An Investigation into the Accretion Processes of Young Stellar Objects

A dissertation submitted to the University of Dublin
for the degree of Doctor of Philosophy

Camille Elizabeth Stock, B.S., M.Sc.
School of Physics

Supervisor:
Prof. Tom P. Ray

March 2023

Trinity College Dublin
Coláiste na Tríonóide, Baile Átha Cliath
The University of Dublin

DIAS
Institiúid Ard-Léinn Bhaile Átha Cliath | Dublin Institute for Advanced Studies

Declaration

I have read and I understand the plagiarism provisions in the General Regulations of the University Calendar for the current year, found at: https://www.tcd.ie/calendar

I have also completed the Online Tutorial on avoiding plagiarism 'Ready, Steady, Write', located at
http://tcd-ie.libguides.com/plagiarism/ready-steady-write

I declare that this report is my own work, is not copied from any other person's work (published or unpublished), and has not previously submitted for assessment either at Trinity College Dublin or elsewhere.

Name: Camille Elizabeth Stock

Signature: ..... **Date:** .....

Acknowledgements

I would like to acknowledge my supervisor Tom for this amazing opportunity to study here at DIAS and his continued understanding when times have been rough throughout this PhD. His insightful and thorough comments have been been integral to my understanding and learning.

To Alessio and Rebeca, for all your guidance and knowledge, your spectroscopy expertise has been immensely helpful. Also thank you for your continued support even when I was doubting myself.

To Antonella, for all your scientific insights and discussions. Thank you for working tirelessly with me to publish my second paper and giving me the chance to work on my thesis from your lovely home in Dundrum.

To the Fitzwilliam Place PhD students and postdocs who have made me feel at home in Dublin (and at O'Briens with a pint in hand), past and present: Mario, Eoin, Anton, Jess, Sam, Dev, Donna, Shilpi, Robin, Ciara, Aoife, Brendan, Shane M, Alberto, Gerhard (I will never forget all your lunchtime conversations!), Johnny, and Jeroen.

To Maria K and Rubén, both of whom I could not have found my footing without, and helped me throughout my first two years. Thanks for all the support and laughs!

To Maria M for putting up with me as a flatmate (sorry!) when we both first moved to Dublin, and for always being there for me to rant or complain or chat about whatever.

To Simon for your friendship, support, and nights at Blackbird, especially in my first two years at DIAS. I miss you, Marty, and Freddie! (and Jenny and Frankie of course)

To Jack for all the fun nights out (stop buying me pints!) and chats. Here's to many more!

To the Dunsink crew who have made me immediately feel at home these last few months of my PhD and have shown unwavering support when all I can do is rant/cry in the kitchen about my thesis: Dale, Sophie, Caitriona, Johnny (again!), Sadhbh, Stephenie, and James.

To all my Hiking Society peeps from Trinity: Laurie, Jamie, Beck, Isabel, Adam, Aislinn, Una, Kush, Itzi, Caoimhe, Chris, Carlos, Q, Matthias, Robert, and John. There's nothing quite like a group of people that you can trudge through the bog in the freezing cold in the rain and still be laughing your ass off. I am so proud to have been on the (chaotic) committee with all you lovely people and to have made so many lifelong friends. Here's to the next mountain (and bog)!

In my time in Dublin, I have also made some amazing friends outside college who have had a real positive impact on my life: Jade, Natalia, Janneke, Selin, Laura, Seán, Pran, and Helena.

And of course I cannot forget my amazing flatmates who have put up with me for 3 years: Jane (and snakey! I couldn't leave him out) and Paula. I will always look back fondly on my time at 205, I already miss Rathmines and you gals!

There are a few friends not from Dublin who also deserve to be mentioned because without their support, chats, and love, this PhD simply would not have been completed: Mark, Stacy, Mo, Beverly, Jenny, and Monique.

I also would like to thank my family for all the support and love. I cannot wait to visit home again and go on a family road trip!

I would be amiss not to thank the lovely and kind people at the TCD Counselling center for the support through my darkest times. Also, to Ralph for her mentoring and generally wonderful personality at the Peer Support office.

To Pauline, for the unwavering support in me and my work. For tolerating incessant questions and late nights with grace and always making me feel comfortable to seek advice. This could not have happened without you, and

I look forward to our continued friendship. I will always be here to pet-sit Doze and Mia.

And finally, to Pearse. Thank you for loving me and being my rock. You are always there for me when I'm a wreck and just want to scream and cry and rant all at the same time, and amazingly you never fail to make me feel better. I am so lucky to have found you in this crazy thing called a PhD and I look forward to our future together. I love you.

Thank you

Abstract

The way in which young stars form is complex and fascinating, and is anything but a smooth, continuous process. Studying their dramatic, and sometimes violent, early years of accreting and ejecting material is vital in understanding how a star will evolve. Of these young objects, protostars are generally less well-studied than the more evolved pre-main sequence (PMS) stars due the necessity of infrared observations to probe through the dusty envelope surrounding protostars. Variability of these young stellar objects (YSOs) and whether or not they are capable of strong episodic accretion is also left relatively unstudied. Variability appears in the accretion and ejection processes of PMS stars as well. To establish a broader understanding of the evolution of young stars it is necessary to investigate different classes of protostar and PMS stars, as well as different timescales of the variability. This thesis aims to contribute to this understanding of the characterisation and sources of different kinds of accretion and ejection variability, by focusing on two young stars: IRS 54 and RU Lup.

Firstly, the very low-mass star (VLMS) IRS 54, of mass $M_\star \sim 0.1 - 0.2\,M_\odot$, which is still in its early stages of its evolution, was investigated. As episodic accretion is likely how young stars accrete most of their mass, it is important to understand on what kinds of timescales these events are occurring and how stellar properties influence them. Through multi-epoch, near-infrared (NIR) spectroscopic and photometric data obtained with the instruments Very Large Telescope/ISAAC and VLT/SINFONI, multiple accretion- (Paβ and Brγ) and outflow-tracing (H_2 2.122 μm and [Fe II] 1.644 μm) emission lines present were investigated to examine physical properties and kinematics of the object. Taking advantage of VLT/SINFONI's integral field unit (IFU) capabilities, it was also possible to detect the red- and blue-shifted lobes of the protostellar jet launching material away from the object. The morphology of the jet and outflow cavities is discussed, providing more context about the system as a whole. The mass accretion rate ($\dot{M}_{\rm acc}$) was calculated and compared across four epochs, roughly a few years apart. It was found to increase from $\sim 1.7 \times 10^{-8}\,M_\odot\,{\rm yr}^{-1}$ in 2005 to $\sim 2.6 \times 10^{-7}\,M_\odot\,{\rm yr}^{-1}$ in 2013, suggesting an accretion burst. This study explores the trends in visual extinction (A_V), mass accretion rate and flux over these epochs and how they fit into the complex processes at work in the inner regions of IRS 54. Increases in all three of these quantities

was found and is attributed to a potential EXor-type outburst, making IRS 54 one of the lowest mass YSOs to show this behaviour.

Delving further into the kinds of variability found in these young stars, a slightly more evolved star (a PMS star) over the much shorter timescale of 15 days was investigated. The chosen target, RU Lup, has a mass of $M_\star \simeq 0.65\,M_\odot$ and is a very strong accretor, which produces many strong emission lines in the optical spectrum. As RU Lup is a PMS star, its dusty envelope has almost completely dissipated, allowing it to be observed optically. This study analysed spectroscopic data from the instrument Canada-France-Hawaii-Telescope/ESPaDOnS and imaging data from the instrument Cerro Tololo Inter-American Observatory/ANDICAM to characterise the short-timescale variability of RU Lup over roughly 15 nights of observations. The accretion luminosity, mass accretion rate and veiling were calculated and their sources of variability were investigated. The photospheric lines of Na I 5688 Å, Mn I 6021 Å and Li I 6707 Å were utilised to estimate the veiling present in RU Lup's spectrum. Additionally, wind-tracing emission lines ([O I] 6300 Å and [S II] 6730 Å) were observed to be very stable over the short time interval of these observations, indicating no dependence on the accretion variability detected. By comparing the variability in measurements of accretion luminosity found via accretion-tracing line profiles with the variability in measurements of veiling, a positive correlation between the two was found, which is independent of extinction.

The types of variability explored in this thesis paint a dynamic picture of the process young stars undergo when evolving. These studies demonstrate the value of both optical and infrared observations in studying different ages of YSO. Observations at different wavelength ranges complement each other, highlighting different aspects of the star formation process, which demonstrates the advantage of simultaneous multi-wavelength observations when characterising the accretion and ejection of an object.

List of Publications and Presentations

Publications

Stock, C.; McGinnis, P.; A. Caratti o Garatti; Natta, A.; Ray, T. P. (2022), Astronomy & Astrophysics, 668, A94. *Accretion variability in RU Lup.*

https://doi.org/10.1051/0004-6361/202244315

Stock, C.; Caratti O Garatti, A.; McGinnis, P.; García López, R.; Antoniucci, S.; Fedriani, R.; & Ray, T. P. (2020), Astronomy & Astrophysics, 643, 181. *Investigating episodic accretion in a very low mass young stellar object.*

https://doi.org/10.1051/0004-6361/202038897

Lubin, D., Holden, B. P., **Stock, C.**, Melis, C., & Tytler, D, (2022), The Astrophysical Journal Supplements. *Lithium abundance and activity in solar analog field stars.* (in prep)

Conferences & Workshops

Irish National Astronomy Meeting (INAM), Dublin, Ireland. September 2022 *(Contributed talk, LOC, session chair)*

Cool Stars 21, Toulouse, France. July 2022 *(Contributed talk)*

Star Formation: from Clouds to Discs, Malahide, Ireland. October 2021 *Poster presentation, LOC, session chair*

Irish National Astronomy Meeting (INAM), virtual. September 2021 *SOC, session chair*

Cool Stars 20.5, virtual. March 2021 *Poster presentation*

Irish National Astronomy Meeting (INAM), virtual. September 2020 *Contributed talk*

Take a Closer Look Conference, Garching, Germany. October 2018 *(Poster presentation)*

Interferometric Data Processing Workshop for eMerlin & ALMA, Dublin, Ireland. September 2018 *(Attended)*

Very Large Telescope Interferometer (VLTI) Summer School, Lisbon, Portugal. July 2018 *(Attended)*

List of acronyms

2MASS - Two Micron All-Sky Survey

AT - Auxillary Telescope

AAT - Anglo-Australian Telescope

AGN - Active Galactic Nuclei

ANDICAM - A Novel Dual Imaging Camera

AO - Adaptive Optics

BC - Broad Component

BLVC - Broad Low Velocity Component

CASA - Common Astronomy Software Applications

CCD - Charge-Coupled Device

CFHT - Canada-France-Hawaii Telescope

CNO - Carbon-Nitrogen-Oxygen (cycle)

CTIO - Cerro Tololo Inter-American Observatory

CTTS - Classical T Tauri Star

ESO - European Southern Observatory

ESPaDOnS - SpectroPolarimetric Device for the Observation of Stars

EW - Equivalent Width

EXor - EX Lupi-type

FIR - Far-Infrared

FUor - FU Orionis-type

FWHM - Full Width at Half Maximum

HH - Herbig-Haro

HVC - High Velocity Component

IFU - Integral Field Unit

IR - Infrared

IRAF - Image reduction and analysis facility

IRAP - L'Institut de Recherche en Astrophysique et planétologie

ISAAC - Infrared Spectrometer and Array Camera

JWST - James Webb Space Telescope

KMOS - K-band Multi Object Spectrograph

KH - Kelvin-Helmholtz (instability)

KPNO - Kitt Peak National Observatory

LSR - Local Standard of Rest

LTE - Local Thermodynamic Equilibrium

LVC - Low Velocity Component

mas - milliarcsecond

MHD - Magnetohydrodynamic

MIR - Mid-Infrared

NASA - National Aeronautics and Space Administration

NB - Narrow Band

NC - Narrow Component

NLVC - Narrow Low Velocity Component

NEOWISE - Near-Earth Object Wide-field Infrared Survey Explorer

NIR - Near-Infrared

NOAO - National Optical Astronomy Observatory

PMS - Pre-main Sequence

PSF - Point Spread Function

RT - Rayleigh-Taylor (instability)

SED - Spectral Energy Distribution

SINFONI - Spectrograph for Integral Field Observations

SMARTS - Small and Medium Aperture Research Telescope Facility

SNR - Signal-to-Noise Ratio

SPIRou - Spectropolarimétre Infrarouge

SpT - Spectral Type

TTS - T Tauri Star

UT - Unit Telescope

UV - Ultraviolet

VLMS - Very Low-Mass Star

VLT - Very Large Telescope

WISE - Wide-Field Infrared Survey Explorer

WTTS - Weak line T-Tauri Star

YSO - Young Stellar Object

ZAMS - Zero Age Main Sequence

Contents

1

Introduction

1.1 Low-mass star formation

The formation of a low-mass star ($M_\star \lesssim 2\,M_\odot$) is relatively well understood and the different evolutionary stages it undergoes during formation can be separated into four classes: 0, I, II and III (see reviews of Shu et al., 1987; Luhman, 2012). The formation of high-mass stars is less certain, although recent studies indicate they may evolve in a similar manner (Fedriani et al., 2019). Nebulae and molecular clouds are ideal nurseries for young stars, which tend to form in groups, not in isolation. A few notable star forming regions are the Orion Nebula, Lupus (e.g. Fig. 1.1), Taurus, and the Rho Ophiuchi clouds (Blitz, 1993; de Zeeuw et al., 1999; Lada & Lada, 2003; Rigliaco et al., 2012; Alcalá et al., 2014; Manara et al., 2015).

Figure 1.1: A wide-field image of the Lupus 3 star forming region taken with the VLT Survey Telescope and the MPG/ESO 2.2-metre telescope. Blue represents emission at 4670Å and red at 6600Å *Credit: ESO; R. Colombari.*

1.1.1 The collapse of molecular clouds

Stars begin their life in molecular clouds: structures spanning sizes between 10pc and 100pc and with masses from $10^4 - 10^6\,M_\odot$ (Hartmann, 2009). The distribution of gas in these clouds is of a filamentary form, with dense ($\gtrsim 10^3\,\mathrm{cm}^{-2}$), cold molecular cloud clumps. Naively assuming magnetic fields do not play a role, these clouds collapse under free-fall conditions, where there are no forces acting against the gravitational pull, which can be defined temporally by the free-fall timescale:

$$t_{ff} = \sqrt{\frac{3\,\pi}{32\,G\,\bar{\rho}}}\,, \tag{1.1}$$

where t_{ff} is the mean time for the cloud to collapse completely, G is the gravitational constant (6.6743×10^{-11} $\mathrm{m}^3\,\mathrm{kg}^{-1}\,\mathrm{s}^{-2}$) and $\bar{\rho}$ is the initial mean density of the cloud. This collapse continues until the thermal pressure of the gas grows and begins to counteract the gravitational pressure (Schulz, 2005). Specifically, the conditions where the gas pressure pushing outward matches the gravitational forces pulling the material inward are described by the Jeans instability (Jeans, 1902). In 1902 James Jeans defined the shortest length-scale where these pressures are balanced. This is now called the Jeans length, and lengths longer than this will result in gravitational collapse:

$$\begin{aligned}\lambda_J &= c_s \sqrt{\frac{\pi}{G\,\rho(r)}} \\ &= 0.19 \left(\frac{T}{[10\,\mathrm{K}]}\right)^{1/2} \left(\frac{n_{\mathrm{H_2}}}{[10^4\,\mathrm{cm}^{-3}]}\right)^{-1/2} \mathrm{pc}\,,\end{aligned} \tag{1.2}$$

where λ_J is the Jeans length, c_s is the speed of sound, $\rho(r)$ is the density of a cloud with radius r and $n_{\mathrm{H_2}}$ is the number density of the gas (in this case, assumed only to be H_2). An associated critical mass (the Jeans mass) can be calculated from the Jeans length, assuming the cloud core is spherically symmetric and isothermal:

$$\begin{aligned}M_J &= \frac{4\,\pi}{3}\,\rho(r) \left(\frac{\lambda_J}{2}\right)^3 \\ &= 1.0 \left(\frac{T}{[10\,\mathrm{K}]}\right)^{3/2} \left(\frac{n_{\mathrm{H_2}}}{[10^4\,\mathrm{cm}^{-3}]}\right)^{-1/2} M_\odot\,,\end{aligned} \tag{1.3}$$

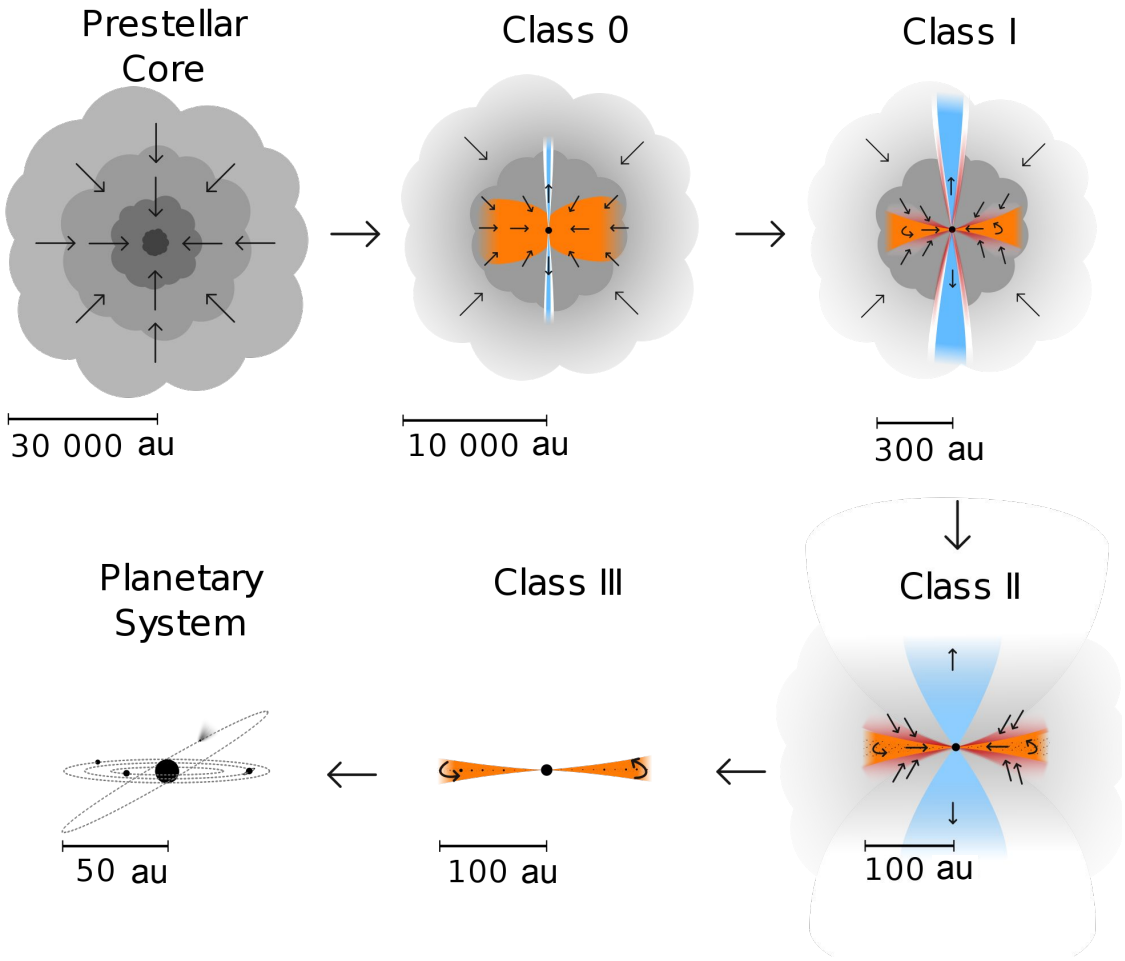

Figure 1.2: An illustration of the stages of low-mass star formation (Persson, 2014a). Orange denotes the accretion disk and accreting material and blue denotes the outflowing material and the jet. Note that Classes 0 and I are considered protostars and Classes II and III are considered pre-main sequence stars.

where M_J is the Jeans mass.

Masses significantly below this threshold are likely to be stable and resist collapse, given an appropriate external pressure. Conversely, masses significantly above this threshold will succumb to gravitational collapse. For instance, molecular clouds themselves contain many coherent clumps that are self-gravitating, with typical values of $T = 10\,\mathrm{K}$ and $n_\mathrm{H} = 10^3\,\mathrm{cm}^{-3}$ (Shu et al., 1987, and references therein). When plugged into Eq. 1.3, the mass needed for stability would be $M_J = 3\,M_\odot$, however, this is more than an order of magnitude below the actual masses of these clumps (Schulz, 2005; Stahler & Palla, 2004), thus they are always close to the onset of gravitational instability and collapse. However, there must be another force acting to mitigate collapse

otherwise there would be a more rapid collapse of these cores, resulting in star formation rates much higher than observed (Zuckerman & Palmer, 1974). The candidate for this is the interstellar magnetic field, although further discussion of the interstellar magnetic field and its effects is beyond the scope of this thesis.

As the core collapses, any existing initial rotation will be amplified by the conservation of angular momentum and will result in most of the material present in the core falling onto a flattened surface, rather than the central object. This process forms a circumstellar disk; material accretes onto the star via this disk (Shu et al., 1987). These accretion disks were first hypothesised as a way to fuel quasars by Lynden-Bell (1969), and a standard model of accretion disks was proposed by Shakura & Sunyaev (1973). An envelope of gas and dust surrounds this disk and the central star, absorbing radiation emitted from within, making it impossible to observe at optical wavelengths. Material in the disk travels inward onto the inner disk toward the truncation radius (Fig. 1.3). This truncation radius is defined as the point where the dynamic stress of the incoming material through the disk balances the magnetic stress from the magnetosphere of the star (see Section 1.2.1 for more details). From here, accretion columns will form along magnetic field lines, onto the stellar surface, providing a path for the accreting material to be channeled along (Ostriker & Shu, 1995). A highly collimated, bipolar jet and winds will also form, ejecting material from the system. This system of structures is considered a protostar (Fig. 1.2), which can be further divided into Class 0 and Class I objects.

1.1.2 Class 0

Class 0 protostars are so deeply embedded in their dusty envelope that they are invisible to optical and near-infrared (NIR) telescopes (Hartmann, 2009). Observations in sub-millimeter and millimeter wavelengths are necessary to investigate these young Class 0 sources. These early stages of formation are accompanied by relatively high mass accretion rates ($\dot{M}_{\rm acc}$) compared to later stages and very powerful jets. As the inner parts of the young stellar object (YSO) are obscured by the dusty envelope, the resulting spectral energy distribution (SED) observed is a combination of black body spectra from the dust (Fig. 1.4).

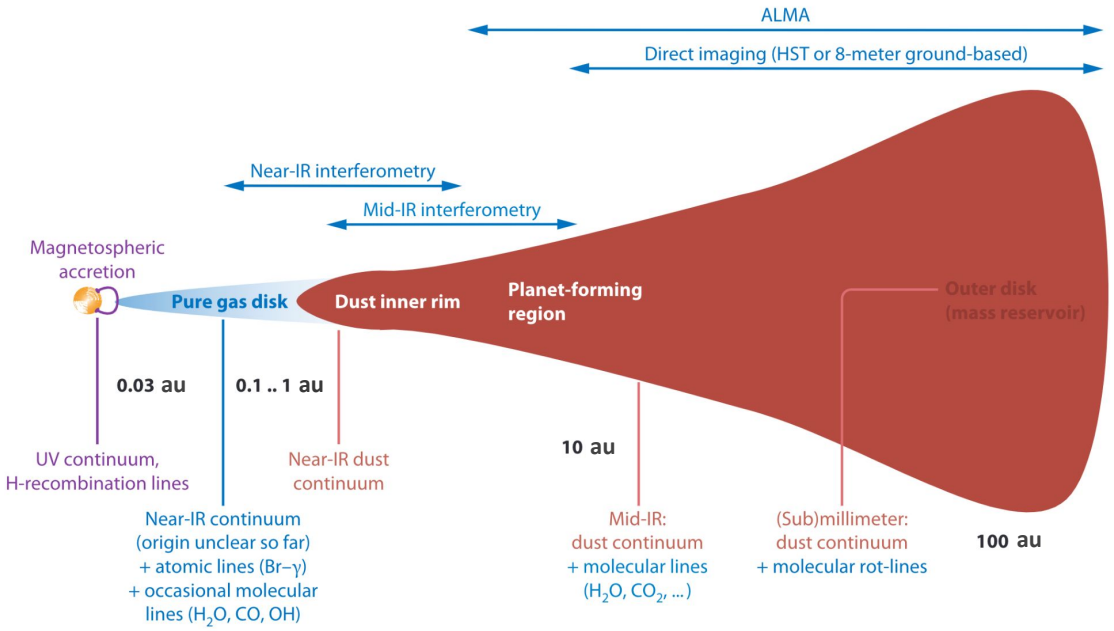

Figure 1.3: A sketch of the spatial scales and structure of the different regions of a protoplanetary disk. The ideal techniques for spatially resolving each region are also above and the different kinds of emission originating from each region are shown below the sketch. The wavelength is shown for increasing radius from the central source (adapted from Dullemond & Monnier, 2010).

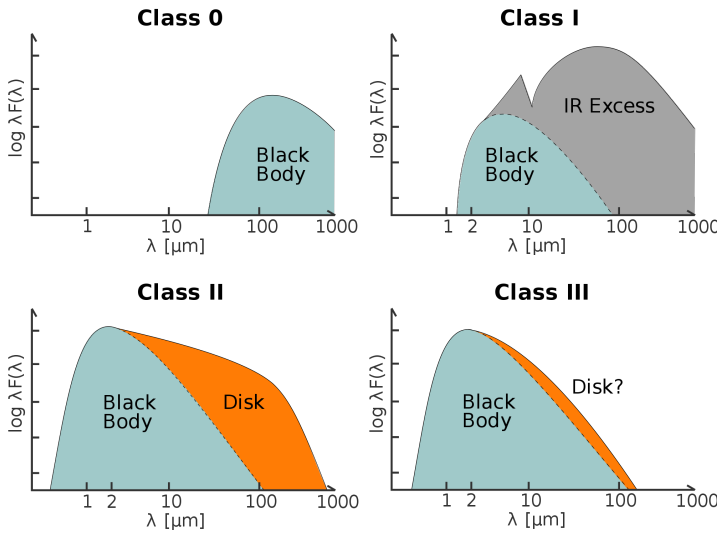

Figure 1.4: The spectral energy distribution (SED) of the different classes of YSO. Note that the 10μm silicate feature can be seen in absorption in the Class I SED. (Persson, 2014b)

1.1.3 Class I

In Class I sources, the gas and dust will continue to fall onto the disk, and from the disk onto the star, depleting the envelope enough that the star becomes detectable in the IR (Hartmann, 2009, See Fig. 1.4). In the past, optical observations were most widely used and these earliest stages of star formation remained a mystery, until IR instruments were designed and provided the opportunity to probe deeper into the encompassing dust. While how the disk and jet relate to one another is not well understood, it is known that there is a strong connection between the two and this is the essence of many studies of protostars (e.g. Hartigan et al., 1995). This process of material falling in to the central star and disk (accretion) is vital to the study of star formation as it helps determine the physical properties of the YSO, including mass, luminosity, and size. Class 0 and I protostars are both characterised by strong accretion rates ($\dot{M}_{\rm acc} \sim 10^{-7} - 10^{-8}\,M_{\odot}\,{\rm yr}^{-1}$) (see White et al., 2007, and references therein), and notably, high mass loss rates ($\dot{M}_{\rm loss} \sim 10^{-8} - 10^{-7}\,M_{\odot}\,{\rm yr}^{-1}$) (see Ray et al., 2007, and references therein).

1.1.4 Class II

Over time more and more material will flow onto the disk and subsequently the star, gradually reducing the envelope. Class II sources are defined by the lack of any substantial envelope surrounding the central star (see Fig. 1.2), and are also classified as T Tauri stars (TTSs). The term T Tauri star refers to a low-mass ($<2\,M_{\odot}$) PMS within the range of $T \sim 7{,}000 - 3{,}000\,{\rm K}$ and spectral type F to M (Joy, 1949; Bertout, 1984).

As they are optically visible, such stars have been known for many years (Joy, 1949; Ambartsumian, 1958). The ones that have many emission lines in their spectra are known as Classical T Tauri Stars (CTTSs) (Hartmann, 2009). The broadening of these emission lines can also be an indicator of accretion, as broadening corresponding to a velocity of $> 270\,{\rm km\,s}^{-1}$ is believed to be due to material accelerated toward the star (White & Basri, 2003).

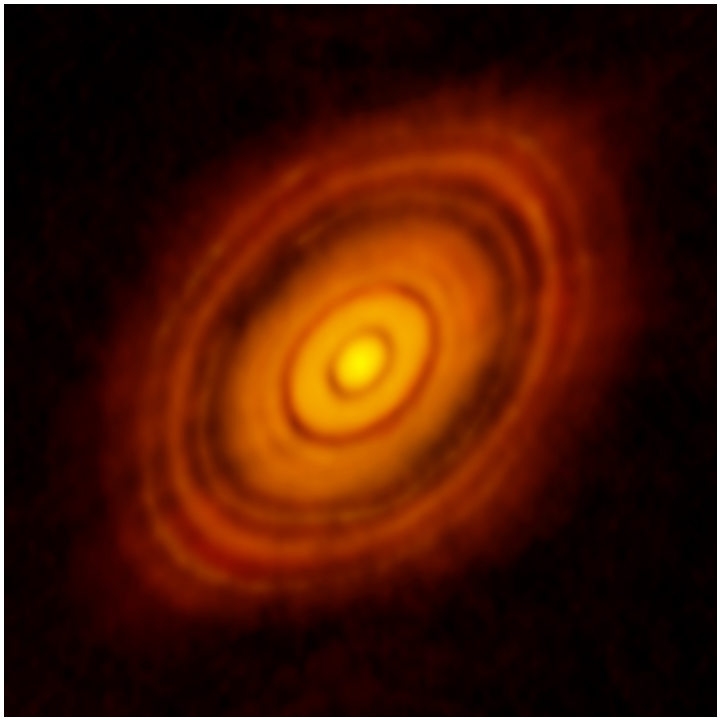

Figure 1.5: An image of HL Tau's protoplanetary disk which contains gaps possibly carved out by planetary cores. *Credit: ALMA(ESO/NAOJ/NRAO); C. Brogan, B. Saxton (NRAO/AUI/NSF).*

1.1.5 Class III

CTTSs' counterparts, weak-line T Tauri stars (WTTSs), are not undergoing accretion and thus have a weaker emission spectrum (e.g. Hα emission). The strength of this Hα emission can be measured through its equivalent width, which is often used as a proxy for accretion. For a star to be considered a WTTS, its equivalent width is usually $\mathrm{EW}_{\mathrm{H}\alpha} < 10\,\text{Å}$ (Appenzeller & Mundt, 1989). However, there are exceptional objects such as FUors (see Section 1.4.1), that are dominated by winds or infall of material that exhibit a small $\mathrm{EW}_{\mathrm{H}\alpha}$ despite still accreting. These WTTSs have historically been considered Class III due to the dissipation of their disk (Duvert et al., 2000). However, this strict dichotomy has been called into question in Gras-Velázquez & Ray (2005) where the authors detected an infrared excess emission in a sample of WTTSs, potentially indicating the existence of accretion disks. This illustrates a more gradual transition from CTTSs to WTTSs than merely a threshold set by the $\mathrm{EW}_{\mathrm{H}\alpha}$.

Young stars' disks have the potential to form planets. This is possible through clustering of material within the disk aggregating into clumps that will eventually become

planets and can carve out gaps in the disk (as seen in Fig. 1.5), along with other mechanisms (Dunham et al., 2014). These gaps can also form in Classes I/II objects, as was observed with the Atacama Large Millimeter/Submillimeter Array (ALMA) (e.g. ALMA Partnership et al., 2015; Andrews et al., 2016). The fourth stage of the evolution of a young star, Class III, is characterised by the eventual ceasing of accretion activity and the dissipation of the jet outflow activity, and in the case of low-mass stars, is identified with the WTTS phase (Hartmann, 2009, see Fig. 1.2).

1.1.6 ZAMS

Continuing to succumb to gravitational contraction, a young star eventually leaves its PMS phase. Its next stage will be the main sequence, defined by the ignition of hydrogen burning. This line in the Hertzsprung–Russell diagram is known as the zero-age main sequence (ZAMS). In contrast to their low-mass counterparts, high-mass stars ($> 8\,M_{\odot}$) reach the ZAMS while they are still accreting the majority of their mass (Beuther et al., 2007; Motte et al., 2018), thus their evolutionary tracks are very different. The burning of hydrogen begins when the interior of the star surpasses 1.0×10^{7} K and pairs of protons can combine to form deuterium, a positron and a neutrino:

$$^{1}\mathrm{H} + {}^{1}\mathrm{H} \rightarrow {}^{2}\mathrm{H} + \mathrm{e}^{+} + \nu \ . \tag{1.4}$$

This "PP chain" (proton-proton chain) continues, and subsequent reactions include:

$$\begin{aligned} {}^{2}\mathrm{H} + {}^{1}\mathrm{H} &\rightarrow {}^{3}\mathrm{He} + \gamma \\ {}^{3}\mathrm{He} + {}^{3}\mathrm{He} &\rightarrow {}^{4}\mathrm{He} + {}^{1}\mathrm{H} + {}^{1}\mathrm{H} \ . \end{aligned} \tag{1.5}$$

The second reaction in Eq. 1.5 is one of multiple paths in which ^{4}He is generated. The production of ^{4}He from four H nuclei is vital for the evolution of the young star as this reaction releases 26.7 MeV of energy: sufficient to halt contraction. This process continues until the rising temperature within the star grows hot enough that another fusion reaction takes over to create ^{4}He nuclei, namely, the Carbon-Nitrogen-Oxygen (CNO) cycle. The CNO cycle dominates the fusion process in early-type main sequence stars at temperatures of $\sim 1.7 \times 10^{7}$ K (Stahler & Palla, 2004; Schulz, 2005). This process accomplishes the production of ^{4}He via heavier atoms in a sequence of reactions

that emits an α particle (a stable ^{4}He nucleus), among other particles, and outputs the same important 26.7 MeV of energy. The net reaction of the CNO cycle is:

$$4\,^1\mathrm{H} \rightarrow {}^4\mathrm{He} + 2\,\mathrm{e}^+ + 2\,\nu\ . \tag{1.6}$$

For example, it would take a $1M_\odot$ star roughly 16 Myrs to reach this state.

1.1.7 SEDs of YSOs

A more rigid and quantitative definition of protostellar classes is contingent on the shape of the SED of the YSO (Dunham et al., 2014) in the infrared, specifically its spectral index (α). An SED illustrates how the flux ($\lambda\,F_\lambda$) changes with wavelength (λ) and the spectral index represents the slope of the SED between $\sim 2.2 - 10\,\mu$m (Greene et al., 1994). How the IR excess varies between classes is shown in Fig. 1.4. Class 0 and Class I objects are still embedded and their envelope radiates in the IR. As described above, Class 0 are completely obscured by this envelope, therefore the only emission present is the black body of the envelope (blue component in the top left panel of Fig. 1.4). Class I protostars are still deeply embedded, however, the black body of the star is visible at NIR wavelengths (blue component in the top right panel of Fig. 1.4). The grey component of this Class I part of the figure represents both the envelope that is absorbing the shorter wavelengths emitting from the star and re-emitting them at longer, mid-infrared (MIR) and far-infrared (FIR) wavelengths, and the disk. Once Class II is reached and the envelope has dissipated, any IR excess emission observed is due to the optically thick disk and extends into the MIR and FIR (orange SED component in the bottom left panel of Fig. 1.4). By the Class III phase, the star may have a slight IR excess due to remnants of the disk (orange component in the bottom right panel of Fig. 1.4), however, the SED in this infrared region is dominated by the black body of the stellar surface. The young stars in classes II and III are considered pre-main sequence (PMS) stars. There also exists a phase of a protoplanetary disk's evolution between Class II and Class III characterised by a 'transition disk'. This is defined to be a disk structure with a large gap between the outer disk and the star, and a disk containing multiple gaps (between the star and inner disk, and then between the inner disk and the outer disk) is considered a 'pre-transitional disk' (Espaillat et al., 2014). These different

kinds of disks can be identified from ALMA images in the submillimetre (see e.g. ALMA Partnership et al., 2015) or from the slope of their SEDs where the typical IR excess of young stars is in deficit (see Fig. 1.6).

1.2 Accretion

1.2.1 Magnetospheric accretion

Young low-mass stars are characterised by their accretion activity and how material is transported from the disk to the surface of the star, which has been an ongoing topic of study for decades. Originally, it was thought that this occurred in a boundary layer between the slowly rotating star and a more rapidly rotating disk, producing high temperature emission (Lynden-Bell & Pringle, 1974). However, a more likely explanation explored in the subsequent years was that material from the inner disk is disrupted by the central star's magnetic field, funneling it along the magnetic field lines and then crashing onto the stellar surface and producing shocks (Camenzind, 1990; Königl, 1991; Calvet & Hartmann, 1992; Hartmann et al., 1994; Ostriker & Shu, 1995). This paradigm is most directly confirmed by the observed asymmetry in emission lines in T Tauri stars. This red-shifted absorption seen is believed to originate in the magnetospheric accretion columns as the material flows toward the stellar surface (Calvet & Hartmann, 1992; Hartmann et al., 1994; Edwards et al., 1994; Muzerolle et al., 1998, 2001). Fig. 1.7 illustrates the complexity of structure present in the inner disk region of these objects. This region contains multiple radii of note such as the magnetospheric truncation radius ($R_{\rm mag}$), co-rotation radius ($R_{\rm co}$) and dust sublimation radius ($R_{\rm sub}$). For reference, these different radii and their associated uncertainties can be seen in Fig. 1.8, where the relative distances between these radii are shown to vary between the sampled T Tauri stars.

The co-rotation radius is defined where the Keplerian angular velocity of the disk equals the stellar angular velocity (Bouvier et al., 2007):

$$R_{\rm co} = (G\,M_\star)^{2/3} \left(\frac{P_{\rm rot}}{2\pi}\right)^{2/3}, \tag{1.7}$$

where G is the gravitational constant and $P_{\rm rot}$ is the rotation period of the star.

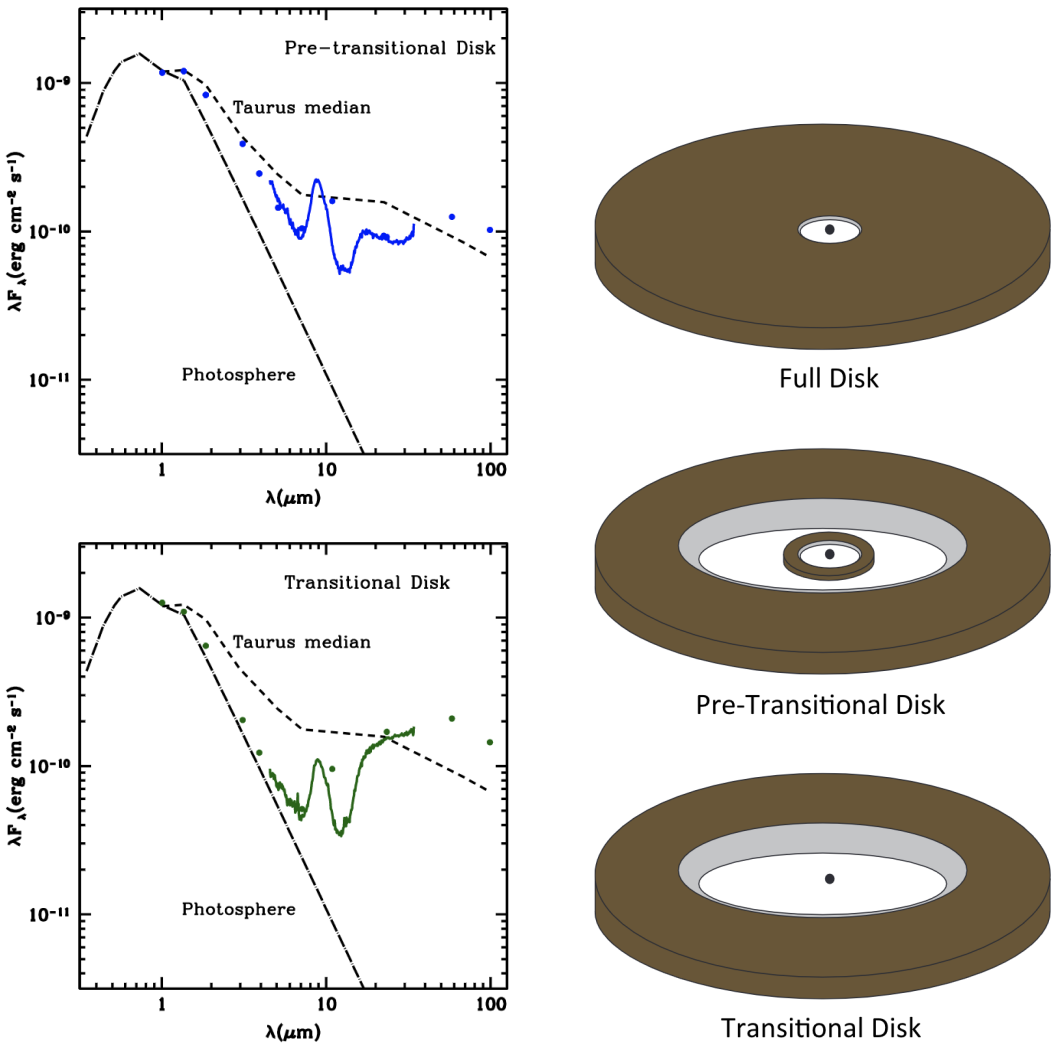

Figure 1.6: *Left:* Two SEDs exhibiting a pre-transitional disk (LkCa 15 Espaillat et al., 2007) and a transitional disk (GM Aur Calvet et al., 2005). These are scaled to the stellar photosphere (dot-dashed-long line) and are also compared with the Taurus median SED (short-dashed line) (D'Alessio et al., 1999). *Right:* A diagram showing the differences in structure of a full disk, pre-transitional disk and transitional disk. (Espaillat et al., 2014)

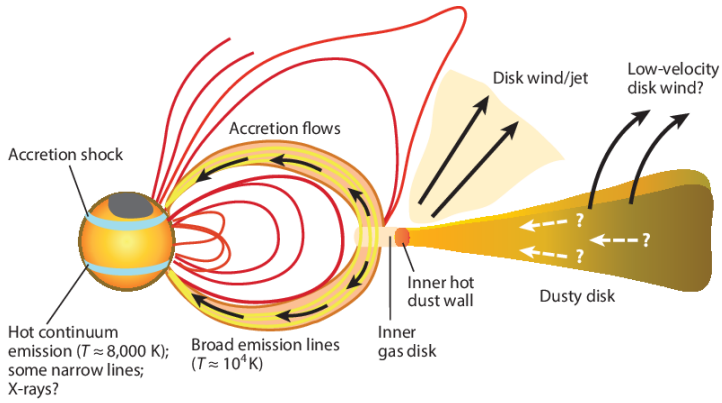

Figure 1.7: A diagram showing the process of magnetospheric accretion in a young star (Hartmann et al., 2016).

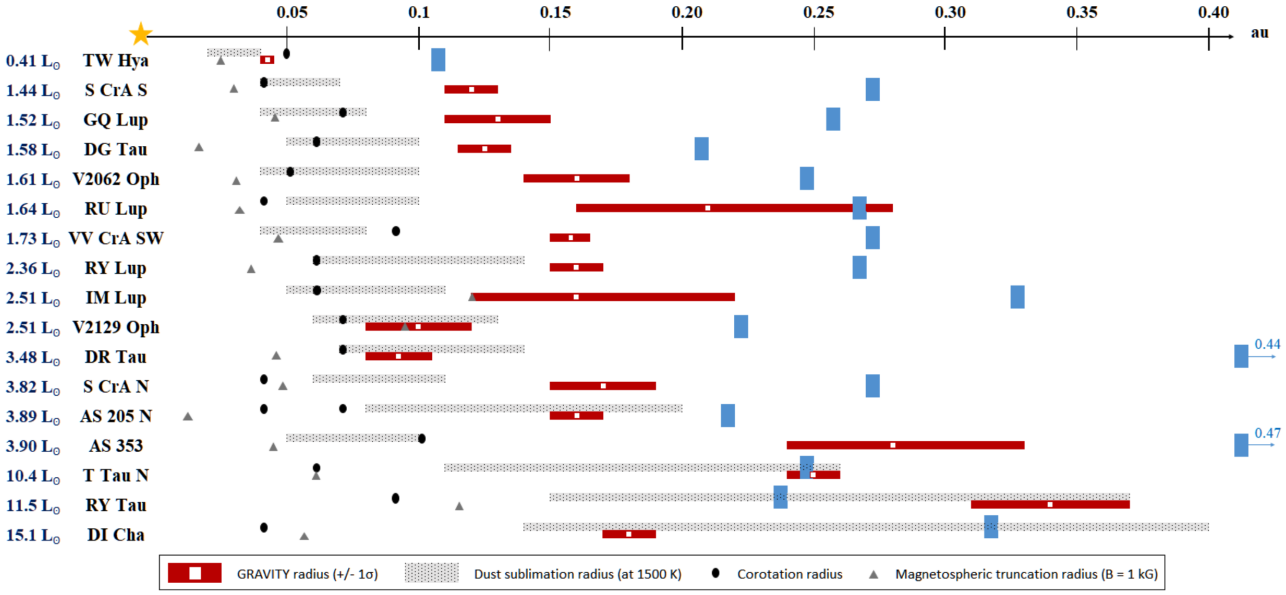

Figure 1.8: Key size properties of T Tauri star targets in the Perraut et al. (2021) sample. The authors employed a ring model approach using the interferometer GRAVITY to measure co-rotation radii $R_{\rm co}$ (black circles), magnetic truncation radii $R_{\rm mag}$ for a magnetic field of 1 kG (gray triangles), range of sublimation radii $R_{\rm sub}$ (gray lines), half-flux radii a derived from the GRAVITY measurements (white squares) including 1σ error bars (red lines) and the achieved angular resolution is shown for comparison (blue rectangles) (Perraut et al., 2021).

The material that eventually gets accreted onto the star is transported inward to ~ 0.1 au through the outer and inner disk. The outer disk is much further out than the inner disk, extending out from tens to $\sim 1{,}000$ au from the central object whereas the inner disk exists at about a few stellar radii (< 0.1 au). The timescales of the processes at work in the outer disk are therefore a million times longer than in the inner regions and have $T \sim 10 - 30$ K in contrast to the relatively high temperatures of $T \sim 1{,}000$ K of the inner disk (Dullemond & Monnier, 2010). This inner dusty disk borders the inner gaseous disk where temperatures are high enough to destroy the dust, marking the dust sublimation radius (in terms of au):

$$R_{\rm sub} = 1.1\sqrt{Q_R}\sqrt{\frac{L_\star}{1000\,L_\odot}}\left(\frac{1500}{T_{\rm sub}}\right)^2, \tag{1.8}$$

where Q_R is the ratio of the dust absorption efficiencies of the incident field and the re-emitted field, $L_\star$ is the luminosity of the star, $L_\odot$ is the solar luminosity and $T_{\rm sub}$ is the dust sublimation temperature (Monnier & Millan-Gabet, 2002). Q_R is dependent on the properties of the dust, such as grain size and the effective temperature ($T_{\rm eff}$) of the star.

Due to the increased heat from the central star, the inner wall of this boundary re-radiates this energy at longer wavelengths, namely the NIR. This observed NIR excess produced is a hallmark of these young, strongly-accreting stars and is why they appear invisible at optical wavelengths when undergoing very strong accretion (e.g. Class I YSOs).

The inner gaseous disk is truncated when the stellar magnetic field is dominant. This occurs when the ram pressure of the gas is equivalent to that of the magnetic field:

$$\frac{B^2}{8\pi} = \rho\, v^2, \tag{1.9}$$

where B is the equipartition magnetic field strength where the pressure of the magnetic field balances the gas ram pressure ($p_{\rm ram} = \rho\, v^2$), ρ is the density of the gas and v is the Keplerian velocity at the radius in question.

This location where the magnetic field meets the inner disk $R_{\rm mag}$ can be approxi-

mated in terms of $R_{\odot}$, when assuming a dipole moment (μ), as

$$R_{\rm mag} \approx \xi \left(\frac{\mu^4}{4\,G M_{\star} \dot{M}_{\rm acc}^2} \right)^{1/7}, \tag{1.10}$$

where ξ is a correction factor dependent upon the details of the disk-magnetosphere interaction ($\xi \lesssim 1$), $M_{\star}$ is the mass of the star and $\dot{M}_{\rm acc}$ is the mass accretion rate (Hartmann et al., 2016). Assuming values for a typical young star as $M_{\star} = 0.5\,M_{\odot}$, $R_{\star} = 2\,R_{\odot}$, a magnetic field of $B \approx 1 - 2\,{\rm kG}$, $\xi \approx 0.7$, and $\dot{M} \approx 10^{-8}\,M_{\odot}\,{\rm yr}^{-1}$, the result is $R_{\rm mag} \approx 4 - 6\,R_{\star}$. This radius is used throughout the literature as "$R_{\rm in}$", or the truncation radius utilised to calculate accretion rates. Due to the complexity of defining the inner gaseous disk region, the prevailing assumption $R_{\rm in} \sim 5R_{\star}$ is used in part to maintain continuity between studies (e.g. Gullbring et al., 1998; Hartmann et al., 1998; Herczeg & Hillenbrand, 2008; Dullemond & Monnier, 2010; Rigliaco et al., 2012; Manara et al., 2016; Alcalá et al., 2017) and because the value can range between $3 - 8\,R_{\star}$ for pre-main sequence stars. The error introduced by this assumption on the subsequent mass accretion rates is estimated by Rigliaco et al. (2012) to be $< 20\%$. This assumed value also takes the co-rotation radius into account, constraining $R_{\rm in}$ to be less than the co-rotation radius, which is typically $5 - 6\,R_{\star}$ (Gullbring et al., 1998). This is because stellar field lines that couple to the gaseous disk further out than $R_{\rm co}$ will work to slow down the rotation of the star. Conversely, stellar field lines coupled to the disk inside $R_{\rm co}$ will cause the star to spin up. The magnetic field is able to couple to the gas in this inner region due to the high (enough) temperatures of $T \geq 1{,}000\,{\rm K}$ that allow collisional ionisation of the metal atoms to occur (Königl, 1991). Following on from this, the accretion process necessitates that infalling material be within $R_{\rm co}$, otherwise material outside this radius will experience a centrifugal force, flinging the material away from the star (Bouvier et al., 2007). Thus, for accretion to happen, $R_{\rm in} < R_{\rm co}$ for the net force to aid the material in accreting onto the star. Throughout this thesis, the region where the inner gaseous disk is truncated by the magnetic field will be defined as $R_{\rm in} = 5R_{\star}$.

Where the magnetic field intercepts the inner disk, the disk is truncated and the gas forms magnetospheric accretion columns (or "funnels") following the magnetic field lines, arching toward the magnetic poles of the star (in the simple dipolar case) (Bouvier

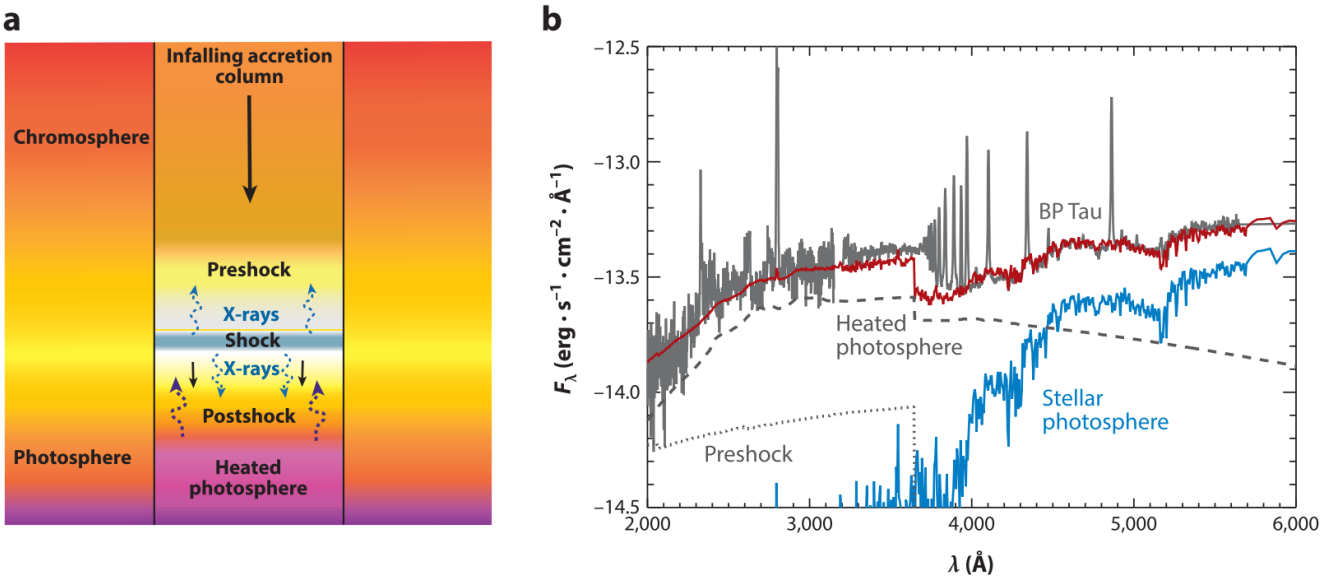

Figure 1.9: **(a)** A diagram of the preshock, shock and postshock regions on the stellar surface, due to infalling material along an accretion column Hartmann et al. (2016). **(b)** A spectrum from the Classical T Tauri star BP Tau (grey), a spectrum of the stellar photosphere (blue), a spectrum of the preshock region (dotted grey), a spectrum of the heated photosphere (dashed grey) and the combination of these shock models (red). The models are from Ingleby et al. (2013).

et al., 2007). The temperatures in these columns are more than 8,000 K. As the columns are accreting onto the star, the gas reaches free-fall velocities of roughly $\sim 300\,\mathrm{km\,s^{-1}}$ when it collides with the stellar surface and produces shocks (see Fig. 1.9a). This free-fall velocity can be calculated for a given star as:

$$v_{\rm ff} = \left(\frac{2\,GM_\star}{R_\star}\right)^{1/2} \left(1 - \frac{R_\star}{R_{\rm mag}}\right)^{1/2} . \tag{1.11}$$

The luminosity of these intense shocks generated from the material pummeling the stellar surface can be calculated by assuming all the kinetic energy is dissipated upon impact:

$$L_{\rm s} = \frac{1}{2}\,\dot{M}_{\rm acc}\,v_{\rm ff}^2 , \tag{1.12}$$

where $L_{\rm s}$ is the shock luminosity.

Briefly, as the shock is produced, the temperature of the gas rises to $T \sim 10^6\,\mathrm{K}$, generating soft X-ray emission (photon energies of $0.1 - 1.0\,\mathrm{keV}$). Most of these X-rays are then absorbed by the gas in the pre- and post-shock regions and re-emitted

at longer wavelengths, giving rise to ultraviolet (UV) and optical continua excesses, as well as some broad ($\approx 250\,\mathrm{km\,s^{-1}}$) line emission (Calvet & Gullbring, 1998). Using X-ray instruments such as the Chandra X-ray Observatory[1] and the X-ray Multi-Mirror Mission-Newton[2] (XMM-Newton), it has been possible to observe the X-ray emission that does not get re-absorbed. This provides further support for the magnetospheric accretion model because the densities and temperature of the gas necessary to emit soft X-rays ($T \sim 10^6\,\mathrm{K}$ and $n_e \sim 10^{11-12}\,\mathrm{cm^{-3}}$) are different than that of the coronal gas ($T \sim 10^7\,\mathrm{K}$ and $n_e \sim 10^{10}\,\mathrm{cm^{-3}}$), and these X-rays are not observed in non-accreting stars (Kastner et al., 2001; Stelzer & Schmitt, 2004; Argiroffi et al., 2007; Günther et al., 2007; Güdel & Nazé, 2009; Schneider et al., 2018).

An observable effect of this excess continuum flux is called "veiling" and will be discussed in Section 1.2.3. This excess flux is particularly apparent at UV wavelengths where the excess flux from the shock can be orders of magnitude stronger than the photospheric flux of the star (Hartigan et al., 1991). This is illustrated in Fig. 1.9b where the grey line is the observed spectrum of the young star BP Tau that is affected by magnetospheric accretion, the blue line is a spectrum of just the stellar photosphere and the red line is the shock model (see Ingleby et al., 2013) that incorporates contributions from the preshock flux and the heated photospheric flux. Fig. 1.9b makes it apparent that the difference between the blue and grey spectra is largest at near-UV wavelengths of $2000 - 4000$Å, replicated in the shock model (red line). Accretion through the disk is studied widely through shock models as well (e.g. Dodin & Lamzin, 2012; Gullbring et al., 1998; Espaillat et al., 2021).

This process of magnetospheric accretion concurs with observations in low-mass ($\lesssim 1\,M_\odot$) pre-main sequence stars, however, for young stars of intermediate ($2-5\,M_\odot$) and high ($> 5\,M_\odot$) mass where the magnetic fields at play are much weaker, different theories are necessary to describe their accretion processes (Hartmann et al., 2016).

[1]The Chandra X-Ray Center (CXC) is operated for NASA by the Smithsonian Astrophysical Observatory.

[2]XMM-Newton is an ESA science mission with instruments and contributions directly funded by ESA Member States and NASA.

1.2.2 Measuring accretion

When studying the dynamic system of a star, the mass accretion rate ($\dot{M}_{\rm acc}$) is a very important quantity for investigating the stellar evolution of the accretion disk and the overall variability of the YSO. This rate can be derived from measuring the release of accretion energy ($L_{\rm acc}$) in the form of the UV/optical continuum and line emission, along with other stellar properties such as radius and mass (Gullbring et al., 1998).

The first studies of accretion, mostly in low mass stars, were based on low-resolution spectroscopic observations of the UV excess and U-band photometry in order to model this excess and derive the accretion luminosity (Valenti et al., 1993; Gullbring et al., 1998; Calvet & Gullbring, 1998; Hartmann et al., 1998). The common origin of both the UV excess and certain strong emission lines is the accretion flow. Therefore, it proved useful to relate the line luminosity with the accretion luminosity (obtained directly from the UV excess) at optical wavelengths. This opened the door for further analysis of accretion in large surveys of young stars in many different star formation regions, such as Orion (e.g. Calvet et al., 2004; Robberto et al., 2004; Fang et al., 2009; Rigliaco et al., 2011; Manara et al., 2012), ρ-Ophiucus (e.g. Natta et al., 2004, 2006; Gatti et al., 2006), Lupus (e.g. Alcalá et al., 2014, 2017), Taurus (e.g. Calvet et al., 2004; Alcalá et al., 2021; Gangi et al., 2022), Cepheus OB2 region (e.g. Sicilia-Aguilar et al., 2005, 2010), and the Chameleon clouds (e.g. Biazzo et al., 2012; Manara et al., 2016). The relation between $L_{\rm acc}$ and $\dot{M}_{\rm acc}$ can be seen in Equation 1.13:

$$L_{\rm acc} = \frac{GM_\star \dot{M}_{\rm acc}}{R_\star}\left(1 - \frac{R_\star}{R_{\rm in}}\right), \tag{1.13}$$

where $R_{\rm in} = 5R_\star$, as explained in the previous section and $L_{\rm acc}$ is the accretion luminosity. Rearranging this equation for $\dot{M}_{\rm acc}$, we obtain:

$$\dot{M}_{\rm acc} = \left(1 - \frac{R_\star}{R_{\rm in}}\right)^{-1} \frac{L_{\rm acc}\, R_\star}{GM_\star}. \tag{1.14}$$

To calculate $L_{\rm acc}$, the flux of one of the bright Hydrogen recombination lines is needed, as a relation between these lines and accretion has been shown to exist (Calvet et al., 2004; Alcalá et al., 2014, 2017) although the physical explanation for this is still under debate. However, the observed line flux is extincted by the dust in the YSO

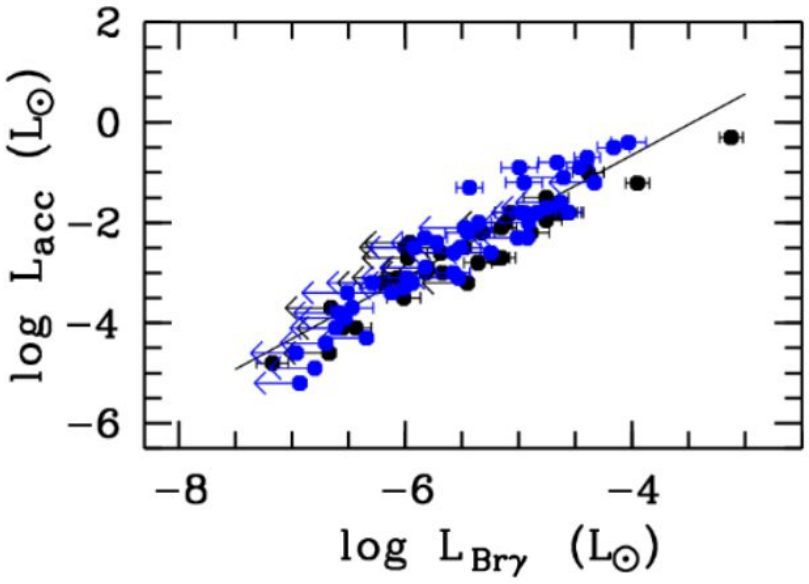

Figure 1.10: A plot showing the linear relationship between $L_{\rm acc}$ and $L_{\rm line}$ (in this case, Brγ) in T Tauri stars (Alcalá et al., 2017).

system and is therefore reddened and must be taken into account. The degree to which this reddening occurs can be calculated from:

$$F_{\lambda}^{0} = F_{\rm obs}^{\lambda} 10^{A_{\lambda}/2.5}, \tag{1.15}$$

where F_{λ}^{0} is the line flux emitted from the source corrected for extinction, $F_{\rm obs}$ is the measured line flux (affected by extinction), and A_{λ} is the extinction measured at a specific wavelength λ. It is especially important to take this reddening into account when studying these early stages of star formation as they are deeply embedded in their parent cloud and the value of A_{λ} is not only non-negligible, but can be quite large. With the extinction-corrected flux and assuming a distance to the object, the line luminosities can be calculated using the following relation to derive $L_{\rm acc}$:

$$L_{\rm line} = 4\pi d^2 F_{\rm line}, \tag{1.16}$$

where $L_{\rm line}$ is the line luminosity, d is the estimated distance from the YSO to the observer and $F_{\rm line}$ is the integrated flux of the line corrected for extinction.

The relation between $L_{\rm acc}$ and $L_{\rm line}$ is empirically derived by Alcalá et al. (2017) by plotting these two parameters for a large sample of YSOs in the star-forming region

Lupus and fitting the data linearly (Fig. 1.10 shows this for the Brγ emission line). This relation holds for line emission that is tracing the accretion process, such as the Hydrogen Balmer, Paschen and Brackett series, Ca II , He I , He II , Na I and O I lines, which were used in the work of Alcalá et al. (2017).

As mentioned above, previous studies have also measured parameters defining this $L_{\rm acc}$ and $L_{\rm line}$ relationship, however, the Alcalá et al. (2017) results are more recent and will be used throughout this thesis. The derived relation can be seen in Equation 1.17:

$$\log\left(\frac{L_{\rm acc}}{L_{\odot}}\right) = a\log\left(\frac{L_{\rm line}}{L_{\odot}}\right) + b, \tag{1.17}$$

where a and b are the parameters derived in Alcalá et al. (2017) and depend on the particular line being measured and $L_{\odot}$ is the solar luminosity. To see the parameters a and b used in this thesis, see Fig. 1.11. Comparing these mass accretion rates from multiple epochs gives insight into the variability of the YSO and helps characterise what phase of evolution the protostar is currently in and how quickly these processes of accretion and ejection change.

1.2.3 Veiling

The presence of an excess emission spectrum in young stars was first noted in Joy (1949), where he studied the spectra of 35 stars in Taurus. This "veiling" effect, notable in CTTSs, has since been studied extensively in many star formation regions. As young pre-main sequence stars, TTSs have accumulated most of their mass and have finished their phases of high accretion activity although the degree of accretion amongst CTTSs is variable in comparison with other low-mass PMS stars, i.e. WTTSs have little-to-no evidence for accretion occuring (e.g. Duvert et al., 2000).

Consequently, the observed spectra of CTTSs exhibit the effects of this accretion activity as increased emission in both the lines and continuum. The observed effect, veiling, is most obvious in photospheric absorption lines, where they appear more shallow or "filled-in" by this excess.

This accretion excess has been modeled in Dodin & Lamzin (2012) wherein their models include both the line emission veiling and continuum veiling (in response to Calvet & Gullbring (1998) who only considered the continuum veiling). Their findings

Diagnostic	λ [nm]	a (±err)	b (±err)
H3 (Hα)	656.2800	1.13 (0.05)	1.74 (0.19)
H4 (Hβ)	486.1325	1.14 (0.04)	2.59 (0.16)
H5 (Hγ)	434.0464	1.11 (0.03)	2.69 (0.17)
H6 (Hδ)	410.1734	1.07 (0.04)	2.64 (0.18)
H7 (Hϵ)	397.0072	1.06 (0.04)	2.69 (0.18)
H8	388.9049	1.06 (0.04)	2.73 (0.18)
H9	383.5384	1.04 (0.04)	2.78 (0.19)
H10	379.7898	1.04 (0.04)	2.83 (0.19)
H11	377.0630	1.06 (0.03)	3.02 (0.18)
H12	375.0151	1.04 (0.03)	3.07 (0.18)
H13	373.4368	1.03 (0.04)	3.13 (0.20)
H14	372.1938	1.03 (0.04)	3.25 (0.21)
H15	371.1977	1.05 (0.04)	3.43 (0.23)
Pa5 (Paβ)	1281.8070	1.06 (0.07)	2.76 (0.34)
Pa6 (Paγ)	1093.8086	1.24 (0.06)	3.58 (0.27)
Pa7 (Paδ)	1004.9368	1.22 (0.09)	3.74 (0.43)
Pa8	954.5969	1.09 (0.12)	3.19 (0.59)
Pa9	922.9014	1.18 (0.08)	3.71 (0.43)
Pa10	901.4909	1.15 (0.10)	3.60 (0.52)
Br7 (Brγ)	2166.1210	1.19 (0.10)	4.02 (0.51)
He I	402.6191	1.05 (0.04)	3.66 (0.22)
He I	447.1480	1.06 (0.04)	3.52 (0.22)
He I	471.3146	0.84 (0.08)	2.89 (0.46)
He IFe I	492.1931	0.97 (0.04)	3.08 (0.24)
He I	501.5678	0.99 (0.04)	3.49 (0.24)
He I	587.5621	1.15 (0.04)	3.67 (0.21)
He I	667.8151	1.25 (0.06)	4.70 (0.33)
He I	706.5190	1.18 (0.05)	4.47 (0.29)
He II	468.5804	1.04 (0.05)	3.85 (0.33)

Figure 1.11: An adapted table from Alcalá et al. (2017) showing the a and b parameters of the $L_{\rm acc} - L_{\rm line}$ empirical relationship. The particular lines used in this thesis are highlighted in yellow.

demonstrated the importance of discriminating between these two sources of veiling when calculating accretion rates. They found that not including the line emission veiling as a contribution can result in overestimation of the accretion rate by several times.

1.2.3.1 Deriving veiling

With high resolution spectroscopy, it is possible to observe the photospheric absorption lines of a PMS star and the excess due to accretion that veils the spectrum. In Hartigan et al. (1989), a quantitative method was developed to measure the amount of veiling present in a given CTTS. By comparing the spectrum of the accreting CTTS, with a spectrum that represents only the photosphere (no accretion present), the following equation is produced:

$$O(\lambda_i) = A[S(\lambda_i) + V(\lambda_i)], \tag{1.18}$$

where $O(\lambda_i)$ is the observed spectrum of the CTTS, $S(\lambda_i)$ is the template or synthetic spectrum containing only the photospheric flux, $V(\lambda_i)$ is the veiling spectrum (the excess due to accretion), A is a normalisation constant and the index i indicates the specific wavelength being considered ($V(\lambda)$ is the entire veiling spectrum). As it is difficult to measure the veiling across the entire spectrum, it can be measured within a specific wavelength range:

$$O(\lambda_i) = A_j[S(\lambda_i) + k_j], \tag{1.19}$$

where k_j is the excess flux in a specific wavelength interval j (in Hartigan et al. (1989) intervals of $10-15$ Å are used), as opposed to i which indicates an individual wavelength, and A_j is the normalisation at this interval.

The dimensionless quantity veiling commonly used is represented as r_j:

$$r_j = \frac{k_j}{S_j}. \tag{1.20}$$

Hartigan et al. (1989) defines S_{cont} as the estimated continuum level of the template star used for comparison at the wavelength range j. By measuring the amount of veiling in a CTTS, it is possible to quantify the amount of accretion activity happening in the star.

1.3 Ejection

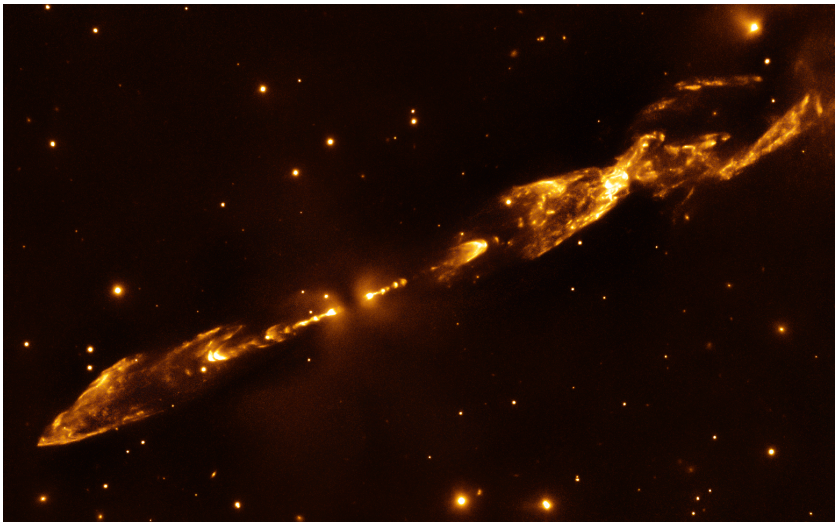

Figure 1.12: HH 212 imaged with VLT/ISAAC, where the pair of jets flow outward from teh central very young object. (*Credit:* ESO/M. McCaughrean)

Outflows are an ubiquitous phenomena found in Class 0, I and II young stars and are probably responsible for aiding the removal of angular momentum of the system (Mestel, 1965), which helps explain why T Tauri stars are such slow-rotators (Bodenheimer, 2011). The material in winds and jets originates from the disk as modeled in Pudritz & Norman (1983), rather than the central star (although see Shu et al., 1987), and are linked closely with the accretion rate of the young star. Just as measuring the mass accretion rate is very important for the study of inflowing material, measuring the mass loss rate can also provide vital information about the processes occurring in the system.

1.3.1 Jets and winds

Outflows and winds can refer to ejected material of differing velocity and origin. Protostars in their earliest stages of YSO, i.e. Class 0 and I sources, produce bipolar molecular outflows that can extend out to 0.1 pc to several pc from the central object (Bodenheimer, 2011). These winds have characteristic velocities of about 20 $\mathrm{km\,s^{-1}}$ and are associated with ongoing accretion. The outflowing emission can be detected both

red-shifted and blue-shifted (unless one lobe is obscured due to the geometry of the system), this is explored for the case of the Class I protostar IRS 54 in Chapter 3.

Jets are a phenomena in which material is flung with very high velocity, (from a few $100\,\mathrm{km\,s^{-1}}$ to $500\,\mathrm{km\,s^{-1}}$, e.g. Marti et al. (1995); Zinnecker et al. (1998); Ray et al. (2007); Pudritz & Ray (2019)) from a star in a bipolar, collimated structure (see reviews of Reipurth & Bally, 2001; Lee, 2020), as shown in Fig. 1.12. These impressive ejections are present in a variety of accreting astrophysical objects such as active galactic nuclei (AGN), black holes, neutron stars, white dwarfs, planetary nebulae and high- and low-mass YSOs (Livio, 2009). The ejected material is launched and gets collimated via magnetic hoop stresses (Pudritz & Ray, 2019), and can travel distances on the order of parsecs away from the central object (Fedriani et al., 2018). As this ejecta flows outward it interacts with the medium and can produce shocks and subsequently, knots. Knots are bright emission regions that occur along the jet's axis, usually spaced out (Zinnecker et al., 1998) and can be seen in Fig. 1.12. Their origins are likely due to the time-variability in the ejection flow velocity from the central object (Raga et al., 1990; Caratti o Garatti & Eislöffel, 2009). Jets have been proposed as a likely solution to how a YSO system removes angular momentum, which has been a problem for many years (Mestel, 1965). Models have been developed for accurately establishing proper motions of these knots (Raga et al., 2015, 2017).

This process of ejection is linked with accretion in all of these systems and is only present when accretion is also present (Edwards, 2008). However, the details of the link between ejection and accretion are still an active topic of study. Observations of HH 30 (Stapelfeldt et al., 1999; Burrows et al., 1996) and DG Tau B (Eislöffel1998 & Mundt, 1998; Stapelfeldt et al., 1997) from the Hubble Space Telescope (HST) provide evidence that the jet originates from the inner accretion disk, relatively near to the central object. This is further confirmed by the velocities of jets being almost always on the order of the escape velocity of the central object of the system, implying the jet is emanating from that central object. Examples of these jets are shown in Fig. 1.13.

Spectroscopic tracers of outflow activity include blue-shifted absorption features ("P-Cygni" features, see Section 1.5) detected in optical permitted emission lines, such as the Hydrogen Balmer series, Na D doublet and Ca II lines. Studies began with spherically symmetric models of winds (Kuhi, 1964; Decampli, 1981; Mundt, 1984; Hartmann et al.,

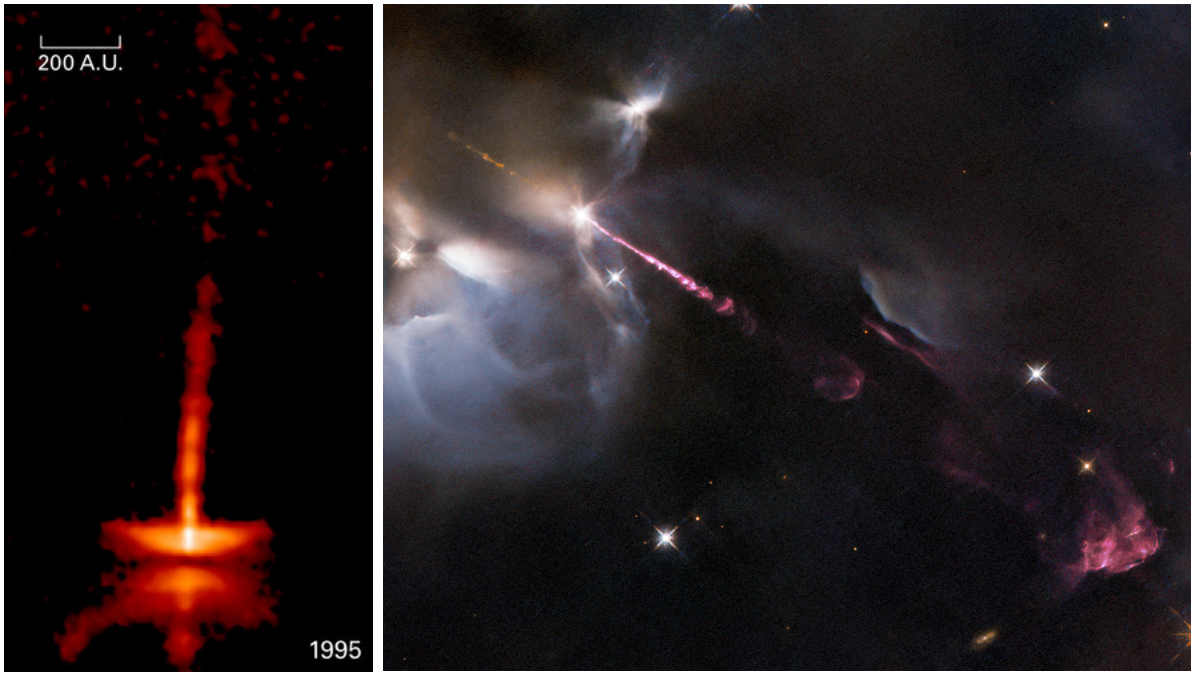

(a) HH 30 (Stapelfeldt et al., 1999; Burrows et al., 1996).

(b) HH 34 (Nisini et al., 2016)

Figure 1.13: Two examples of dramatic jets from protostars.

1990; Natta & Giovanardi, 1990) finding a range of mass-loss rates of $\dot{M}_{\rm loss} \sim 10^{-7} - 10^{-8}\,M_{\odot}\,{\rm yr}^{-1}$ and temperatures in between the range of $T \sim 4{,}500 - 8{,}000\,{\rm K}$. Eventually, more complex modelling without the assumption of spherically symmetric winds was carried out by Calvet & Hartmann (1992) and Johns & Basri (1995a), giving $\dot{M}_{\rm loss} \sim 10^{-8} - 5\times10^{-9}\,M_{\odot}\,{\rm yr}^{-1}$ and $T \sim 8{,}000\,{\rm K}$. The typical values that continue to be used are $\dot{M}_{\rm loss} \sim 10^{-8}\,M_{\odot}\,{\rm yr}^{-1}$ and $T \sim 8,000$ (Johns-Krull, 2009).

More recent studies by Rigliaco et al. (2013), Natta et al. (2014) and Simon et al. (2016) have revisited characterising these slow winds using high resolution spectroscopy of optical forbidden lines such as [O I] , [O II] , [S II] , [N I] and [N II] . These complex lines can contain multiple components that trace different velocities of outflows. The process of decomposing spectroscopic lines will be explained in Section 1.5 and is utilised in the work chapters of 3 and 4.

1.4 YSO variability

Young stars have been known to exhibit variability in their accretion over the course of their evolution. Episodic accretion was proposed to help explain the "luminosity problem", wherein the observed accretion luminosities ($L_{\rm acc} \propto M_\star \dot{M}_{\rm acc}$) were much lower (factors of $10-100$) than what theoretical models predicted (Kenyon et al., 1990, 1994; Kenyon & Hartmann, 1995). Time-variable accretion can explain this because most YSOs are observed in a low-accretion, low-luminosity state, while most of the material is accreted during episodic bursts. Dunham & Vorobyov (2012) developed a model incorporating episodic accretion that agrees with the observed protostellar luminosity distribution, thus resolving the luminosity problem.

It is important to note that in this case, an increase in accretion is associated with an increase in luminosity as more material is accreted, producing stronger shocks than normal close to the stellar photosphere and additional radiation. Two forms this variability can take are FU Orionis-type outburts (FUors) and EXors (confusingly, named after EX Lupi), which were first discovered through optical photometric monitoring, but since then the definition of the phenomenon has been broadened to include more embedded types of young stars (Herbig, 1966, 1977, 1989; White et al., 2007). It is also possible to have extinction effects causing decreases in the observed brightness of a young star, such as in the phenomenon called "dippers" (see Section 1.4.3). FUors exhibit dramatic changes in luminosity of many magnitudes, whereas EXors only show changes of a few magnitudes at optical wavelengths (e.g. Hartmann, 2009, and references therein).

The combination of these effects produce many potential perturbations that need to be accounted for when considering the origins of any observed change in brightness or spectroscopic line profile in a young star, and whether it is an intrinsic variability. Figure 1.14 illustrates the different kinds of variability seen in YSOs and how they are not distinct categories, but overlap often. Some of the kinds of variability in Fig. 1.14 are beyond the scope of this thesis and not discussed here.

1.4.1 FUor-type outbursts

FUors are stars that exhibit very large increases in accretion that last over relatively short time scales ($\sim 10^2$ years) and have been observed to accrete $\sim 10\%$ of their

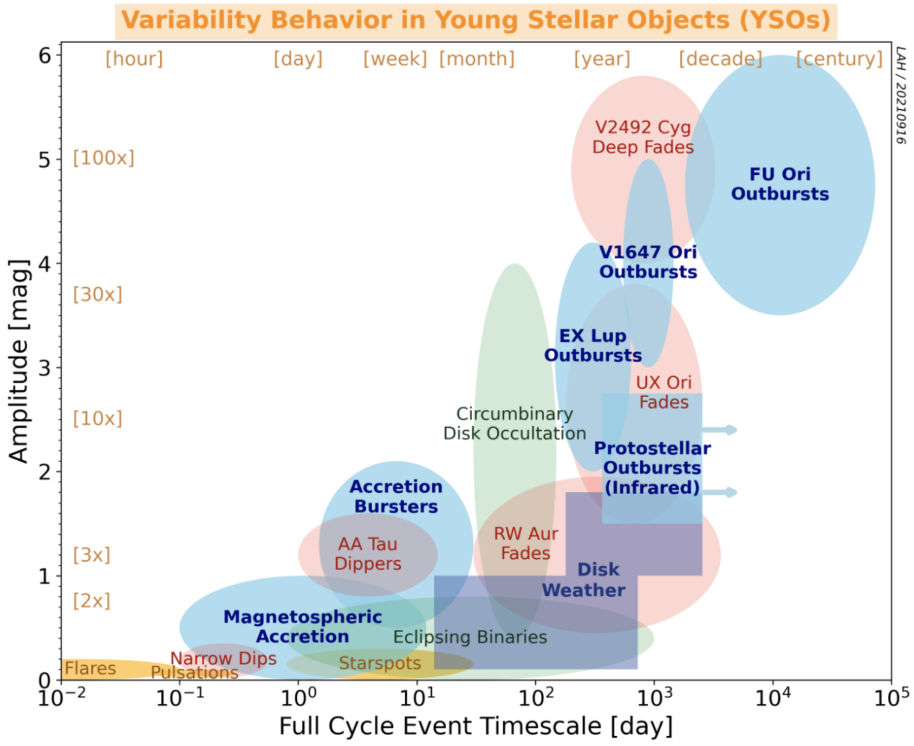

Figure 1.14: A figure from Fischer et al. (2022) illustrating the different types of YSO variability known in terms of their cycle length and magnitude of the change. Blue indicates the accretion-related events, purple indicates routine variabilities (brightening or dimming), red indicates dimming (extinction-related) behaviour, yellow indicates stellar phenomena, and green indicates binary-related variability. (Fischer et al., 2022)

mass during these bursts over the course of their formation (Hartmann, 2009). It is believed these kinds of dramatic bursts preferentially occur during the early stages of star formation, when mass is still falling onto the disk from an envelope. The increased use of IR observations have helped shed light on these phenomena as embedded objects are difficult to study at optical wavelengths. Mass accretion rates of $\dot{M}_{\rm acc} \sim 10^{-4} M_{\odot} yr^{-1}$ have been inferred in order to explain the observed spectra and accretion luminosities (Hartmann, 2009). This is several $(3-4)$ orders of magnitude higher than the quiescent phase of these young stars, and might accrete up to $\sim 30-40\%$ of their final mass during these bursts over the course of their formation (Fischer et al., 2019). What causes these violent bursts is still under investigation, however, a possible explanation involves an unstable piling up of infalling matter on the disk that results in a sudden burst as this instability is eliminated by rapidly accreting the material onto the star. This has been predicted on smaller scales in MHD models of the inner disks of CTTSs (Romanova

et al., 2009; Hillenbrand & Findeisen, 2015, e.g.).

1.4.2 EXor - type bursts

EXors are phenomena that occur over shorter timescales ($\sim 1-2$ years) and are less violent ($\dot{M}_{\rm acc} \sim 10^{-6} M_{\odot}\,{\rm yr}^{-1}$) than their FUor counterparts (Audard et al., 2014). The brightness of these objects can increase by several magnitudes over mere months, according to photometric observations (e.g. Audard et al., 2010). Their frequency is also greater than FUors, with bursts occurring potentially only a few years apart (Herbig, 2008). This large increase in brightness is believed to be caused by an increase in accretion activity, and can be measured using the mass accretion rate ($\dot{M}_{\rm acc}$). In addition to changing in brightness, EXors can demonstrate different spectral features during a burst than in quiescence that can aid their identification. Many of these features, CO bandheads ($2.3-2.4\,\mu$m) in emission, the Na I doublet ($2.206\,\mu$m), and sometimes Ca I ($2.267\,\mu$m) exist in the NIR, however, since they originate from the inner disk it may be difficult to observe if the geometry of the system is not ideal (Lorenzetti et al., 2009).

Similar to FUors, most EXors observed are T Tauri stars in quiescence. However, there is evidence that earlier stage protostars also exhibit these episodic bursts (Audard et al., 2014), and it has been found that in Class I YSOs, that eruptive variability of the EXor - and FUor - type is at least an order of magnitude more common than in Class II YSOs (Contreras Peña et al., 2017). Again, the increased use of infrared observations has helped shed light on these phenomena, as embedded objects are difficult to study at optical wavelengths.

1.4.3 Dimming variability

In addition to increases in the brightness of YSOs, there can also be dimming effects that have been observed to be both periodic and aperiodic (e.g. Herbst et al., 2000). The irregularity in which some of these stars (i.e. UXor - types, RW Aur and AA Tau) dim suggests an occultation of the line-of-sight by dust (Alencar et al., 2010; Bouvier et al., 2013). This wavelength-dependent phenomenon is attributed to extinction and thus dust grains passing between the observer and target, absorbing the emitted light and then re-emitting it at longer wavelengths. As discussed in Section 1.1, this effect is observed in protostars (Classes 0 and I) as a NIR excess, resulting from the absorption

of UV and optical emission and subsequent re-emission in the NIR (Nisini, 2008).

1.4.3.1 UXor - type dimming

UXor - type stars present a particular kind of aperiodic dimming. These stars demonstrate dimming events caused by a severe puffing-up of the very inner disk due to a thermal instability (Natta et al., 2001; Dullemond et al., 2003; Pontoppidan et al., 2007). They are typically observed edge-on which allows such a dimming to be noticeable on the plane of the sky. These aperiodic extinction events are relatively frequent and last on the order of days to weeks (Pontoppidan et al., 2007). The authors in Dullemond et al. (2003) concluded that this is due to a "self-shadowed" disk where the outer disk lies in the shadow of the puffed-up rim of the inner disk.

1.4.3.2 Dippers

Young stars that demonstrate a reduction of brightness ($1 - 2\,\mathrm{mag}$) and then a return to their original brightness are called "dippers" and present an open question as to the exact origin of their dimming events (Contreras Peña et al., 2017; Pinilla et al., 2018; Koutoulaki et al., 2019a). Many of these dimming events have been investigated with respect to the star-disk interaction and impact of warped and asymmetric disk geometries on the observed brightness of the YSO (Ansdell et al., 2016; Pinilla et al., 2018; Dodin et al., 2019a; Nealon et al., 2019).

1.4.3.3 Dimming related to hot/cold spots

Additionally, periodic variabilities in brightness of YSOs can be due to hot and cold spots on the stellar surface moving in and out of view as the star rotates. These periodic signals have been used to measure the rotation period of young stars (e.g. Herbst et al., 2000; Donati et al., 010a,b). Spectroscopically, the stellar rotation can also be manifest in the profiles of emission lines when accretion is appropriately high (i.e. CTTSs). Depending on the inclination angle, this rotation can make the accretion columns that are flowing from the disk onto the stellar surface appear more or less blue- and red-shifted depending on their orientation at a given phase of the rotation period, as well as modulate the emission lines' equivalent widths (e.g. Johns & Basri, 1995b; Kurosawa et al., 2005; Costigan et al., 2014). However, it is also possible to characterise stellar rotation in low-

mass stars during low accretion rates when the accretion columns are non-axisymmetric and the spectral resolution and SNR are high enough (e.g. Sicilia-Aguilar et al., 2015; Gahm et al., 2013; Campbell-White et al., 2021).

1.5 Spectroscopy

Spectroscopy is one of the most useful tools for analysing the electromagnetic radiation emitted from everything from exoplanets to stars to distant galaxies. Specifically, the profiles of emission and absorption lines can provide an incredible amount of information about the chemical composition and kinematics of the source. This thesis utilises spectroscopic line diagnostics at optical and IR wavelengths in order to determine physical parameters of proto- and pre-main sequence stars.

The intensity of radiation emitted from a source depends predominantly on the source's radius, temperature, density and its distance from the observer. To measure this, one can look first to the total energy emitted from the object per area per unit time and how it depends on the temperature of the object. The Stefan-Boltzmann Law does this by defining a constant (σ) that applies when the source is in thermal equilibrium (Stefan, 1879; Boltzmann, 1884):

$$L = 4\,\pi\,R^2\,\sigma\,T^4, \quad \text{where } \sigma = 5.67 \times 10^{-8}\,[\mathrm{W\,m^{-2}\,K^{-4}}]\,, \tag{1.21}$$

and L is the luminosity.

The most efficient radiating and absorbing body at any temperature is defined to be a "black body". For every possible temperature, a black body curve can be plotted across all wavelengths with respect to intensity, and will peak at a characteristic wavelength (λ_{peak}) dependent on that temperature (see Fig. 1.15). How this peak intensity shifts with wavelength is shown in Fig. 1.15 as the black dashed line: λ_{peak} moves toward longer wavelengths for curves of lower temperature. This inverse proportionality between λ_{peak} and temperature (for a black body) was described by Wilhelm Wien in 1893 by introducing a constant, Wien's displacement constant:

$$\lambda_{\mathrm{peak}} = \frac{2.898 \times 10^7\,[\mathrm{\AA}]}{T/[\mathrm{K}]}\,. \tag{1.22}$$

This has been known since as Wien's displacement law. The spectrum of a black

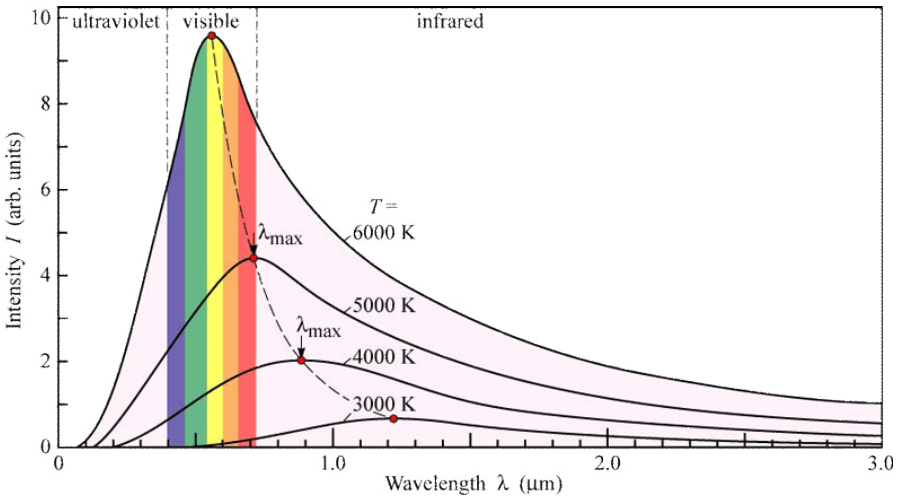

Figure 1.15: Black body spectra at different temperatures. The y-axis is given in arbitrary units of intensity and the x-axis is in terms of microns (μm). Each curve represents a different temperature of the emitting body and the dashed black line shows how the peak intensity of each curve moves toward longer wavelengths at lower temperatures (Dodd et al., 2006).

body that encompasses this displacement law is described by the Planck distribution function (B_ν) which defines the luminosity-frequency (or luminosity-wavelength, B_λ) relationship at a given temperature $T_\star$ (Planck, 1901):

$$B_\nu(T_\star) = \frac{2h\nu^3}{c^2} \frac{1}{e^{(h\nu/kT_\star)} - 1}\,, \tag{1.23}$$

where $T_\star$ is the radiation temperature of the star, ν is the frequency of the radiation, h is Planck's constant ($h = 6.626 \times 10^{-34}\,\mathrm{J\,Hz^{-1}}$), k is Boltzmann's constant ($k = 1.381 \times 10^{-23}\,\mathrm{J\,K^{-1}}$) and c is the speed of light ($c = 2.998 \times 10^{8}\,\mathrm{m\,s^{-1}}$). In the case of our Sun with a surface temperature of $T = 5770\,\mathrm{K}$, the peak intensity of its emission spectrum is in the visible, yellow specifically, at $\lambda_{\mathrm{peak}} = 5500$Å (see Fig. 1.15).

Observationally, no object acts as a perfect emitter or absorber, however, looking at a black body of the same temperature as the object provides the underlying continuum shape without perturbations from spectral features (Pradhan & Nahar, 2011).

Such spectral features include emission lines, absorption lines and spectral bands. Spectral lines represent a specific atomic (or molecular) transition which occurs at a specific wavelength, where emission lines produce a line in excess to the continuum level, absorption lines produce a line below the continuum level and spectral bands occur when there are many spectral lines closely spaced and arranged in a regular sequence (Pradhan

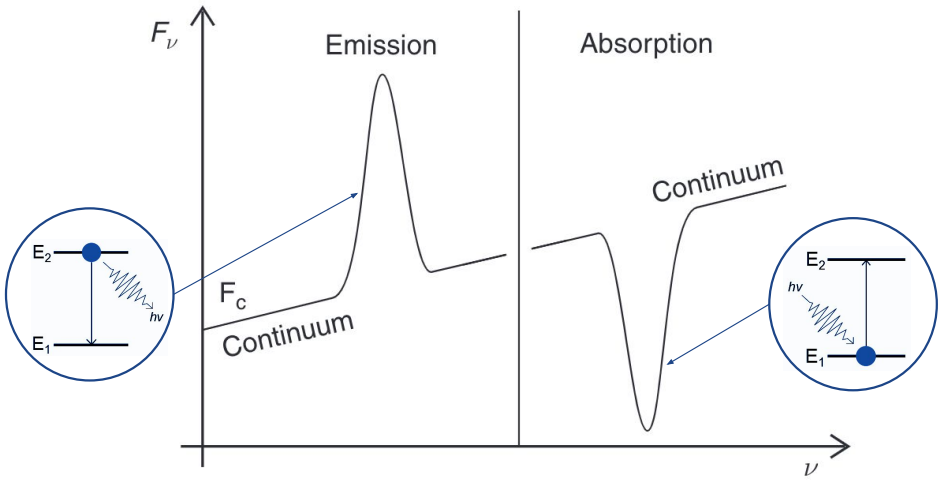

Figure 1.16: A figure demonstrating the difference between emission and absorption lines in a spectrum. Adapted from Pradhan & Nahar (2011).

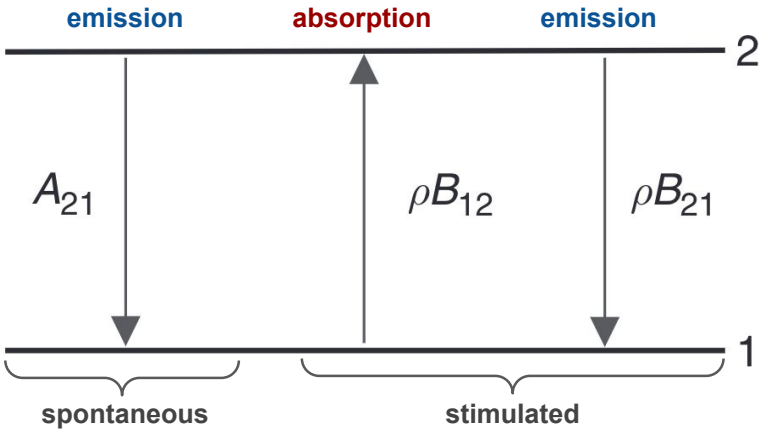

Figure 1.17: A figure demonstrating the possible transitions of an atom between two levels. Adapted from Pradhan & Nahar (2011).

& Nahar, 2011). These transitions occur from the jumping up and down between energy levels of electrons which either emit or absorb photons (see Fig. 1.16). For a given atom, X, these photo-excitation and de-excitation processes can be expressed generally as:

$$X + h\nu \rightleftharpoons X^* \,, \tag{1.24}$$

where $h\nu$ is a discrete quanta of energy (a photon) and X^* represents an excited state of X.

The probability of a given transition is represented by its Einstein coefficients A and B. Einstein postulated three distinct radiative processes that occur between two

levels: spontaneous decay (A_{ji}), stimulated emission (B_{ji}) and absorption (B_{ij}), as seen in Fig. 1.17. While spontaneous decay depends only on the number population of the upper level (N_j), the emission and absorption due to an external radiation field depend on both the level populations (N_j and N_i) and the density of that external field $\rho(\nu)$. The emission and absorption processes can be related through Kirchhoff's Law that states they are equal (under thermal equilibrium):

$$\rho_{12}B_{12}N_1 = A_{21}N_2 + \rho_{21}B_{21}N_2, \tag{1.25}$$

where the left hand side of the equation represents the absorption process and the right hand side represents the two emission processes. In the case of no external radiation field, $\rho(\nu) = 0$ and one can solve for A_{ji} such that it decreases exponentially with time, and leads to the definition of the lifetime (τ_j) of level j:

$$A_{ji} \equiv \frac{1}{\tau_j}, \tag{1.26}$$

where A_{ji} has units of [s^{-1}]. The Einstein coefficient for stimulated emission (B_{ji}) depends on A_{ji} in the following way, when the external field is assumed to be a blackbody given by the Planck function ($\rho(\nu) = \frac{8\pi\nu^2}{c^3}\frac{h\nu}{\exp(h\nu/kT)-1}$):

$$B_{ji} = \left(\frac{c^3}{8\pi h\nu^3}\right) A_{ji}, \tag{1.27}$$

at a specific frequency (ν). From this equation, it is apparent that $B_{ji} \propto \lambda^3 A_{ji}$ which means B_{ji} increases rapidly with λ and is dominant at longer wavelengths, for example at microwave wavelengths, where stimulated emission is more likely than at shorter wavelengths (Pradhan & Nahar, 2011). In this thesis, I am working at optical and NIR wavelengths, and therefore, only require the use of A_{ji} when studying the emission transitions seen in the spectra. Specifically, when looking at emission line ratios of [FeII] in the NIR, the A_{ji}'s of the two transitions are used to calculate the extinction (see Section 2.3.2). The values of these Einstein coefficients can be calculated or measured in a laboratory. Here I take them from Nussbaumer & Storey (1988) where the authors calculate A_{ji} for the infrared [FeII] lines.

1.5.1 Line broadening

The line profile of a spectral line is one of the best tools available to astrophysics for probing the kinematics and conditions of radiating astrophysical objects. The changing shape and width of a line is due to both the atomic transitions producing the line and the environment in which the atoms find themselves, this is called broadening. Natural broadening, pressure (or "collisional") broadening, Doppler broadening due to bulk motion of the gas or plasma and Zeeman broadening are examples of processes that can warp the observed shape of spectral lines. The convolution of all these different distributions is necessary to determine the line profile of a given atom.

Firstly, the natural line width is effected by radiation damping which is related to the radiative decay rates for the energy levels involved in a transition. It is defined by the uncertainty principle $\Delta E\,\Delta t \geq \hbar$ and is inversely proportional to the radiative lifetime of an excited state (Mihalas, 1978). This effective broadening is represented by a Lorentzian profile.

The processes at work behind pressure broadening are complex and involve effects from the plasma density, temperature, excitation energies of atomic levels and electric fields ("Stark broadening") (see Pradhan & Nahar, 2011, for a detailed explanation). This combination of effects is beyond the scope of this thesis, however, it is notable that the net profile from pressure broadening takes the form of a Lorentzian profile, as is the case for natural broadening.

Doppler broadening is the byproduct of the Doppler effect wherein the frequency of radiation emitted by an atom is observed to be higher when the source is moving towards the observer and vice versa (Stahler & Palla, 2004; Pradhan & Nahar, 2011). This is seen especially in systems where an emitting body is rotating, as the emission source is moving in and out of view on the plane of the sky, changing its angle with respect to the observer. The line shape of Doppler broadening due to thermal and turbulence is a Gaussian function:

$$\Phi_\nu = \frac{1}{\sqrt{\pi}\,\Delta\nu_D}\, e^{-\left(\frac{\nu-\nu_0}{\Delta\nu_D}\right)^2}, \tag{1.28}$$

where ν is the frequency of the given line in the observer's frame, ν_0 is the line frequency in the rest laboratory frame and $\Delta\nu_D$ is the Doppler width, defined in the case of no

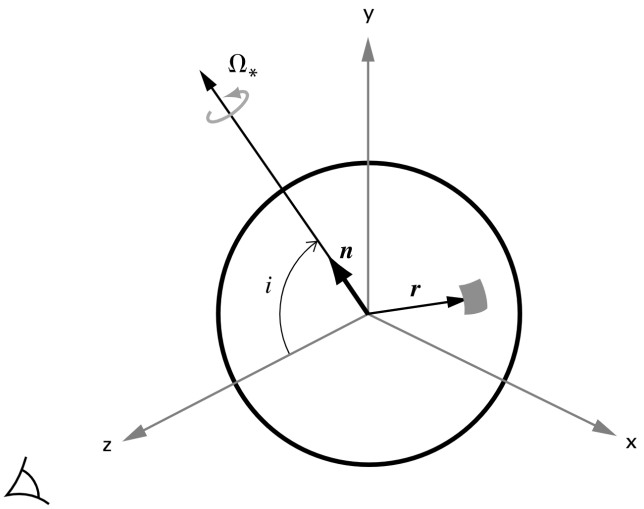

Figure 1.18: The geometry of a rotating star (Stahler & Palla, 2004).

bulk motion, such as rotation, as:

$$\Delta\nu_D = \sqrt{\frac{\nu_0}{c^2\left(v_{\rm therm}^2 + v_{\rm turb}^2\right)}}\ , \tag{1.29}$$

where $v_{\rm therm}$ is the thermal velocity contribution to the broadening and $v_{\rm turb}$ is a contribution due to the micro-turbulent motions of the gas particles. The thermal velocity contribution in the gas is generated through the movement of the atoms, molecules and ions, dependent on their temperature:

$$v_{\rm therm}^2 = \frac{2kT}{m_i}\ , \tag{1.30}$$

where m_i is the mass of the particles in question. Because the frequency of a Doppler shift depends on the velocity of the atom, which itself depends on the ambient temperature, the result is a contribution to the total broadening that directly measures the temperature.

Additionally, Doppler broadening of a line profile allows an observer to determine the projected rotational velocity ($v \sin i$) of a rotating source (Gray, 2005). As shown in Fig. 1.18, $\Omega_\star$ is the angular speed of the rotation of a star of radius $R_\star$. If the point being measured is at radius $\boldsymbol{r} = (x, y, z)$ from the origin (the small grey square in Fig. 1.18), its rotational velocity is:

$$\mathbf{v} = \Omega_\star\, \hat{\mathbf{n}} \times \mathbf{r} \tag{1.31}$$

where $\hat{\mathbf{n}} = (0, \sin i, \cos i)$ is a unit vector along the axis of rotation. The amount of Doppler shift will depend on the v_z component, which is defined as:

$$\begin{aligned} v_z &= -x\,\Omega_\star \sin i \\ &= -\frac{x}{R_\star} V_{\rm eq} \sin i\,, \end{aligned} \tag{1.32}$$

where i is the inclination angle with respect to the z-axis and $V_{\rm eq} = \Omega_\star R_\star$ is the equatorial velocity of the star (Stahler & Palla, 2004). Often this $V_{\rm eq}$ is just left as v, hence the notation "$v \sin i$" to describe the projected rotational velocity of the star.

A young star with hot or cool spots will be observed to have a changing line profile (blue- and red- shifts) due to changing amounts of Doppler broadening corresponding to the prevailing rotational phase, as shown in Fig. 1.19 (Reiners et al., 2013).

The final source of broadening discussed is Zeeman broadening: a consequence of Zeeman splitting in the presence of a magnetic field (see Reiners, 2012, and references therein), the nuances of which are left out in the interests of brevity. When undergoing a transition from one energy level to another, an electron will encounter altered levels when coming into contact with a magnetic field. Each energy level will split into $2J+1$ states, where J is the total angular momentum quantum number, and each of these states will have a different magnetic quantum number m where $\Delta m = -1, 0, +1$. This effect can be quantified in terms of either a wavelength ($\Delta\lambda$) or velocity (Δv) shift:

$$\begin{aligned} \Delta\lambda &= 46.67\, g\, \lambda_0^2\, B \quad [\text{mÅ}] \\ \Delta v &= 1.4\, \lambda_0\, g\, B \quad [\text{km s}^{-1}]\,, \end{aligned} \tag{1.33}$$

where λ_0 is the initial wavelength of the transition in μm, g is the energy level dependent Landé factor (see Reiners (2012) for details about g) and B is the magnetic field strength in kG.

The inclusion of Zeeman broadening in the convolution of all broadening processes does not always have a large effect, in contrast to the much stronger effects of the pressure and Doppler broadening. Even in a kG strength magnetic field, the Zeeman splitting is only on the order of 1 km s^{-1} at optical wavelengths, which would require an

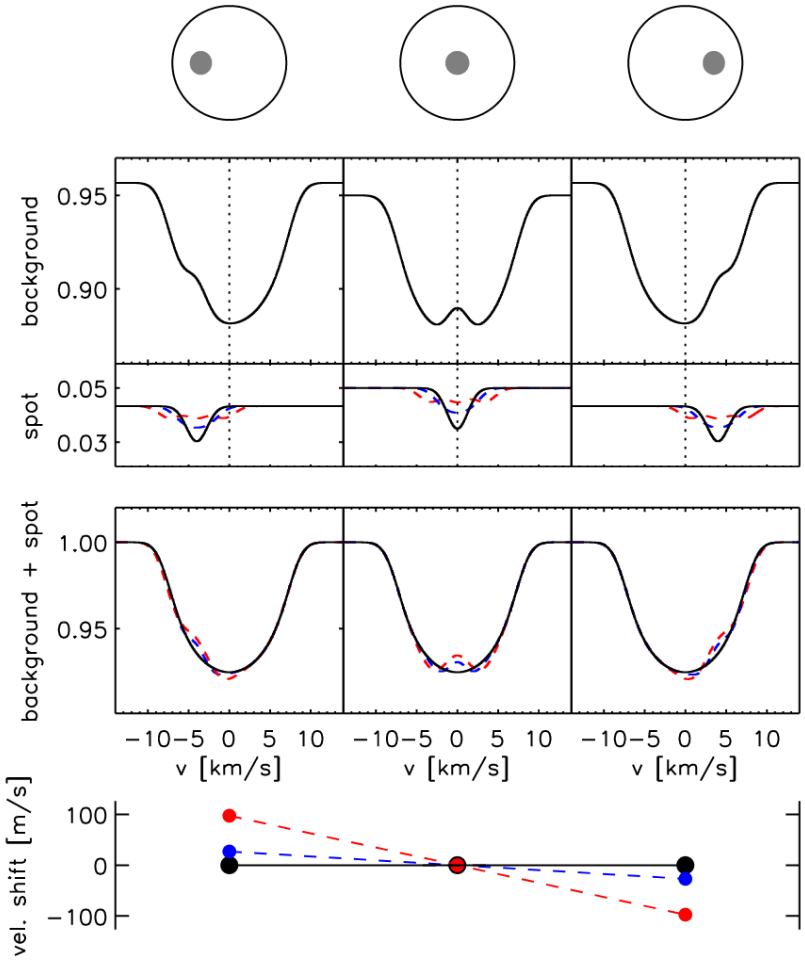

Figure 1.19: An example of Doppler Broadening in hotspots on a young star. The different location of the hotspot moves as the star rotates, producing different spectroscopic signatures (Reiners et al., 2013).

especially high resolution spectrograph to detect and, more importantly, is below most intrinsic line widths. To detect the Zeeman effect, which has been done sucessfully in some proto- and pre-main sequence stars (e.g. Donati et al., 1997; Johns-Krull et al., 1999), these obstacles can be overcome by choosing a target star with a particularly large magnetic field ($> 1\,\mathrm{kG}$) and observing at longer wavelengths, i.e. the infrared. Because the Zeeman broadening effect scales as $\Delta\lambda \propto \lambda^2$, (as opposed to the Doppler effect which scales as $\Delta\lambda \propto \lambda$), an increase in wavelength produces that increase amount squared of Zeeman broadening of the line (Schulz, 2005). Similarly, the observation of the Zeeman effect as a tool to calculate magnetic fields has been done using IR lines in main sequence stars for quite some time (see e.g. Saar & Linsky, 1985).

The final convolution of these broadening phenomena is the combination of Gaussian and Lorentzian distributions, producing a Voigt function (Gaussian $\circledast$ Lorentzian $\rightarrow$ Voigt). The profile of these two functions are different: the Lorentz distribution falls off much slower than a Gaussian and has a lower peak intensity). Therefore, the Gaussian component dominates the line core (thermal broadening components) and the Lorentzian dominates in the wings (natural and pressure broadening components).

2

Observational techniques and diagnostics

Figure 2.1: One of the Unit telescopes of the Very Large Telescope in Chile on Cerro Paranal, shining its guide star laser into the night sky. *Credit:* ESO

When one imagines the field of astronomy often the beautiful pictures of stars, galaxies and nebulae come to mind (such as Fig. 2.1). However, images and spectra are not taken looking this beautiful, it takes a lot of hard work reducing observing data to create the final product. There are many difficulties involved in taking data of the night sky, especially when doing so from the ground and not a space telescope. The two primary techniques used in this thesis are spectroscopy and photometry. These kinds of observations are obtained from imagers and spectrgraphs mounted on impressive telescopes all over the world in particularly high-up and often dry places.

2.1 Observing Techniques

Depending on the wavelength range of the detector, there are different limitations the atmosphere imposes (when using ground-based telescopes). Figure 2.2 shows the transmittance of the atmosphere as a function of wavelength, specifically the visible ($\sim 0.4 - 0.9\,\mu$m), NIR ($\sim 1.0 - 2.5\,\mu$m), MIR ($\sim 5 - 25\,\mu$m) and FIR ($\sim 25 - 350\,\mu$m).

Band	λ (μm)	Range
B	$0.4 - 0.5$	optical
V	$0.5 - 0.7$	optical
R	$0.55 - 0.8$	optical
I	$0.7 - 0.9$	optical
J	$1.17 - 1.33$	NIR
H	$1.49 - 1.78$	NIR
K	$2.03 - 2.20$	NIR
$W1$	$2.74 - 4.06$	MIR
$W2$	$3.56 - 5.64$	MIR

Table 2.1: Wavelength ranges of the optical, NIR and MIR filter bands used in this thesis. $W1$ and $W2$ refer to the first two WISE (Wide-field Infrared Survey Explorer) filters.

Transmittance is the percentage of light that can pass through the atmosphere, which strongly influences what observations are possible for ground-based telescopes and what wavelengths of light are only observable from space.

It is vital in astronomy to not only be aware of these limitations, but have a way to quantify and remove them. An important piece to this puzzle is the point spread function (PSF), the diffraction image of a point-like source through the telescope's optics system, which is deconvolved with the raw image to obtain the science image. The ideal FWHM of the PSF of a circular aperture, in the absence of atmospheric effects is given as:

$$\theta = \frac{\lambda}{D} \text{ [rad]} , \tag{2.1}$$

where λ is the operating wavelength and D is the diameter of the telescope. A cross-section through the center of this idealised PSF is a Gaussian function. However, as a measure of the response of a specific optics system, the PSF is not ideal or the same for different telescopes. It can be modeled as the power spectrum of the Fourier transform of the aperture:

$$\text{PSF}(\boldsymbol{\alpha}) = |\,\text{FT}\,[W(\boldsymbol{\alpha})]\,|^2 \tag{2.2}$$

where FT is the Fourier transform, $\boldsymbol{\alpha}$ is a vector concerning the coordinates of a point in the focal plane, and $W(\boldsymbol{\alpha})$ is the pupil function of the telescope – a representation of how light transmits through the telescope (Goodman, 1995, and references therein).

In reality, the width of the PSF is often set by the night's particular atmospheric conditions, which demonstrates the dramatic effects Earth's turbulent atmosphere can

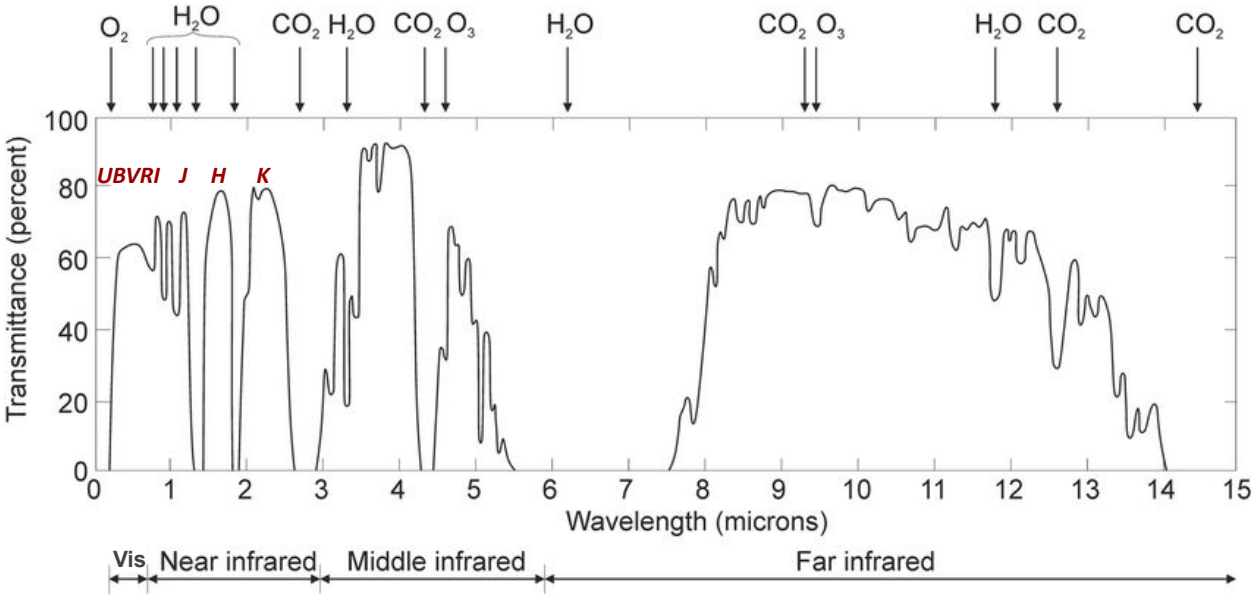

Figure 2.2: The transmittance (%) of the atmosphere (the amount of light passing through the atmosphere), as a function of wavelength. The optical, NIR, MIR and FIR wavelength ranges are shown on the bottom of the plot and the absorbing molecules are shown above the plot. The dark red letters correspond to the optical and NIR wavelength bands.

have on ground-based observations (Esposito & Pinna, 2008). Light leaving a star reaches the Earth's atmosphere and is then scattered by refractive inhomogeneities. Because the light waves propagating through the atmosphere experience amplitude and phase fluctuations, this turbulence limits the angular resolution and contributes to the "seeing" of an observation. The seeing is defined as the FWHM of the seeing disk (the observed image of the source), and subsequently changes from day to day. To put the importance of this in context, in the ideal case of Eq. 2.1 for one of the 8.2 m UTs (unit telescopes) at Paranal Observatory in Chile, observing a source at $\lambda = 1.0\,\mu$m, the width of the PSF would be $0.02''$ (1.22×10^{-7} rad). This is > 30 times smaller than the actual seeing observed on a given night. A seeing of $1.0''$ is considered decent to produce a sharp image, however, modern large ($8-10$ m) telescopes (e.g. Paranal Observatory and Mauna Kea Observatories) are able to attain much better effective seeing ($\sim 0.1''-0.4''$, wavelength-dependent) with the help of adaptive optics (AO) systems that adjust a telescope mirror in real time to account for atmospheric fluctuations[1] (Dougados, 2008;

[1]The live seeing at the Mauna Kea site can be found at: `http://mkwc.ifa.hawaii.edu/current/seeing`, where it shows measurements of seeing using the two instruments, DIMM (Differential Image Motion Monitor) and MASS (Multi-Aperture Scintillation Sensor) (Kornilov et al., 2007; Tokovinin & Kornilov, 2007), commonly used to measure atmospheric turbulence Lyman et al. (2020). A discussion of similar monitoring at Paranal Observatory can be found in Milli et al. (2019).

Whelan & Garcia, 2008). When dealing with spectroscopy, the spectral resolution can be found as $R = \lambda/\Delta\lambda$.

More science has been done, in the past, at optical wavelengths as it is rather intuitive (our eyes are designed for detecting optical light) and because the atmosphere is relatively transparent at these wavelengths. Observations analysed in this thesis are predominantly within the optical and NIR wavelength ranges. Although the optical spectrum suffers less from atmospheric effects, it is unable to probe through the dust that surrounds protostars, especially Class 0 and I. NIR observations are able to access regions of higher extinction than the optical allows (e.g. $A_K \simeq 0.1 A_V$), ideal for Class I protostars, and even longer wavelengths such as the sub-millimetre provide access to the even higher extinctions found in Class 0 objects. However the NIR too has limitations, namely the H_2O absorption from the atmosphere separating the J, H and K bands (see Fig. 2.2). Additionally, OH emission is prevalent in this same range, and these contaminating emission lines need to be removed during the spectroscopic data reduction process.

2.1.1 Telluric lines

A specific form of atmospheric contamination appearing in spectra are telluric lines, which are especially prevalent at optical and NIR wavelengths both in absorption and emission. Water (H_2O) and Oxygen (O_2) molecules are primarily responsible for these narrow absorption lines in the these ranges (Curcio et al., 1964; Moehler et al., 2014; Langeveld et al., 2021, and references therein). Not only are these contaminating lines present, but they vary in wavelength due to pressure changes and wind along the line of sight. Additionally, they vary in line strength depending on the location of the telescope, the weather and the airmass during the observations. These telluric lines need to be removed because they often blend with the target source's actual absorption and emission lines, introducing further uncertainties in measurements. There are many methods currently being used to remove telluric lines from stellar spectra, often specific to the particulars of an individual study (e.g. Moehler et al., 2014; Gullikson et al., 2014; Smette et al., 2015; Rudolf et al., 2016; Langeveld et al., 2021; Allart et al., 2022). These include (1) generating a simulated telluric absorption spectrum to subtract from the science spectrum, (2) comparing the science spectrum with a standard star's spectrum observed simultaneously with the same instrument and (3) identifying and removing telluric lines one by one. The first of these methods is ideal, however, necessitates complex radiative transfer models and information about the night's specific observing conditions. The second method requires more telescope time and it can be costly to

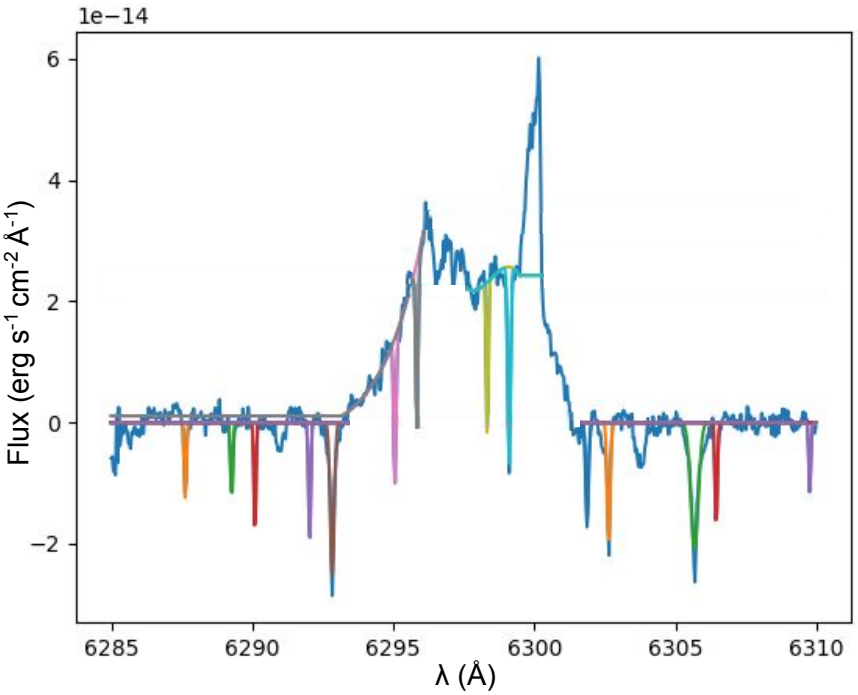

Figure 2.3: Telluric absorption lines identified in and close to the [O I] 6300Å emission line in RU Lup. See Chap. 4 for the analysis done with this spectral line. The colours are merely the individual fits done one by one for the telluric lines.

observe a standard star. Moreover there will be slight differences in airmass between the observations of the standard and the science target (Moehler et al., 2014, and references therein). This is the method used to remove telluric lines in the ISAAC spectra of Chap. 3. The final method's efficiency depends heavily upon how large the spectrum containing telluric lines is and how blended they are with other spectral features. In the case of Chap. 4, the region requiring telluric removal was small (~ 10 Å), and the spectral resolution high enough, that this third method was satisfactory. This can be seen in Fig. 2.3 where a segment of the spectrum of RU Lup centered at the [O I] 6300 Å emission line is shown in blue, and the multi-colored lines trace the absorption telluric lines that were fit in the Python code so as to be removed. It should be noted that there also exists a telluric emission line due to H_2O that blends with the narrow component of the [O I] 6300 Å emission line and also was removed from the RU Lup spectra.

2.2 Instruments

2.2.1 ESO/VLT

The European Southern Observatory (ESO) is an international organisation providing astronomers with state-of-the-art ground-based telescopes in the southern hemisphere. Of its 16 member states, Ireland became a member during the first year of my PhD and opened the door to many more opportunities to utilise ESO's Very Large Telescope (VLT).

Figure 2.4: Top panel: Three of the Four UT's at the Very Large Telescope atop Cerro Paranal (*Credit:* ESO/B. Tafreshi twanight.org). **Bottom left panel:** The ISAAC instrument being carried up the mountain in a truck to be mounted at the VLT in 1998 (*Credit:* ESO, 1998). **Bottom right panel:** The SINFONI instrument being lifted for mounting on the one of the UTs at the VLT (*Credit:* ESO/Max Alexander, 2012).

Atop Cerro Paranal in the Chile's Atacama Desert, ESO's telescope facility, the VLT, operates four 8.2 m Unit Telescopes (UTs) and four 1.8 m movable Auxiliary Telescopes (ATs). Each UT is fitted with a rotating ensemble of spectroscopic and interferometric instruments studying wavelengths of light spanning from the deep ultra violet (0.3 μm) to the mid-infrared (24 μm). The top panel of Fig. 2.4 shows a beautiful image of three of the four UTs with their domes open, ready to observe the night sky. The specific

instruments at the VLT used in this thesis are described below and can be seen in Fig. 2.4.

ISAAC

Although decommissioned in 2013, the Infrared Spectrometer and Array Camera (ISAAC, Moorwood et al., 1998) was mounted on the Nasmyth A focus of UT3. ISAAC was equipped with two independent arms, for observations at short wavelengths (SW) and long wavelengths (LW), respectively. The SW arm, a 1024×1024 Hawaii Rockwell array, could observe at wavelengths of $1 - 2.5\,\mu$m. The LW arm, an Aladdin 1024×1024 array, could observe at wavelengths of $3 - 5\,\mu$m. ISAAC's spectral resolution was $R \sim 10,000$. The slit length in ISAAC was $120''$ and the slit width had four possible settings: $0.3''$, $0.6''$, $0.8''$, $1.0''$, $1.5''$ or $2.0''$. The pixel scale was 146 milliarcseconds (mas). The imaging capabilities of ISAAC provided Js, J, H and Ks band photometry as well as narrow band (NB) imaging at wavelengths where notable emission lines are present (e.g. NB 2.17 μm observes the Brγ line). The FOV of the imager of the SW arm was $152'' \times 152''$, and there were no adaptive optics in use on the instrument. This instrument provided exquisite coverage of the spectral range needed to study young stellar objects and their accretion and ejection properties. The ISAAC instrument is used in Chapter 3. ISAAC can be seen being brought up Cerro Paranal in a truck to find its home at the VLT in 1998 in the left panel of Fig. 2.4. An example of an impressive ISAAC image can be found in Fig. 1.12 of HH 212.

SINFONI

Also now decommissioned (as of 2019), the Spectrograph for INtegral Field Observations in the Near Infrared (SINFONI, Eisenhauer et al., 2003) was installed at the Cassegrain focus of UT4. SINFONI was an integral field unit (IFU) fed by an adaptive optics module and fitted with a Hawaii 2RG 2048×2048 detector array. The spectrograph operates four gratings: J, H, K and $H + K$ with $R \sim 2000$, 3000, 4000 and 1500, respectively. The fields of view can be $8'' \times 8''$, $3'' \times 3''$ or $0.8'' \times 0.8''$. Each wavelength channel is imaged which produces a cube of data of the target. SINFONI's IFU capabilities are demonstrated in the study discussed in Chapter 3 to investigate the morphology of the extended emission in the Class I protostar IRS 54. SINFONI can be seen getting mounted on one of the UTs at Cerro Paranal in the right panel of Fig. 2.4.

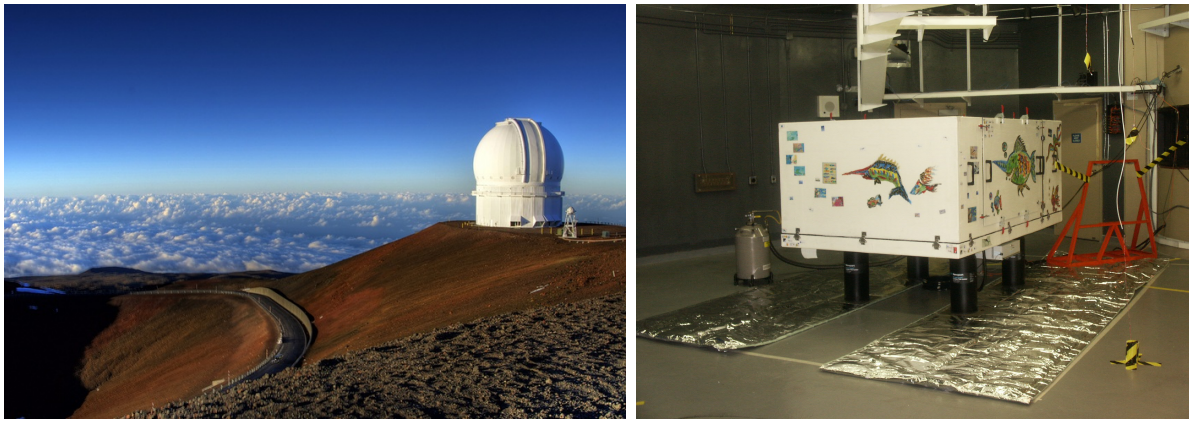

Figure 2.5: Left panel: One of the domes of the CFHT atop the dormant volcano Mauna Kea on the big island of Hawaii (*Credit:* CFHT). **Right panel:** The ESPaDOnS stectropolarimeter at the CFHT, covered in swordfish art (*Credit:* CFHT).

2.2.2 CFHT

The Canada-France-Hawaii Telescope sits close to the peak of Mauna Kea, a 4200 m dormant volcano, on the big island of Hawaii. It is a 3.6 m optical and infrared telescope that is host to 12 instruments and has been operating since 1979 by the National Research Council of Canada, Centre National de la Recherche Scientifique of France and the University of Hawaii.

ESPaDOnS

The Echelle SpectroPolarimetric Device for the Observation of Stars (ESPaDOnS) is mounted at the CFHT near the summit of Mauna Kea in Hawaii (Donati et al., 2006). This instrument can detect the complete optical spectrum ($0.3-1.05\,\mu$m) with a spectral resolution of either $R \sim 68{,}000$ ('object + sky' mode, as used in Chap. 4) or $R \sim 81{,}000$ ('object only' mode). It has a 79 gr/mm grating that spans 40 grating orders and a 2000×4500 CCD (charge-coupled device) detector. The spectral sampling bin size of ESPaDOnS is 1.8 km s^{-1}. The high resolution acheived with ESPaDOnS allows in-depth emission and absorption line profile analysis to be carried out. Incorporating the circular and linear polarisation spectra, this instrument is excellent for measuring the magnetic fields in a target (e.g. Donati et al., 2006). It can also be used solely as a spectrograph as in Chap. 4 where the high resolution is taken advantage of to calculate the veiling in the CTTS RU Lup by precisely measuring photospheric lines.

Figure 2.6: Left panel: An aerial view of the CTIO site on Cerro Tololo, with the 4 m Víctor M. Blanco Telescope in the foreground (*Credit:* CTIO/NOIRLab/NSF/AURA/P. Marenfeld). **Right panel:** The ANDICAM detector mounted on the 1.3 m telescope at the CTIO site (*Credit:* SMARTS consortium).

2.2.3 CTIO/SMARTS

The Cerro Tololo Inter-American Observatory (CTIO) is located on the mountain of Cerro Tololo in the Coquimbo region of Chile. The two largest telescopes include the 4 m Víctor M. Blanco Telescope and the 4.1 m Southern Astrophysical Research (SOAR) telescope, which is located just to the southeast on Cerro Pachón. Additionally, there are four smaller (0.9 m, 1.0 m, 1.3 m and 1.5 m) telescopes operated by the Small & Moderate Aperture Research Telescope System (SMARTS) consortium which includes collaborations from CTIO, Yale University and Ohio State University.

ANDICAM

A Novel Dual Imaging CAMera (ANDICAM) is a 1.3 m telescope at the CTIO site. It can obtain B, V, R, I, J, H and K photometry within a 6 arcmin (optical) or 2.4 arcmin (NIR) field of view. This telescope's CCD is a Fairchild 447 2048 $\times$ 2048 with a pixel scale of $0.371''$/pixel (DePoy et al., 2003). The optical filters B, V, R and I are KPNO Johnson-Kron-Cousins filters and are used in Chap. 4 to observe the young star RU Lup.

2.3 Emission lines as diagnostic tools in the optical and NIR

The circumstellar environment of YSOs is best analysed through spectroscopic observations. Depending on the class of the YSO, it may be necessary to probe the inner, dusty workings of the protostar at longer wavelengths (i.e. the IR). Pre-main sequence stars, however, are less enveloped and are routinely studied at optical wavelengths. Both of these wavelength ranges are utilised in this thesis, measuring and analysing key emission lines in the spectra to characterise these young objects.

2.3.1 Equivalent width

A relative measure of the line strength of an emission or absorption feature with respect to the continuum level is the equivalent width (EW). This relative quantity does not require a flux calibration of the spectrum and is also sometimes denoted as W_λ:

$$W_\lambda = \int \frac{I_0 - I(\lambda)}{I_0}\, d\lambda \ , \tag{2.3}$$

where λ is the centroid wavelength of the line being measured, I_0 is the intensity of the continuum at the line centre and $I(\lambda)$ is the observed intensity of the line (Schulz, 2005, and references therein). The value quantifying a spectral line's energy as an area is how it is related to both the abundance of the ion and the strength of the associated transition. EW is used throughout this thesis to compare line strengths between different epochs and studies, conscious of the caveats above regarding continuum variations.

2.3.2 Extinction

Extinction (A_λ) is a measure of how much radiation at a specific wavelength (λ) has been absorbed due to dust in the intervening space between the emitting source and the observer. Measuring the amount of extinction is vital to calculating the actual luminosity of any deeply embedded object. Out of convention, the visual extinction (A_V) is generally referenced. Extinction affects shorter wavelengths more than longer wavelengths, which has the effect of reddening spectra and decreasing the amount of flux observed (Nisini, 2008). This is due to the size of the dust grains absorbing the radiation: the longer the wavelength, the larger the grains would need to be to absorb it. At appropriately long wavelengths, less interaction between the radiation and the dust grains occurs, allowing the emission to reach our telescopes un-extincted. We can

study the extinction in outflows by obtaining actual, versus theoretical, emission line ratios of forbidden emission lines from Iron ([Fe II]) . Extinction is not the same in all regions of a YSO structure, which means that if the spatial resolution is high enough, it is important to note that an A_V measurement take on source will be higher than one taken further out in the jet where things are less dense. The [Fe II] lines discussed below originate in environments such as jets, therefore, it can be assumed that the extinction measured with this method will be a lower limit for the extinction present close-in to the YSO.

[Fe II] transitions can be used to determine A_V, however, uncertainties are still prevalent in estimating the radiative transition probabilities used in the calculation. To do this, there are two pairs of bright near-IR lines (1.644/1.257 μm and 1.644/1.320 μm) whose ratios are useful because they originate from the same upper level and are optically thin (Nisini et al., 2002). Here, the theoretical intensity ratio depends not on the physical conditions in the emission region, but the frequencies and transition probabilities. The Einstein coefficients represent the transition rates and are as described in the previous section, however, here I use a notation where they are identified by the wavelength of the line they represent as opposed to the level numbers: $\mathrm{A}_{ij} = \mathrm{A}_{\lambda_1}$ and $\mathrm{A}_{ik} = \mathrm{A}_{\lambda_2}$. The observed ratio is described in the following equation (Gredel & Roland, 1994):

$$\frac{I_{\lambda_1}}{I_{\lambda_2}} = \frac{\mathrm{A}_{\lambda_1}\,\lambda_2}{\mathrm{A}_{\lambda_2}\,\lambda_1} 10^{-E(\lambda_1-\lambda_2)/2.5}, \tag{2.4}$$

where I_{λ_1} and I_{λ_2} are the observed intensities of the two [Fe II] lines, $\mathrm{A}_{\lambda_1} = 4.65$ and $\mathrm{A}_{\lambda_2} = 4.83$ (taken from Nussbaumer & Storey, 1988), λ_1 and λ_2 are the wavelengths of the lines, and $E(\lambda_1 - \lambda_2)$ is the colour excess at the wavelength of the considered lines:

$$E(\lambda_1 - \lambda_2) = \alpha\,(\lambda_1^{\beta} - \lambda_2^{\beta})\,A_V. \tag{2.5}$$

This equation, along with an extinction law (e.g. Rieke & Lebofsky, 1985), allows for the calculation of A_V:

$$\begin{aligned} &A_\lambda = \alpha\,\lambda^{\beta} A_V; \\ &\alpha = 0.42,\ \beta = -1.75. \end{aligned} \tag{2.6}$$

As described in more detail in Nisini et al. (2005), while both 1.644/1.257 μm and 1.644/1.320 μm are valid ratios to use to find A_V, the 1.644/1.257 μm ratio tends to provide a slightly larger value of A_V. Nisini et al. (2005) determines that this is not due to any observational uncertainties, but is most likely due to the uncertainties in

the radiative transition probabilities of the lines. Undertaking the calculations of these probabilities, Quinet et al. (1996) found values with discrepancies from the the previous Nussbaumer & Storey (1988) ones as large as 20%.

2.3.3 [Fe II] line ratios as a diagnostic of density

The NIR [Fe II] lines that can be useful in jet diagnostics originate from transitions within the first 16 fine structure levels. Depending on their excitation temperatures and critical densities, [Fe II] line ratios can be used to determine different important characteristics of jets (e.g. Nisini et al., 2002, and references therein). Ratios such as 1.533/1.644 μm, 1.599/1.644 μm, and 1.677/1.644 μm have relatively large, different critical densities (between 10^4 and $10^5\,\mathrm{cm}^{-3}$) and can be used to diagnose the electron density. However, as they have very similar excitation temperatures (ranging from ~11,000 K to ~12,000 K) their ratio is not very sensitive to the gas temperature. In order to ascertain the gas temperature it would be necessary to consider [Fe II] transitions with higher excitation energies (e.g. ~19,000 K) such as the 1.811 μm and 1.813 μm lines, however, these particular lines fall in regions of poor atmospheric transmission. Alternatively, the bright optical [Fe II] line at 0.862 μm could be used (Nisini, 2008).

2.3.4 Permitted emission lines

Many of the transitions observed from these YSOs are from electronic states of Hydrogen and Hydrogen-like configurations of elements also with a single electron in an outer s-shell (Hartigan, 2008). At bluer wavelengths the Hydrogen Balmer continuum dominates in accreting TTSs, which is produced by photons released through capture of free electrons into the $n = 2$ level of Hydrogen (Stahler & Palla, 2004). The blue regions of the DR Tau and BP Tau spectra in Fig. 2.7 demonstrate this strong Balmer continuum. However, WTTSs demonstrate a behaviour more akin to main-sequence objects where the flux is observed to be lower in this region (see Fig. 2.7). The notable presence of this Hydrogen emission provides a distinguishing spectroscopic feature between CTTSs and WTTSs, specifically with the equivalent width of the Hα 6563 Å emission line. Traditionally, the threshold between CTTSs and WTTSs has been defined as $\mathrm{EW}_{\mathrm{H}\,\alpha} < 5$ Å (Herbig & Bell, 1988) and $\mathrm{EW}_{\mathrm{H}\alpha} < 10$ Å (Appenzeller & Mundt, 1989). The actual cut-off is therefore somewhat arbitrary and, in any event, depends on spectral type as well as spectral resolution of the observations (Martín, 1997).

These Hydrogen transitions (H I) occur in the accretion funnels of YSOs where the material from the surrounding disk is being accreted onto the stellar surface (see

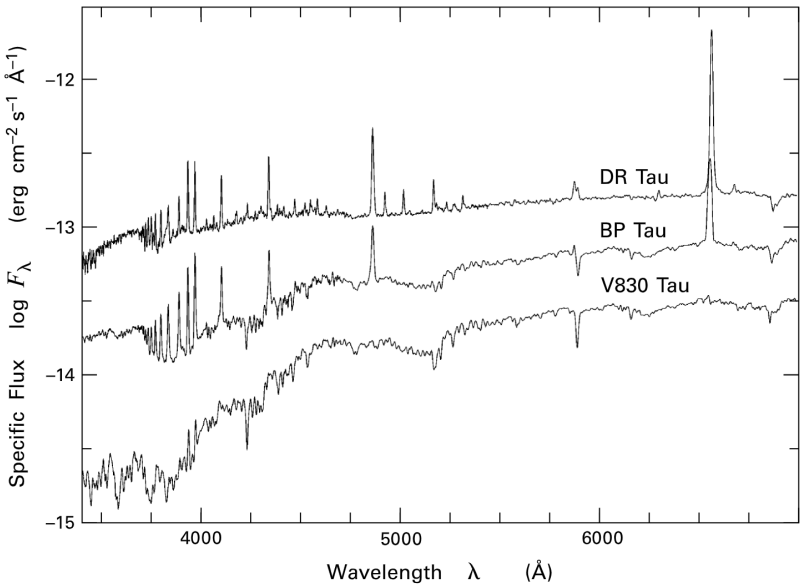

Figure 2.7: Spectra of three T Tauri stars demonstrating the difference in Balmer continuum emission at blue wavelengths between CTTSs (DR Tau and BP Tau) and WTTSs (V830 Tau). The flux is arbitrary as the spectra are shifted vertically to be easier to visually compare. (Taken from Stahler & Palla, 2004)

Section 1.2.1) (e.g. Calvet & Hartmann, 1992; Hartmann et al., 1994; Muzerolle et al., 2001). The brightest of these Balmer lines is the Hα 6563 Å emission line, which can have an equivalent width, in some cases, as high as -150 Å in strongly accreting stars (the negative value here indicates the line is in emission as opposed to a positive value for an absorption line) (Muzerolle et al., 2003).

3

Investigating episodic accretion in a very low-mass young stellar object

Camille Stock, Alessio Caratti O Garatti, Pauline McGinnis, Rebeca García López, Simone Antoniucci, Rubén Fedriani & Tom P. Ray, (2020), Astronomy & Astrophysics, 643, 181, https://doi.org/10.1051/0004-6361/202038897.

3.1 Introduction

The young stellar object (YSO) phase represents a very important stage in the life of a star and influences its subsequent evolution. YSOs can be divided into four classes (Class 0, I, II and III), where Class I to Class III are defined by their spectral index (α) measured from the near- to mid-infrared (NIR to MIR) portion of the spectrum (Lada, 1987). Class 0 stars are normally observed only at millimetre (mm) and radio wavelengths and represent the earliest phase when over 50% of the mass is still contained in an envelope surrounding the protostellar core. Although Class I YSOs are deeply embedded, they are nevertheless observable in the NIR. Since they are still strongly accreting and generating powerful outflows, it is possible to study both accretion and ejection processes at this relatively early stage through IR spectroscopy and imaging using state-of-the-art ground-based telescopes.

Young stars have been known to exhibit episodic variability in their accretion and ejection over the course of their evolution (see e.g. Audard et al., 2014, and references therein). It is important to note that in this case, an increase in accretion is usually associated with an increase in luminosity as more material is accreted, producing strong shocks onto the stellar photosphere and additional radiation. Two evident forms that this variability mentioned in Chap. 1 can take are FUor-type outburts (Section 1.4.1 and EXor outbursts (Section 1.4.2).

EXor bursts are phenomena that occur over shorter timescales ($\sim 1-2$ years) and are less violent ($\dot{M}_{\rm acc}$ increases of $1-2$ orders of magnitude typically up to $10^{-7}-10^{-6}\,M_{\odot}\,{\rm yr}^{-1}$) than their FUor counterparts (Audard et al., 2014). Their frequency is also higher than FUors, with bursts occurring potentially only a few years apart (Herbig, 2008). Similar to FUors in the quiescent state, most EXors are optically observable classical T Tauri stars. However, there is evidence that earlier stage protostars also exhibit episodic bursts (see, e.g. Audard et al., 2014, and references therein), and it has been found that, in Class I YSOs, this eruptive variability is at least an order of magnitude more common than in Class II YSOs (Contreras Peña et al., 2017). Certainly

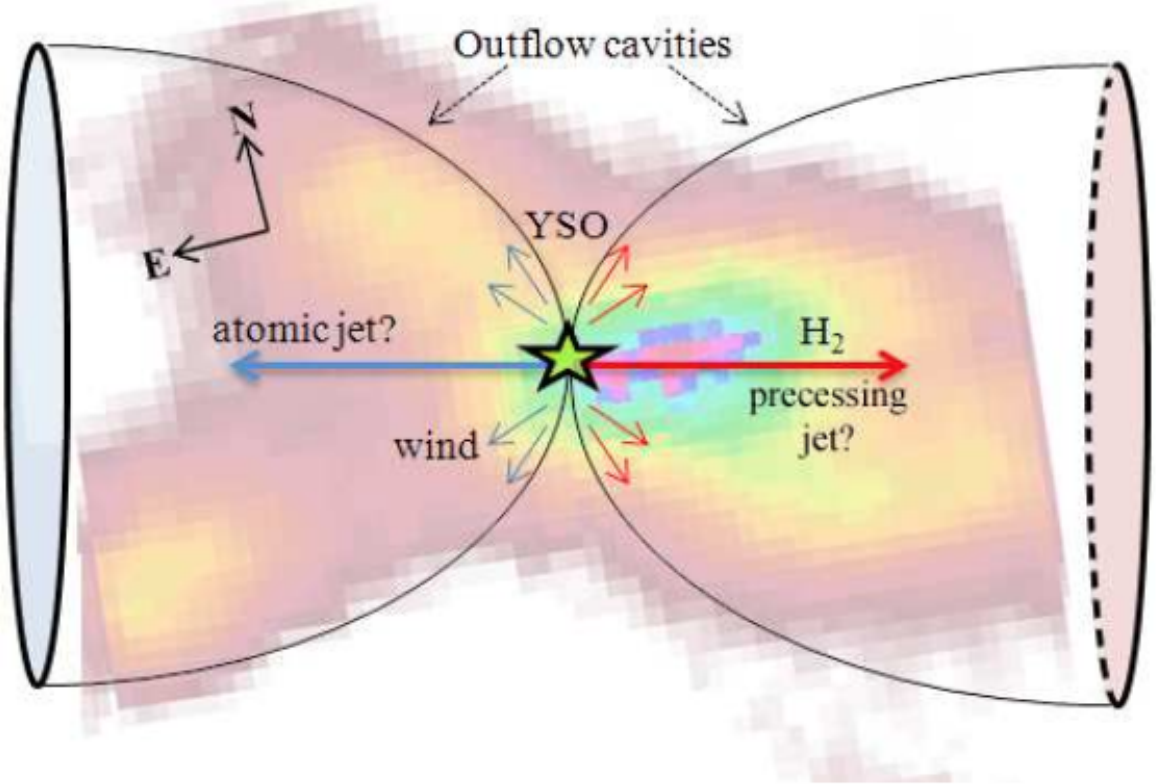

Figure 3.1: A morphology sketch of IRS54's outflow structure overlaid with an image acquired with SINFONI in the K-band in 2010 (García-López et al., 2013).

the increased use of IR observations has helped to shed light on this phenomenon at earlier phases in stellar evolution.

Here, the variability of a single object (IRS 54) is investigated over 9 years using NIR spectroscopic and photometric data. IRS 54 (YLW 52) is located in the Ophiuchus star-forming region at a distance of $\sim$ 137 pc (Sullivan et al., 2019). It is a Class I very low-mass star (VLMS) ($M_\star \sim 0.1 - 0.2\,\mathrm{M}_\odot$) of estimated spectral type M (García-López et al., 2013, hereafter GL13) with a bolometric luminosity of $L_{\mathrm{bol}} = 0.78\,\mathrm{L}_\odot$ (van Kempen et al., 2009). Observations of this YSO have revealed an accretion disk and a H_2 molecular jet (Khanzadyan et al., 2004, GL13) typical of protostars at an early evolutionary phase (see e.g. Lee, 2020, and references therein), see Fig. 3.1. IRS 54 in fact is one of the lowest luminosity sources where an H_2 outflow has been spatially resolved (GL13). Moreover, it is an ideal candidate for studying variability due to its edge-on disk geometry that allows the red- and blue-shifted components of its outflow to be viewed, and because multi-epoch spectra and imaging are available spanning almost a decade.

Date yyyy-mm-dd	Telescope	Int (s)	Seeing (″)	R	Std. star (Hip)	Band	Method
2005-06-16	VLT/ISAAC	300	1.54	10500	082254	J	spec.
2005-06-16	VLT/ISAAC	300	1.54	10000	082254	H	spec.
2005-06-16	VLT/ISAAC	180	1.54	8900	082254	Ks	spec.
2013-04-22	VLT/ISAAC	300	1.69	10000	082254	H	spec.
2013-06-12	VLT/ISAAC	20	1.00	-	-	H	photo.
2013-06-12	VLT/ISAAC	20	1.00	-	-	J	photo.
2013-08-01	VLT/ISAAC	300	1.12	10500	082254	J	spec.
2013-09-10	VLT/ISAAC	300	1.38	8900	092393	Ks	spec.
2013-09-12	VLT/ISAAC	60	0.49	-	-	Ks	photo.
2014-05-22	VLT/SINFONI	300	0.56	4000	082430	H	IFU
2014-06-02	VLT/SINFONI	300	0.60	4000	079771	K	IFU

Table 3.1: Observation log for ISAAC and SINFONI data taken in 2005, 2013 and 2014. The SINFONI archival data used from 2010 is not included in this table, being published in GL13. J band photometry was implemented using the acquisition image taken in the J band the same night as the spectroscopy J band data.

3.2 Observations and data reduction

The Class I protostar IRS 54 was observed over four epochs (2005, 2010, 2013 and 2014) in the NIR, as reported in Table 3.1. Epochs 2005 and 2013 were obtained with VLT/ISAAC (Moorwood et al., 1998). The details of the ISAAC instrument can be found in Section 2.2 and Table 3.1. The K band data in 2005 cover a larger wavelength range than in 2010, because two contiguous spectral segments were acquired in 2005. To correct for the atmospheric response, telluric standard stars were also observed (see Column 6 in Table 3.1).

During the 2013 epoch, ISAAC was at the end of its life and the top two quadrants of the resultant images were compromised, visible in Fig. 3.2. This was known when the observations were taken, therefore the object was positioned in the bottom half of the field-of-view. However, this restricted the region of useful data. This only effected the photometry data in that there were fewer nearby stars that could be used to calibrate the shift and flux of IRS54. ISAAC spectroscopic data were reduced in the standard way using IRAF[1] (Image Reduction and Analysis Facility). The wavelength calibration was carried out utilizing the NIR OH ro-vibrational atmospheric lines in each frame, using IRAF routines. These lines occur at known wavelengths, therefore it is possible

[1]IRAF is distributed by the National Optical Astronomy Observatory (NOAO). http://iraf.noao.edu

to identify them in the science spectra with a line list[1] and fit a polynomial function to wavelength versus pixel offset. Spatial distortion and curvature caused by the long slit were corrected using the calibration file STARTRACE. An average wavelength accuracy of ~ 2 Å was achieved. Telluric standard stars were observed under similar airmass conditions and used to remove the unwanted telluric lines from the target spectra. This un-flux calibrated telluric spectrum was divided by the spectrum of a blackbody of the same spectral type[2]. Hydrogen recombination lines were manually removed from the spectrum of the telluric standard star so that they would not appear in the target spectrum and subsequently blend with the Hydrogen recombination lines being emitted from the target. This spectrum was then used as an input in the 'telluric' routine of IRAF which divides the target spectrum by this telluric spectrum and is multiplied by an appropriate scaling factor to get the telluric-removed science spectrum of the target.

The photometric data obtained with ISAAC (epochs 2005 and 2013) were reduced with IRAF. Flat-fielding of the raw data, sky subtraction and cosmic ray corrections were all performed. Approximately five nearby stars in the field of view were used to flux calibrate the final science images using their known 2MASS catalogue values. However, the J band flux calibration was completed using the J band acquisition image as photometric science images were not available. The infrared filters of ISAAC were $J \sim 1.25\,\mu$m, $H \sim 1.65\,\mu$m, and $Ks \sim 2.16\,\mu$m, and the filters of 2MASS were $J \sim 1.235\,\mu$m, $H \sim 1.662\,\mu$m, and $Ks \sim 2.159\,\mu$m. When calculating the line velocities, the spectra were corrected to the parent cloud velocity of $\sim 3.5\,\mathrm{km\,s^{-1}}$ (Wouterloot et al., 2005; André et al., 2007).

The 2014 data were acquired over two separate nights with the VLT/SINFONI (Eisenhauer et al., 2003), utilizing a field of view of $3'' \times 3''$ and a pixel scale of $0.1''$. Further specifications of the SINFONI instrument can be found in Section 2.2 as well as in Table 3.1. As with the ISAAC data, to correct for atmospheric effects, telluric standard B-type stars were observed (see Column 6 of Table 3.1).

The data reduction was completed with the GASGANO[3] data file organiser to run the standard SINFONI pipeline recipes. These were used to apply dark and bad pixel masks, flat field correction, optical depth correction and a wavelength calibration using either OH lines (in the case of the H band) or arc lamps (in the case of the K band, where there were not enough strong OH lines) to the data cubes. A systematic wavelength shift of ~ 2.2 Å was found (and corrected for) with respect to the theoretical wavelength

[1] I used the atlas of OH lines from Rousselot et al. (2000) found in a condensed form at the ESO site: https://www.eso.org/sci/facilities/paranal/decommissioned/isaac/tools.

[2] These blackbody spectra were obtained from the ESO site: https://www.eso.org/sci/facilities/paranal/decommissioned/isaac/tools/lib

[3] GASGANO is maintained by ESO. https://www.eso.org/sci/software/gasgano

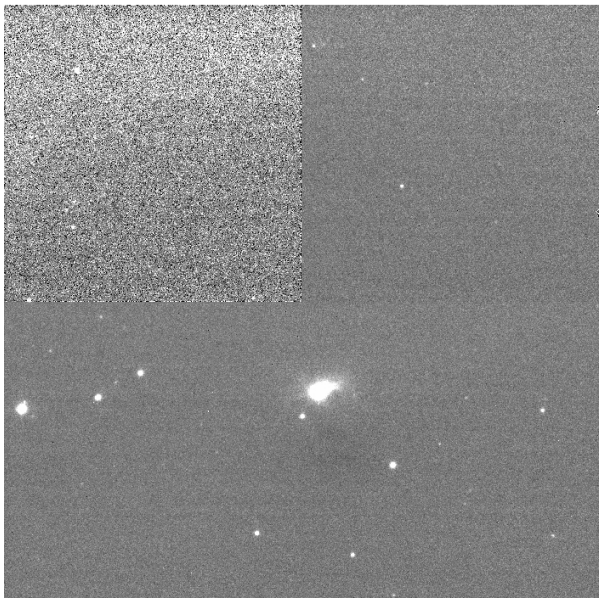

Figure 3.2: One of the science images taken in the K-band of IRS54 with ISAAC. Notice the top two quadrants of the detector are compromised and the object has been positioned in the bottom half where the only usable data is.

values. A spectrum was then extracted from the telluric cube on source using IRAF. The region to extract (about the central region on the cube) was determined using CASA[1] (Common Astronomy Software Applications) Viewer. The telluric lines were removed in the same method as described above for the ISAAC data. The H band reduction of the 22 May 2014 SINFONI data required a further manual sky subtraction because OH line residuals were present in the datacube. This was done by selecting a region of sky in the field of view with little to no emission from the source and subtracting this from the science cube. The resulting spectra were extracted on source. The extraction region on source was centered at $[0'', 0'']$ and the sky region was centered at $[-1.3'', -1.3'']$, both with apertures of about 3×3 pixels. The 2010 VLT/SINFONI archival data were taken from GL13.

[1]CASA is developed by an international consortium of scientists based at the National Radio Astronomical Observatory (NRAO), the European Southern Observatory (ESO), the National Astronomical Observatory of Japan (NAOJ), the Academia Sinica Institute of Astronomy and Astrophysics (ASIAA), the CSIRO division for Astronomy and Space Science (CASS) and the Netherlands Institute for Radio Astronomy (ASTRON) under the guidance of NRAO. https://casa.nrao.edu

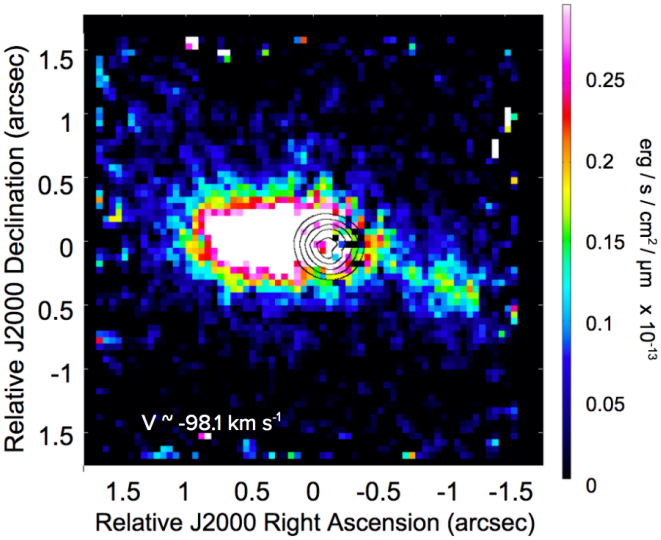

(a) blue-shifted [Fe II] (1.644 μm) emission.

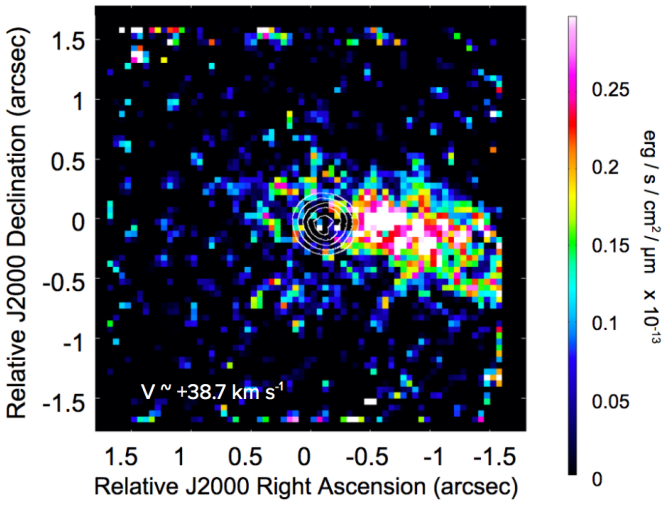

(b) red-shifted [Fe II] (1.644 μm) emission.

Figure 3.3: **(a)** blue-shifted component of the [Fe II] emission in the *H* band in IRS 54 from the SINFONI 2014 data. Four spectral channels were averaged from 1.6430 μm (-171 km s^{-1}) to 1.6438 μm (-25 km s^{-1}). **(b)** red-shifted component of the [Fe II] emission in the *H* band in IRS 54 from the SINFONI 2014 data. Four spectral channels were averaged from 1.6440 μm (11 km s^{-1}) to 1.6443 μm (66 km s^{-1}). For reference, the centre black (**a**) and white (**b**) contours represent the continuum of the source taken at levels of 0.1, 0.3, 0.5, 0.7 and 0.9. One pixel here corresponds to 0.1″.

3.3 Results

3.3.1 Morphology

Detected features in IRS 54 include a disk, jet, and illuminated outflow cavity walls (see Figure B.2 of GL13). The geometry of the system is such that the disk is seen roughly edge-on (GL13). This geometry poses challenges from an observational perspective, specifically in viewing the inner disk where most of the accretion activity takes place. Nevertheless, the edge-on disk configuration of IRS 54 also provides good conditions in which to trace its bipolar jet back to the source (see below).

Images were generated from the SINFONI data for the H_2 and [Fe II] (1.644 μm) emission lines in the *H* and *K* bands. Figure 3.3 shows both the blue- and red-shifted continuum-subtracted images of the emission from the [Fe II] line at 1.644 μm observed in 2014, where four spectral channels were averaged from 1.6430 μm (-171 km s^{-1}) to 1.6438 μm (-25 km s^{-1}, see Fig. 3.3a) and from 1.6440 μm (11 km s^{-1}) to 1.6443 μm (66 km s^{-1}, see Fig. 3.3b). This emission traces the jet of the YSO and is extended with respect to the source position, which is indicated with the black and white contours in

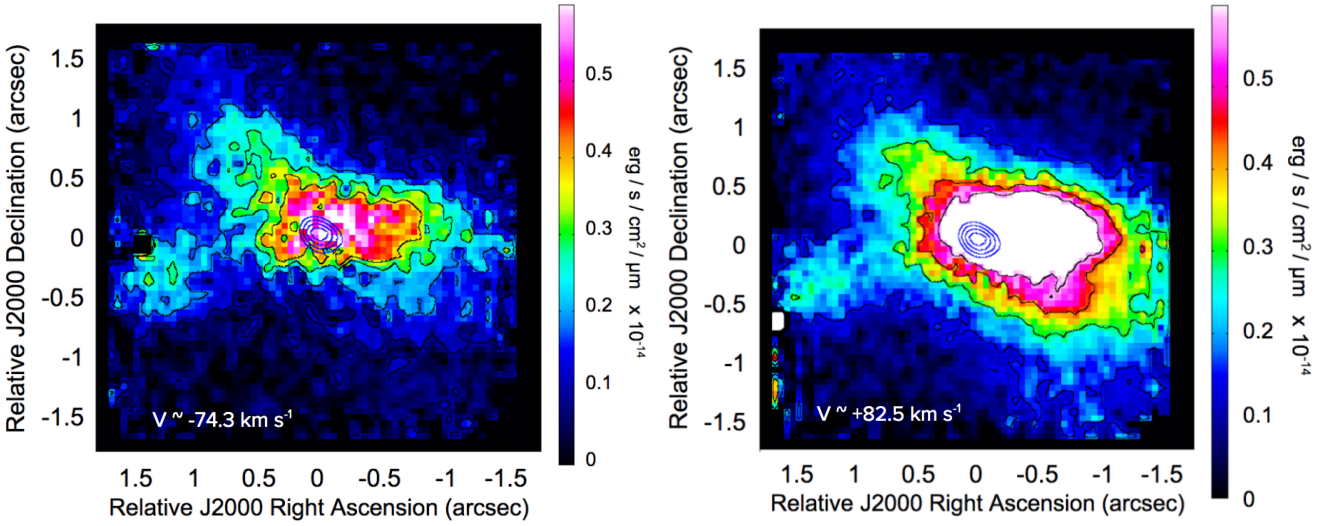

(a) blue-shifted H_2 (2.1218 μm) emission.

(b) red-shifted H_2 (2.1218 μm) emission.

Figure 3.4: (a) blue-shifted component of the H_2 emission in the K band in IRS 54 from the SINFONI 2014 data. Four spectral channels were averaged from 2.12087 μm (-125 km s^{-1}) to 2.12160 μm (-22 km s^{-1}). **(b)** red-shifted component of the H_2 emission in the K band in IRS 54 from the SINFONI 2014 data. Four spectral channels were averaged from 2.12185 μm (30 km s^{-1}) to 2.12258 μm (134 km s^{-1}). For reference, the centre blue contours represent the position of the continuum of the source taken at levels of 0.2, 0.4, 0.6 and 0.8 of the continuum flux. One pixel here corresponds to 0.1″.

Fig. 3.3a and Fig. 3.3b, respectively. It is spatially asymmetric about the central source, with much stronger blue-shifted than red-shifted emission. In summary, the IRS 54 jet predominately emits [Fe II] in the blue-shifted lobe.

In contrast, most of the H_2 emission comes from the red-shifted lobe: it traces not only the bright red-shifted jet but also what appear to be cavity walls that straddle the source. Figure 3.4 shows the red- and blue-shifted continuum-subtracted images of IRS 54 at the H_2 1-0 S(1) emission line in the K band. In Fig. 3.4a four spectral channels were averaged from 2.12087 μm (-125 km s^{-1}) to 2.12160 μm (-22 km s^{-1}), and in Fig. 3.4b four spectral channels were averaged from 2.12185 μm (30 km s^{-1}) to 2.12258 μm (134 km s^{-1}). The blue contours represent the location of the central source and its continuum emission. The behaviour of this H_2 emission traces a different spatial component of the jet than that of the [Fe II] emission. The red-shifted component of the jet is primarily radiating H_2 at 2.122 μm. The molecular jet was already observed to be asymmetric by GL13, with a red-shifted molecular jet component and also possibly a blue-shifted atomic jet component. Here, this asymmetry is observed as well and also observe the atomic component. These observations therefore adhere to the morphology sketch presented by GL13 (their Figure B.2).

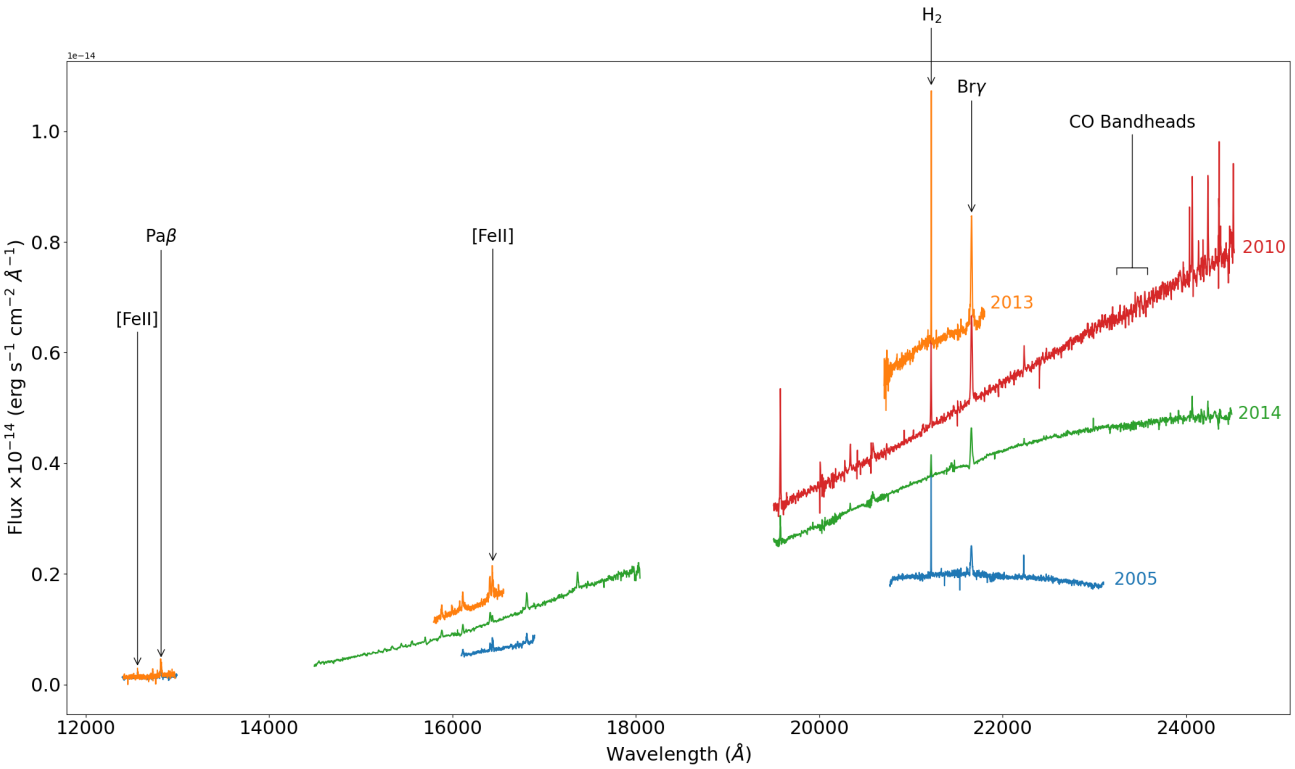

Figure 3.5: Spectral Energy Distribution (SED) of J, H and K bands over the four epochs (2005, 2010, 2013 and 2014). Notably, the J band has two overlapping spectra from 2005 (blue) and 2013 (orange).

3.3.2 Spectroscopy and IFU on source

Figure 3.5 shows the on-source flux calibrated spectra (J, H and K bands) along with the main lines detected from these observations (epochs 2005, 2013 and 2014) and from 2010 archival data (GL13). It is apparent from Fig. 3.5 that not only the flux intensities of both line and continuum have changed from one epoch to another, but also the shape of each spectral energy distribution (SED). Between 2005 (blue), 2010 (red) and 2013 (orange) the flux increased and the shape of the SED went from being approximately flat (especially in the K band) to having a much steeper slope. The SED of 2014 (green) receded to a flux below that of 2010 (red), becoming less steep in the K band. Because 2010 data were only available in the K band, it is impossible to say definitively whether this was the case in the J and H bands as well. Emission lines at different epochs have been identified and labelled in Fig. 3.5; Tables 3.2 and 3.3 provide a list of the main lines detected along with their full width at half maximum (FWHM), fluxes, radial velocities and full width at zero intensity (FWZI). These quantities are analysed further in the coming sections to derive visual extinction (A_V) and mass accretion rates at different epochs.

2005	Line	λ (μm)	FWHM (Å)	F (erg s^{-1} cm^{-2})	v_R (km s^{-1})	FWZI ($\pm$24 km s^{-1})
J	[**Fe**II] (HVC, b)	1.257	3.4	$(3.4 \pm 0.4) \times 10^{-16}$	-111 ± 5	-
	[**Fe**II] (LVC)	1.257	2.7	$(1.7 \pm 0.3) \times 10^{-16}$	-30 ± 5	358
	[**Fe**II] (HVC, r)	1.257	5.2	$(2.6 \pm 0.6) \times 10^{-16}$	54 ± 5	-
	Paβ	1.282	13.0	$(2.8 \pm 0.2) \times 10^{-15}$	-17 ± 4	608
H	**Br**13	1.611	12.9	$(1.4 \pm 0.9) \times 10^{-15}$	0 ± 5	540
	Br12	1.641	12.5	$(1.6 \pm 0.1) \times 10^{-15}$	1 ± 4	530
	[**Fe**II] (HVC, b)	1.644	3.6	$(7.0 \pm 0.4) \times 10^{-16}$	-121 ± 3	-
	[**Fe**II] (LVC)	1.644	5.9	$(9.8 \pm 0.7) \times 10^{-16}$	-43 ± 3	511
	[**Fe**II] (HVC, r)	1.644	7.3	$(7.7 \pm 0.8) \times 10^{-16}$	64 ± 3	-
	Br11	1.681	14.7	$(2.7 \pm 0.2) \times 10^{-15}$	-22 ± 4	535
K	**H**$_2$	2.122	3.1	$(7.2 \pm 0.8) \times 10^{-15}$	11 ± 1	184
	Brγ	2.166	19.2	$(1.0 \pm 0.6) \times 10^{-14}$	-113 ± 2	733
2010						
K	**H**$_2$	2.122	7.0	$(1.2 \pm 0.2) \times 10^{-14}$	6 ± 3	339
	Brγ	2.166	18.3	$(3.0 \pm 0.7) \times 10^{-14}$	-18 ± 4	734
2013						
J	[**Fe**II] (HVC, b)	1.257	2.4	$(4.2 \pm 0.3) \times 10^{-16}$	-102 ± 5	-
	[**Fe**II] (LVC)	1.257	1.6	$(1.8 \pm 0.2) \times 10^{-16}$	-22 ± 5	358
	[**Fe**II] (HVC, r)	1.257	5.1	$(1.1 \pm 0.2) \times 10^{-16}$	107 ± 5	-
	Paβ	1.282	14.8	$(3.5 \pm 0.2) \times 10^{-15}$	-7 ± 4	608
H	**Br**14	1.588	14.6	$(3.5 \pm 0.4) \times 10^{-15}$	-32 ± 4	717
	Br13	1.611	13.6	$(4.2 \pm 0.3) \times 10^{-15}$	-5 ± 3	632
	Br12	1.641	13.9	$(5.2 \pm 0.4) \times 10^{-15}$	-34 ± 5	566
	[**Fe**II] (HVC, b)	1.644	4.8	$(3.4 \pm 0.2) \times 10^{-15}$	-98 ± 2	-
	[**Fe**II] (LVC)	1.644	2.3	$(2.3 \pm 0.2) \times 10^{-15}$	-17 ± 2	565
	[**Fe**II] (HVC, r)	1.644	7.0	$(3.4 \pm 0.2) \times 10^{-15}$	72 ± 5	-
K	**H**$_2$	2.122	3.2	$(5.3 \pm 0.2) \times 10^{-15}$	7 ± 2	170
	Brγ	2.166	16.4	$(4.2 \pm 0.9) \times 10^{-14}$	-57 ± 1	803

Table 3.2: J, H and K bands Kinematics for IRS 54 taken with VLT/ISAAC (2005 and 2013) and VLT/SINFONI (2010) The letters b and r in column three represent whether the component is blue- or red-shifted.

2014	Line	λ (μm)	FWHM (Å)	F (erg s^{-1} cm^{-2})	v_R (km s^{-1})	FWZI ($\pm$24 km s^{-1})
H	**Br**20	1.519	13.9	$(6.8 \pm 0.7) \times 10^{-16}$	27 ± 3	572
	Br19	1.526	22.9	$(1.2 \pm 0.1) \times 10^{-15}$	-24 ± 5	707
	Br18	1.534	22.4	$(1.4 \pm 0.3) \times 10^{-15}$	-37 ± 7	664
	Br17	1.544	16.0	$(1.1 \pm 0.2) \times 10^{-15}$	8 ± 5	660
	Br16	1.556	17.3	$(1.5 \pm 0.1) \times 10^{-15}$	-31 ± 3	578
	Br14	1.588	14.7	$(2.0 \pm 0.2) \times 10^{-15}$	-11 ± 3	623
	Br13	1.611	14.9	$(2.8 \pm 0.1) \times 10^{-15}$	12 ± 3	614
	Br12	1.641	13.9	$(2.9 \pm 0.2) \times 10^{-15}$	13 ± 3	585
	[**Fe**II]	1.644	10.4	$(1.3 \pm 0.1) \times 10^{-15}$	-65 ± 3	419
	Br11	1.681	17.1	$(5.8 \pm 0.3) \times 10^{-15}$	1 ± 3	945
	Br10	1.736	17.1	$(5.4 \pm 0.4) \times 10^{-15}$	-28 ± 3	673
K	**H**$_2$	2.122	3.1	$(7.2 \pm 0.8) \times 10^{-15}$	11 ± 3	367
	Brγ	2.166	19.2	$(1.0 \pm 0.6) \times 10^{-14}$	-33 ± 4	789

Table 3.3: A table continued from Table 3.2 of J, H and K bands Kinematics for IRS 54 taken with VLT/SINFONI in 2014.

The spectra from IRS 54 display multiple hydrogen-recombination lines, the brightest of which are the Brγ and Paβ emission lines in the K and J band, respectively. These lines are primarily accretion signatures (e.g. Muzerolle et al., 1998). Forbidden iron ([Fe II] 1.257 μm and 1.644 μm) and molecular hydrogen (H_2 2.122 μm) emission lines, which trace the jet, are also visible. The [Fe II] emission is also useful in understanding physical properties of the surroundings of the YSO, such as the amount of foreground extinction in the observations.

The R(0-15) and P(1-9) (between 2.31 and 2.37 μm) rotational lines (J) of the v= 2 − 0 CO band head, which trace relatively mild temperatures (a few hundred Kelvin) are also worth investigating in the K-band spectra that extend to these wavelengths (2010 and 2014). These lines are possibly seen in absorption in the 2014 data (see Fig. 3.6). The signal-to-noise ratio is higher in the 2014 spectrum, making these absorption features easier to identify in this epoch than in the 2010 epoch, however, many of these line measurements are below 3σ. Notably, a star of spectral type M would have CO photospheric absorption lines, including the high rotational lines (i.e. those that actually pile up, producing the band heads), which typically trace gas at a few thousand Kelvin. The high-J lines are not seen here. Moreover, such a young source as IRS 54 should present very high veiling and thus photospheric lines should not be detected. Therefore if these features in absorption do exist in the spectrum, they

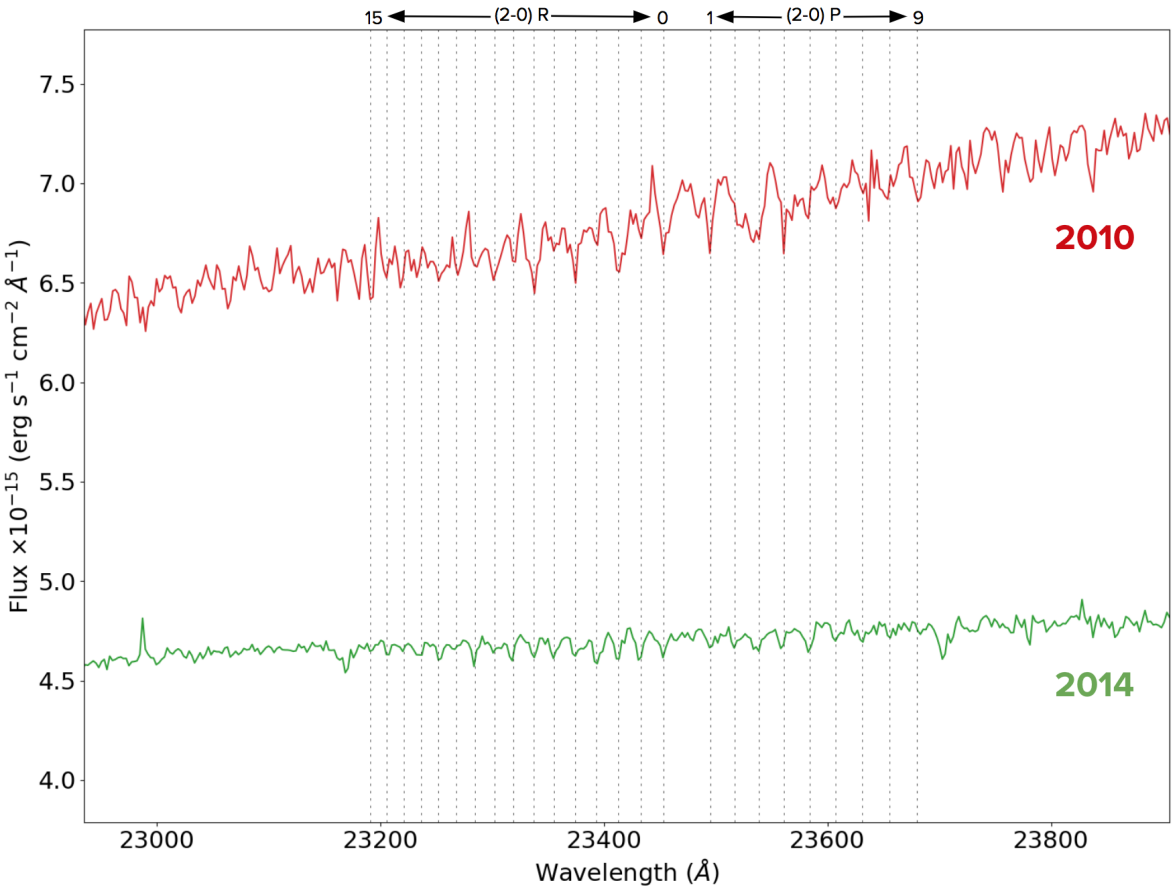

Figure 3.6: Where the low J lines from the v= 2 – 0 CO band head (2.31 - 2.37 μm) in the 2010 (red) and 2014 (green) data would be. There is some evidence that they are seen in absorption. The vertical lines indicate the locations of the different lines.

most likely originate from the outer disk or from the envelope, seen against a much hotter inner disk gas. These features are observed in emission during outbursts of EXors (Audard et al., 2014).

3.3.3 Variability in visual extinction

As discussed in Section 2.3.2, the ratio of [Fe II] 1.644/1.257 μm emission lines can be used as a diagnostic of visual extinction present. The 1.320 μm is also an option, however it is outside this study's wavelength range and therefore is not used. To study if and how the visual extinction changes with time, line ratios were measured at different epochs. A_V was calculated for the ISAAC data (2005 and 2013 epochs) using Equation 2.4 for this line ratio from the spectra extracted on-source, using the flux values reported in Tables 3.2 and 3.3. These two forbidden emission lines have similar velocity ranges of about $\pm 200\,\mathrm{km\,s^{-1}}$. To increase the signal-to-noise ratio and thus reduce the

	A_V (mag)	$L_{\mathrm{acc,\,Br}\gamma}$ ($L_\odot$)	$\dot{M}_{\mathrm{acc,\,Br}\gamma}$ ($M_\odot\,\mathrm{yr}^{-1}$)	$L_{\mathrm{acc,\,Pa}\beta}$ ($L_\odot$)	$\dot{M}_{\mathrm{acc,\,Pa}\beta}$ ($M_\odot\,\mathrm{yr}^{-1}$)
2005	15 ± 1	0.039 ± 0.007	$(2.1 \pm 0.4) \times 10^{-8}$	0.023 ± 0.009	$(1.2 \pm 0.5) \times 10^{-8}$
2013	24 ± 1	0.68 ± 0.09	$(3.6 \pm 0.5) \times 10^{-7}$	0.29 ± 0.08	$(1.5 \pm 0.4) \times 10^{-7}$

Table 3.4: Visual extinction (A_V) values calculated using the ratio [Fe II] 1.644/1.257 μm and mass accretion rates ($\dot{M}_{\mathrm{acc}}$) calculated from the Brγ and Paβ line luminosities using the relation from Alcalá et al. (2017). The average of the $\dot{M}_{\mathrm{acc}}$ found from the Brγ and Paβ lines is $\dot{M}_{\mathrm{acc,\,avg}} = (1.7 \pm 0.5) \times 10^{-8}\,[M_\odot\,\mathrm{yr}^{-1}]$ for 2005 and $\dot{M}_{\mathrm{acc,\,avg}} = (2.6 \pm 0.5) \times 10^{-7}\,[M_\odot\,\mathrm{yr}^{-1}]$ for 2013.

Note. The errors propagated for the $\dot{M}_{\mathrm{acc}}$ for both Paβ and Brγ are underestimates, as the errors present in the conversion from line flux to accretion luminosity (the a and b values found in Alcalá et al., 2017) were omitted in order to compare the values found in the different epochs (which would be affected the same way by this conversion). This remains valid when comparing the values of $\dot{M}_{\mathrm{acc}}$ found from the same line over two different periods. However, in order to compare between the values of $\dot{M}_{\mathrm{acc}}$ found from two different lines, these errors on a and b would need to be taken into consideration, and the result would be a much larger error bar for the $\dot{M}_{\mathrm{acc}}$ values that would bring the measurements from Brγ and Paβ into agreement. Here, the former is preferred.

uncertainties, the fluxes of the different velocity components were combined. As the SINFONI data (2010 and 2014 epochs) did not contain J band observations, a measurement of the integrated flux of the [Fe II] 1.257 μm line was not possible. The measured A_V value changes from 15 ± 1 mag in 2005 to 24 ± 1 mag in 2013 (as reported in Column 2 of Table 3.4). These values are similar to those found in other studies towards Class I protostars (Davis et al., 2011). It is important to note that these values represent lower limits for the extinction on source, because the [Fe II] lines originate in the jet.

3.3.4 Accretion-Tracing Lines

The Brγ and Paβ lines are understood to primarily trace the accretion activity of the young star (e.g. Muzerolle et al., 1998; Calvet et al., 2004; Alcalá et al., 2017). An empirical correlation exists between the accretion luminosity (L_{acc}) and the luminosity of these hydrogen-recombination lines (L_{line}), among other emission lines. The robustness of this correlation is questioned in Mendigutia et al. (2015) where it is explored whether the correlation between $L_{\mathrm{acc}} - L_{\mathrm{line}}$ is directly tracing a physical accretion process or indirectly by probing winds or outflows that are powered by accretion. The authors suggest the use of the $L_{\mathrm{acc}} - L_\star$ correlation that also empirically exists when investigating the possible physical origins of phenomena. Here, I am comparing multiple epochs of L_{acc} estimates and have chosen to use the $L_{\mathrm{acc}} - L_{\mathrm{line}}$ correlation as my dataset includes high SNR spectra of known accretion-tracing lines, allowing for a decent calculation of L_{line}.

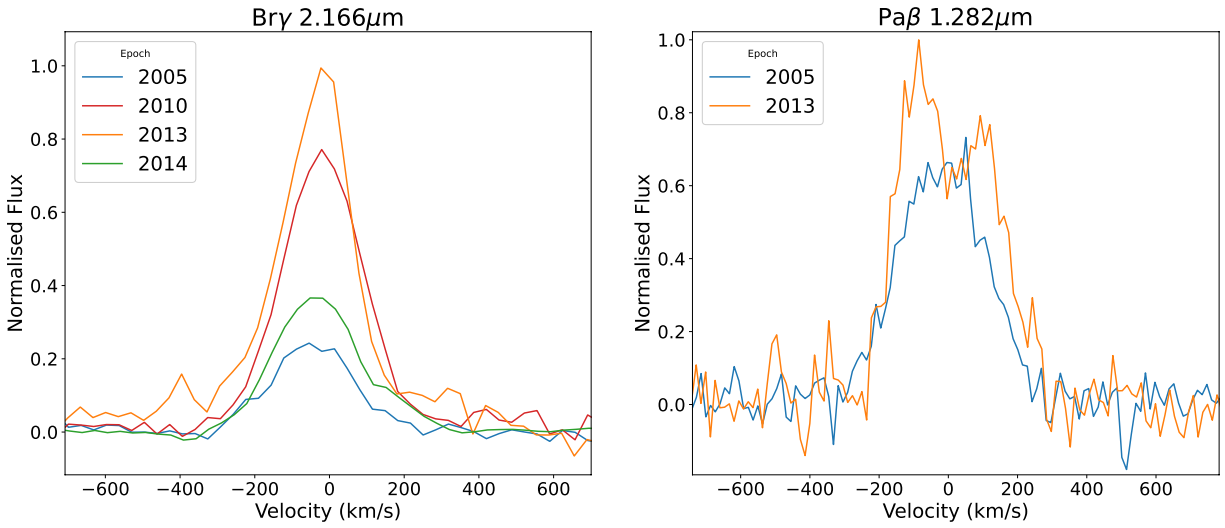

(a) Brγ 2.166 μm **(b)** Paβ 1.282 μm

Figure 3.7: Line profiles of the **(a)** Brγ 2.166 μm and **(b)** Paβ 1.282 μm hydrogen-recombination lines. Both lines are continuum-subtracted and have been corrected to the cloud velocity and normalised to the 2013 peak flux densities. In **(a)** the ISAAC spectral data (epochs 2005 and 2013) have been smoothed to match the lower spectral resolution of the SINFONI data (epoch 2014). In **(b)**, this was not necessary as only ISAAC data contained J band observations.

However, this does not mean that the chosen emission lines contain no contamination from winds/outflows, rotation effects, scattering, etc. The uncertainty introduced from these effects is incorporated into the $L_{\rm acc} - L_{\rm line}$ correlation measured in Alcalá et al. (2017) where a survey of accretion young stars are analysed without removing these smaller effects on the individual accretion-tracing lines.

As expected of lines tracing the same processes, both of these lines follow similar trends of increasing flux in the accretion burst between 2005 and 2013. In 2014, a decrease is seen in the Brγ line (Fig. 3.7). The values of the fluxes of these lines can be found in Tables 3.2 and 3.3. Figure 3.7a shows the continuum-subtracted line profiles of the Brγ (2.166 μm) line emission present in the data from the epochs 2005, 2010, 2013 and 2014 normalised to the peak intensity of the 2013 epoch. Due to the different spectral resolution of ISAAC and SINFONI, the ISAAC spectra were re-sampled to match the lower resolution of the SINFONI data for comparison purposes. Subsequently, this line was found to have an average FWZI of $\sim$765 km s^{-1}. The intensity of the Brγ line flux increased by about a factor of five from 2005 (blue) to 2013 (orange), and then in 2014 (green) dropped to an intensity of only $\sim$ 40% of the peak of 2013 (orange). As a tracer of accretion processes, this decrease in Brγ emission suggests that accretion

decreased dramatically between the 2013 and 2014 epochs, a much sharper change than the peak increase from 2005 to 2013. The integrated flux and radial velocity of the Brγ emission across all four epochs can be found in Tables 3.2 and 3.3.

In Fig. 3.7b, the Paβ (1.282 μm) line profiles from two epochs are shown normalised to the peak intensity of the 2013 epoch in the J band. It is apparent that the change in flux from 2005 to 2013 was much less pronounced at this wavelength range than in the K band (see Brγ in Fig. 3.7a); the intensity in 2005 was $\sim$70% that of the peak intensity in 2013. In comparison the Brγ line in 2005 only reached $\sim$25% of the peak intensity of that in 2013. However, it is worth noting that the line profiles shown in Fig. 3.7 are not de-reddened. De-reddening is the removing of effects of extinction (A_V effects shorter wavelengths more strongly, effectively "reddening" the spectrum) on a spectral feature. Once de-reddened (see Figs. 3.11 and 3.12), the differences in flux between the 2005 and 2013 epochs are readily visible.

3.3.5 Outflow-tracing lines

Jets provide an environment where shocks can break up dust grains releasing, for example, refractory elements like Fe into the gas phase (see, e.g. Nisini et al., 2002; Nisini, 2008). Two [Fe II] lines in particular (1.644 μm and 1.257 μm) are understood to be tracing the outflow activity in IRS 54 (Connelley & Greene, 2014). They are consistent in their trends of flux increase and eventual decrease, as for the Brγ and Paβ lines, as seen in Fig. 3.8. This trend suggests that the YSO ejection activity close to the source follows the same path as that of accretion.

These forbidden emission lines can exhibit multiple and often complex velocity components (Davis et al., 2001). The high-velocity component (HVC) is generally associated with the jet at higher velocities on larger scales, while the low-velocity component (LVC) originates from a more compact and dense region at the base of the jet (see, e.g. García-López et al., 2009). Both [Fe II] lines show evidence of a HVC and LVC, which are both blue-shifted. Potential red-shifted components of the HVC's of both the [Fe II] 1.257 μm and 1.644 μm lines are just about visible at $\sim$+100 km s^{-1}. However, it is heavily blended with the LVC and surrounding noise. The difficulty in separating the different velocity components is not unexpected given the (almost edge-on) geometry of the disk.

In addition to atomic emission, molecular hydrogen (H_2) emission is also detected and shown in Fig. 3.8c, where the shift in peak velocity is due to the spectral resolutions of ISAAC and SINFONI. This traces dense molecular gas of relatively low excitation ($n_{H_2} \geq 10^5\,\mathrm{cm}^{-3}$, T $\sim$ 2000 K Caratti o Garatti et al., 2006). The brightest

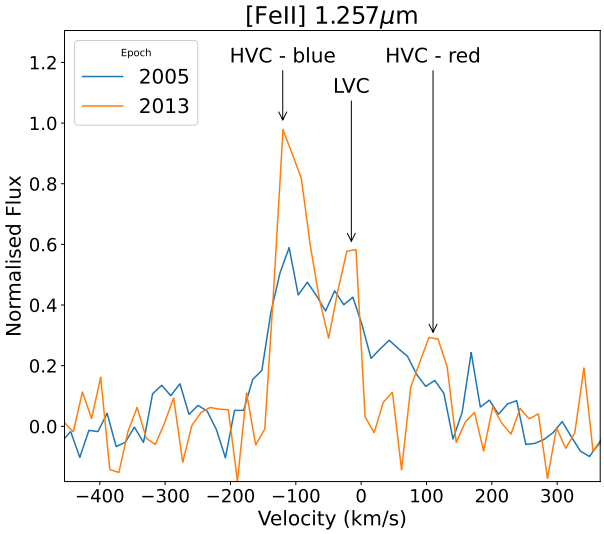

(a) [Fe II] 1.257 μm

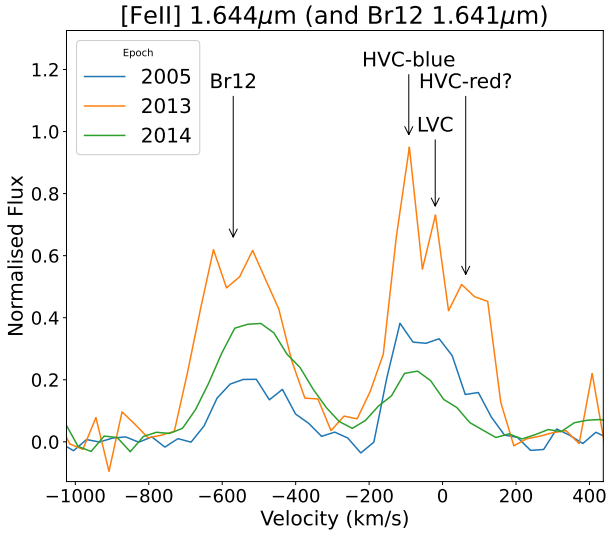

(b) [Fe II] 1.644 μm

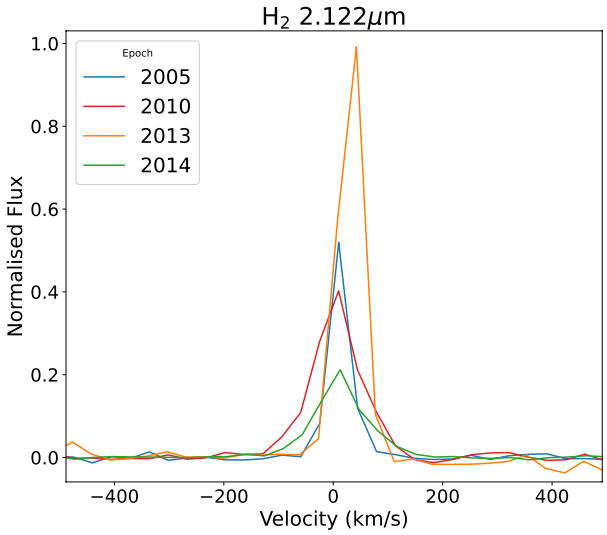

(c) H_2 2.122 μm

Figure 3.8: **(a)** and **(b)** Line profiles of [Fe II] at 1.257 μm and 1.644 μm. **(c)** Line profile of molecular hydrogen (H_2) 2.122 μm. All lines are continuum-subtracted and have been corrected to the cloud velocity. In **(b)** and **(c)**, the ISAAC spectral data (epochs 2005 and 2013) have been smoothed to match the lower spectral resolution of the SINFONI data (epoch 2014); in **(a)**, this was not necessary as only ISAAC data contained J band observations. Notably, there are different velocity components present. The red-shifted HVC in **(b)** cannot be separated as it is blended with the LVC. In **(b)** the Br12 (1.641 μm) line is also shown to highlight how the 2014 epoch (green line) changes differently in the outflow-tracing [Fe II] emission from the accretion-tracing Br12 line.

Date yyyy-mm-dd	Instrument	J (mag)	H (mag)	K (mag)	Ref.
1994-04-25	KPNO/SQIID	16.63 ± 0.10	13.50 ± 0.10	10.87 ± 0.10	1
1999-03-29	DENIS	14.90 ± 0.12	-	8.666 ± 0.060	2
1999-04-17	2MASS	14.678 ± 0.037	11.189 ± 0.029	8.713 ± 0.023	3
2002-03-01	IRTF/NSFCAM	16.38 ± 0.10	12.22 ± 0.04	10.15 ± 0.02	4
2005-06-16	VLT/ISAAC	16.00 ± 0.25	13.12 ± 0.17	10.80 ± 0.18	-
2008-05-24	AAT/IRIS2	15.71 ± 0.20	12.47 ± 0.20	10.44 ± 0.20	5
2010-06-14	VLT/SINFONI	-	-	9.83 ± 0.10	6
2013-06-12	VLT/ISAAC	15.90 ± 0.35	12.06 ± 0.13	-	-
2013-09-12	VLT/ISAAC	-	-	9.67 ± 0.05	-
2014-05-22	VLT/SINFONI	-	12.30 ± 0.20		-
2014-06-02	VLT/SINFONI	-	-	10.10 ± 0.10	-

Table 3.5: Photometry measurements from J (1.25 μm), H (1.65 μm) and K (2.16 μm) filters.

References. **(1)** Barsony et al. (1997); **(2)** DENIS Consortium (2005) ; **(3)** Cutri et al. (2003); **(4)** Haisch, Jr. et al. (2004); **(5)** Barsony et al. (2012); **(6)** García-López et al. (2013).

transition detected is the 1-0 S(1) line at 2.122 μm (other H_2 lines are also present in the data, but their signal-to-noise ratio values are much lower). Figure 3.8c shows the line profile at different epochs. Notably, between 2013 and 2014 the intensity dropped to $\sim$ 20% of the peak, below even that of the earliest (2005) epoch. This trend can be seen in the [Fe II] 1.644 μm line as well, but not in the Bracket or Paschen hydrogen-recombination lines (whether this trend is also seen in the [Fe II] 1.257 μm line cannot be confirmed due to the lack of J band data in 2014). This is consistent with expectations that the H_2 and [Fe II] emission are tracing different processes in IRS 54 than the Brackett and Paschen lines. The H_2 and [Fe II] lines trace the outflow, while the Brackett and Paschen lines trace accretion activity closer to the star and inner disk.

3.3.6 Photometry

In order to put these observations in perspective and investigate the variability of IRS 54 across a broader time frame and at different wavelengths, the SINFONI and ISAAC photometry are combined with archival and literature photometric data for IRS 54 obtained by 2MASS (2 Micron All Sky Survey), the SQIID (Simultaneous Quad-Color Infrared Imaging Device) at Kitt Peak National Observatory, DENIS (Deep Near Infrared Survey), NSFCAM (NASA), the Anglo-Australian Telescope (AAT) and the Wide-field

Date yyyy-mm-dd	Instrument	W1 (mag)	W2 (mag)	Ref.
2010-02-27	WISE	8.135 ± 0.041	6.424 ± 0.057	7
2010-08-28	WISE	6.774 ± 0.015	4.796 ± 0.013	7
2014-03-02	NEOWISE	7.230 ± 0.018	5.626 ± 0.016	8
2014-08-28	NEOWISE	7.116 ± 0.021	5.549 ± 0.016	8
2015-02-27	NEOWISE	6.927 ± 0.021	5.385 ± 0.017	8
2015-08-25	NEOWISE	6.955 ± 0.020	5.252 ± 0.019	8
2016-02-26	NEOWISE	6.858 ± 0.020	5.407 ± 0.016	8
2016-08-18	NEOWISE	6.792 ± 0.022	5.444 ± 0.017	8
2017-02-27	NEOWISE	7.269 ± 0.020	5.656 ± 0.016	8
2017-08-13	NEOWISE	7.399 ± 0.018	5.795 ± 0.016	8
2018-02-27	NEOWISE	7.172 ± 0.019	5.512 ± 0.018	8
2018-08-09	NEOWISE	7.107 ± 0.019	5.505 ± 0.015	8
2019-03-01	NEOWISE	7.495 ± 0.016	5.867 ± 0.016	8
2019-08-11	NEOWISE	7.299 ± 0.018	5.651 ± 0.015	8

Table 3.6: Photometry measurements from W1 (3.4 μm) and W2 (4.6 μm) filters.

References: **(7)** Wright et al. (2010) (WISE is a joint project of the University of California, Los Angeles, and the Jet Propulsion Laboratory/California Institute of Technology, funded by the National Aeronautics and Space Administration.); **(8)** Mainzer et al. (2011, 2014).

Infrared Survey Explorer (WISE). These data can be seen in Fig. 3.9 and Tables 3.5 and 3.6, where their respective sources are cited. The WISE data (MIR) were used to obtain an idea of how the object has varied at these longer wavelengths where extinction is less influential. J, H and K bands all show a similar trend in luminosity variability, while the MIR observations (bands $W1$ and $W2$ at 3.4 μm and 4.6 μm, respectively) show the brightness peaking in 2010. Their steep rise suggests that the maximum has happened around the epochs of 2010 or 2011 rather than in 2013. However, due to the gaps in photometry between 2010 and 2013, it is impossible to define when the maximum of each light curve takes places. As monitoring data were available from NEOWISE between 2014 and 2019, it can be seen from the photometry in 2014 that $W1$ and $W2$ magnitudes dropped with respect to 2010, and after that there is a smooth secondary maximum followed by an erratic dimming of the source.

Multi-epoch archival data in the J, H and K bands show a large variability of up to two magnitudes during the decade preceding the 2005 observations. The observed variability in IRS 54 seems therefore to be episodic rather than a single event witnessed in these observations. 2MASS NIR archival data indicate that in 1999 the object was $\sim$1 mag brighter than the peak seen in this study. However, it is worth noting the differing spatial resolution and likely contamination from the surrounding nebulosity in the region in the 2MASS data. Nevertheless, as there are also DENIS data (in J and K bands) from the 1999 epoch that agree with the 2MASS data points, it can be trusted that IRS 54 brightened around 1999 and then a quiescent state followed until the more recent surge observed between 2010 and 2013.

3.3.7 Accretion variability

As discussed in Section 1.2.2, the accretion luminosity can be calculated through the relation between $L_{\rm acc}$ and $L_{\rm line}$ (see Fig. 1.10 and Eq. 1.17). In this equation, a and b are the parameters derived in Alcalá et al. (2017) and depend on the particular line being measured: the Brγ line has corresponding values of $a = 1.19 \pm 0.10$ and $b = 4.02 \pm 0.51$ and the Paβ line has corresponding values of $a = 1.06 \pm 0.07$ and $b = 2.76 \pm 0.34$. The mass accretion rate can then be found by using Eq. 1.13 and the resultant values can be found in Table 3.4.

I derive an average from these two lines to obtain a value of $\dot{M}_{\rm acc} = (1.7 \pm 0.5) \times 10^{-8}\,{\rm M}_{\odot}\,{\rm yr}^{-1}$ in 2005 and $(2.6 \pm 0.5) \times 10^{-7}\,{\rm M}_{\odot}\,{\rm yr}^{-1}$ in 2013. This shows that the mass accretion rate increases by one order of magnitude between 2005 and 2013. Notably, the A_V increases in tandem with the $\dot{M}_{\rm acc}$, although an increase in extinction is normally associated with a decrease in flux. However, in the case of IRS 54 the accretion burst is

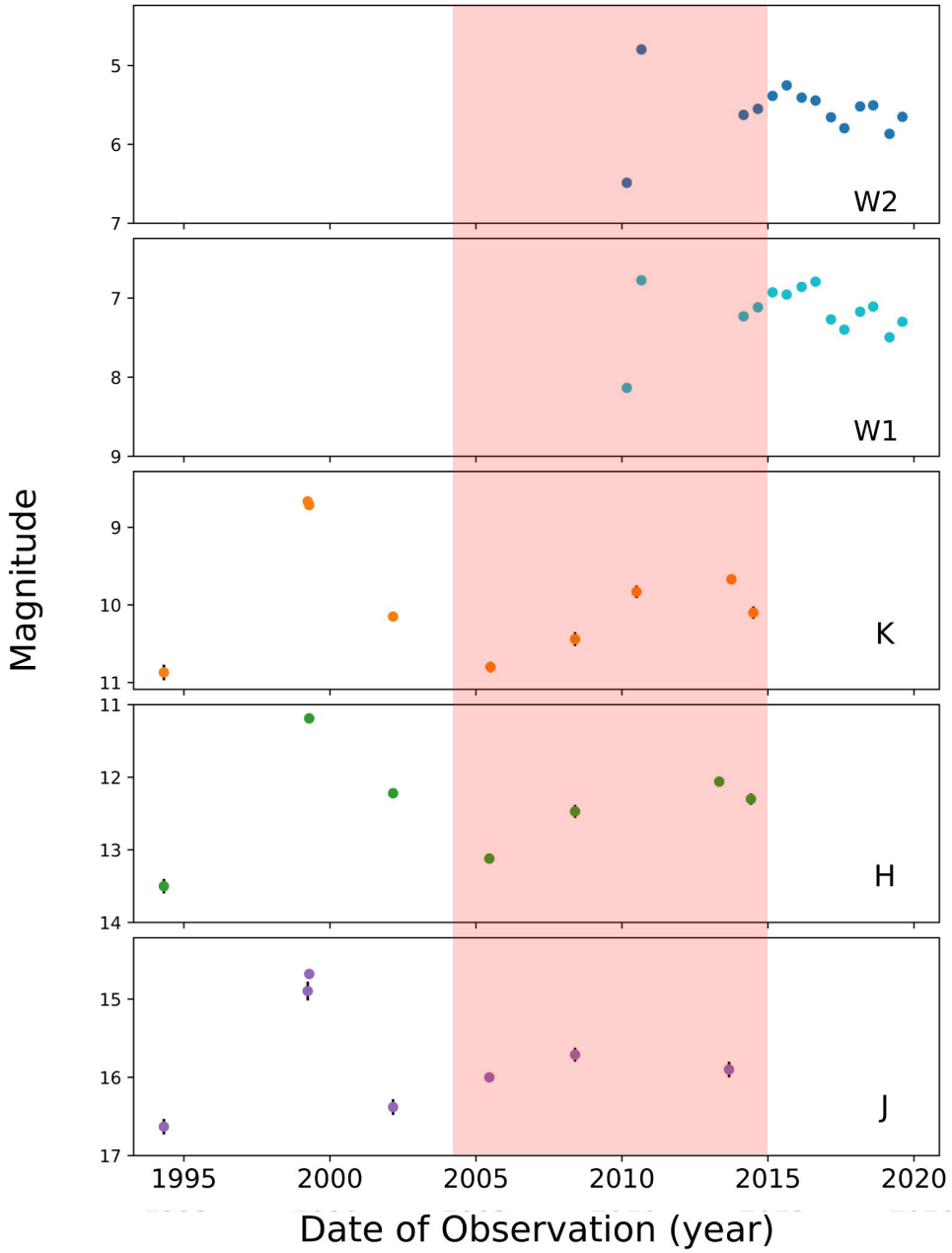

Figure 3.9: Photometry of IRS 54. The archival data are described in Tables 3.5 and 3.6. The data from SINFONI and ISAAC are also included. The shaded region indicates the four epochs discussed in this paper and the accretion burst detected. The error bars are in black, however, are often smaller than the points themselves.

so strong that the flux increase is apparent even with the extinction dampening it.

To determine A_V, the [Fe II] line ratio is used, which originates from the jet rather than directly from the accretion region, where one would expect the HI lines to originate. As the jet is further from the surface of the star, the extinction would only decrease from the central source. However, as the SINFONI spectra were extracted on source within the $3'' \times 3''$ field of view, the extinction measured is on the part of the jet closest to the object (within $1''$ - $1.2''$ i.e. within ∼150 au of the source). Even so, these values of A_V should be taken as lower limits. Extinction dampens the apparent accretion luminosity, and therefore the apparent $\dot{M}_{\rm acc}$. As a lower limit for A_V has been calculated, the actual $\dot{M}_{\rm acc}$ may be higher than reported. This is explored further in Sect. 4.4.

For the 2010 archival data, GL13 estimate extinction on source using a different method from ours, exploiting the measured versus expected ratio of H_2 lines. This leads to an estimate of A_V of ∼30 mag. Using this value, GL13 estimate $\dot{M}_{\rm acc} \sim 3 \times 10^{-7}$ $M_\odot\, yr^{-1}$ from the relation between $L_{\rm line}$ and $L_{\rm acc}$ derived by Calvet et al. (2004). In order to compare $\dot{M}_{\rm acc}$ in 2010 with what was found in the other epochs (2005 and 2013),it was recalculated using the same Alcalá et al. (2017) relation between $L_{\rm line}$ and $L_{\rm acc}$ used throughout this study. The result is $\dot{M}_{\rm acc} = 4.3 \times 10^{-7}$ $M_\odot\, yr^{-1}$, which is slightly higher than that found in GL13. This result would then strengthen the idea of the burst maximum being closer to the 2010-2011 epochs rather than the 2013 one.

3.4 Discussion

3.4.1 Accretion and extinction variability

From the observations, it is clear that IRS 54 underwent significant changes in luminosity, accretion and extinction during the period from 2005 to 2014. This is shown clearly in Fig. 3.10 where IFU observations are shown from the 2010 and 2014 epochs on the same scale, so as to make the dramatic drop in flux between these dates obvious. Although there were no IFU observations taken during the 2013 epoch, the sharp increase in flux seen in the spectroscopy is interpreted as an accretion burst that peaked between 2010 and 2013.

The $\dot{M}_{\rm acc}$ between 2005 and 2013 (Table 3.4) increases by a factor of ~ 20, while A_V increases by nine magnitudes (flux increases by ~ 4000 in the V band and by ~ 2.4 in the K band). While both of these are significant changes, it is clear that the accretion appears to have the larger effect on the SED of IRS 54 between this time period because an overall increase in luminosity is seen, especially in the K band where the continuum flux increases by a factor of approximately six. The photometry also reflects this increase

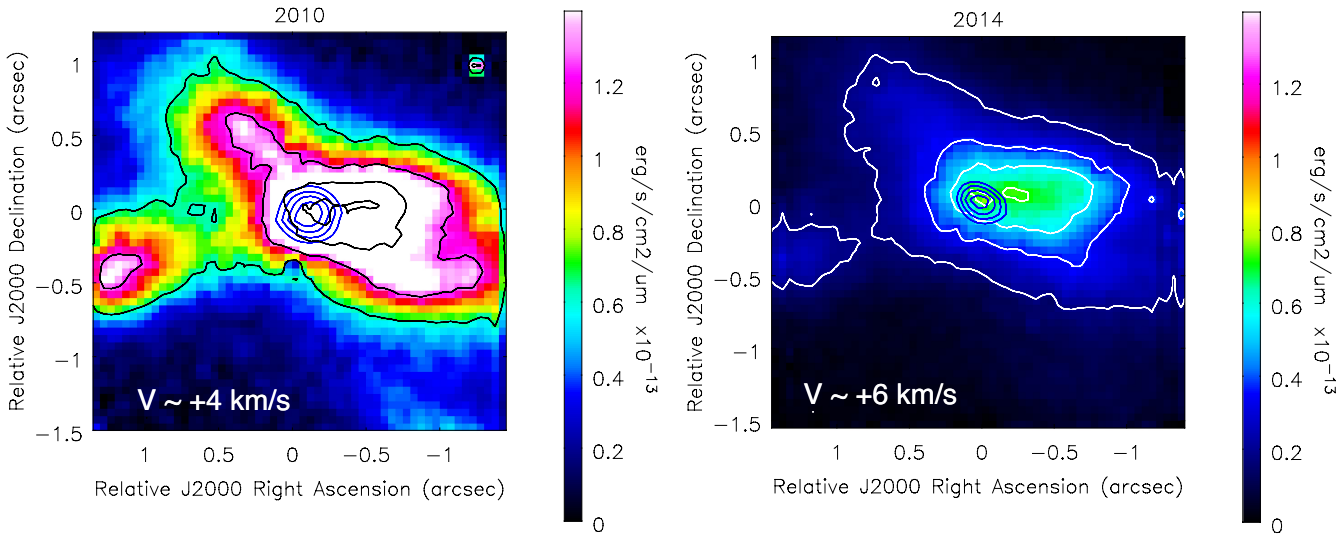

Figure 3.10: Continuum-subtracted SINFONI data from the 2010 (left panel) and 2014 (right panel) epochs taken by summing five spectral channels centred on the H_2 emission line at 2.122 μm in the K band. The blue contours represent the spatial position of the continuum of the source taken at levels of 0.2, 0.4, 0.6 and 0.8 of the continuum flux.

in flux (Fig. 3.9), supporting the idea of an accretion burst. The MIR data show that there is a large increase of over a magnitude in 2010 followed by a decrease and with subsequent small fluctuations from 2014 to 2019. The MIR shows a sharper increase in flux within 2010 than seen in the NIR which is likely due to extinction affecting these latter wavelengths to a lesser extent. To measure the effect of visual extinction on a given wavelength, the ratio A_V/A_λ can be used. In the case of the MIR, A_V/A_L is ~ 17, and A_V/A_M is ~ 43 (Rieke & Lebofsky, 1985). Namely, $A_V = 15$ mag and $A_V = 24$ mag (the values found in this study) translate to 0.88 mag and 1.41 mag in the L band, and to only 0.35 mag and 0.56 mag in the M band, respectively.

As the extinction was seen to increase between 2005 and 2013, it is important to note that the spectra shown in Fig. 3.5 are reddened due to extinction. A_V was thus calculated in the data where appropriate emission lines were available for the analysis (see Sect. 3.3.3). Between 2005 and 2013, a large increase in A_V (from $\sim$15 mag to $\sim$24 mag) is found. As line and continuum fluxes are also seen to increase in this time frame, this change cannot be accounted for solely by variable extinction. All increases of line fluxes measured here, especially in the K band, are in fact more pronounced in the de-reddened spectra (see Figs. 3.11 and 3.12). The de-reddened spectra indicate that the 2010 epoch was close to the peak of the burst, as its flux is similar to that of 2013 in the K band, when both are corrected for extinction. However, it is important to remember that the A_V in 2010 was estimated in GL13 using H_2 lines rather than the

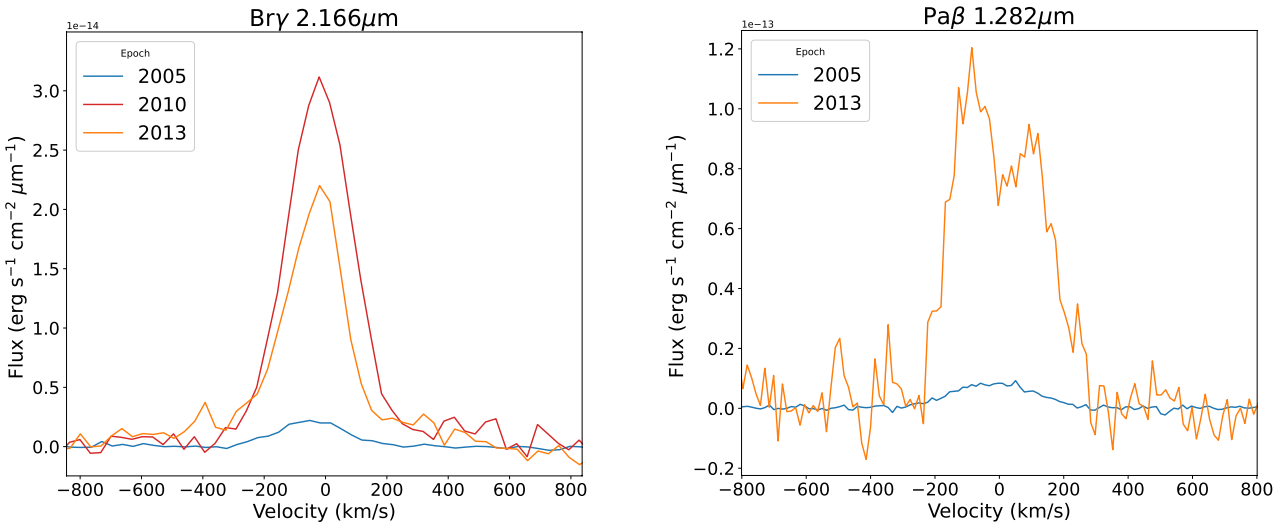

Figure 3.11: De-reddened flux of the accretion-tracing (Paβ and Brγ) lines from IRS 54. These plots were generated using the extinction values found in Table 3.4 for the 2005 and 2013 epochs. The 2010 epoch uses the extinction value found in GL13.

[Fe II] lines which were used for 2005 and 2013, and therefore caution is needed when comparing these values.

Both extinction and accretion can affect the shape of the SED of a protostar, but in different ways. An increase in accretion would result in a more pronounced increase in luminosity at shorter wavelengths. For example, in the NIR, it would increase the flux in the J band more than in the K band, effectively flattening the SED. Alternatively, an increase in extinction would result in a steeper slope of the SED in this wavelength range, decreasing the observed flux more at the shorter wavelengths (J band) than at the longer wavelengths (K band). These results indicate that the change in SED shape observed is not due solely to one or the other of these phenomena, but to a combination of the two. An increase in steepness in the slope with increased extinction is seen, but also an increase of flux in the H and especially the K bands. This combination of both accretion and extinction is representative of the complex processes at work and how they are related to one another in IRS 54. The combined effect of these two processes is quite unique, because it tends to flatten the light curves more at shorter wavelengths. This can be seen qualitatively in Fig. 3.9, where the J band light curve is much flatter with respect to the K, $W1$, or $W2$ bands. Variations in the SED of a young star can also be due to changes in the inner disk structure (e.g. Fang et al., 2014).

A possible explanation for this tandem increase of both extinction and accretion is that the increase in accretion and ejection lifts a large amount of dust from the

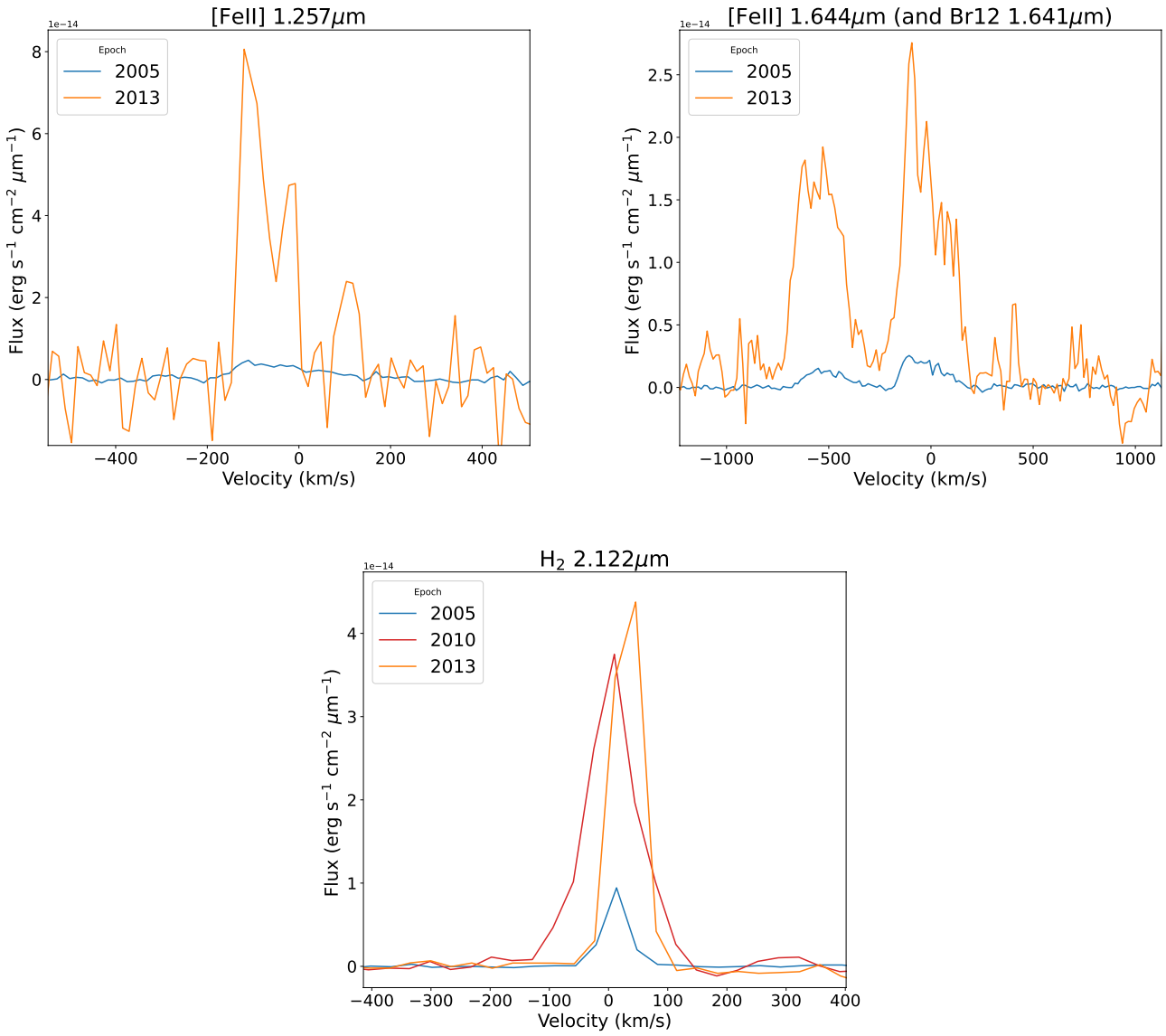

Figure 3.12: De-reddened flux of the outflow-tracing ([Fe II] and H_2) lines from IRS 54. These plots were generated using the extinction values found in Table 3.4 for the 2005 and 2013 epochs. The 2010 epoch uses the extinction value found in GL13.

disk, which crosses the line of sight and therefore produces more extinction. The edge-on geometry of the system supports this interpretation as any dust lifted as a result of an accretion or ejection burst would easily intersect the line of sight between the observer and the source. Therefore, this system demonstrates an accretion or ejection burst activity that also increases the visual extinction along the line of sight. A similar increase of extinction was observed for RW Aur, whose photometric and polarimetric variability were explained by the presence of dust in the disk wind (Dodin et al., 2019b; Koutoulaki et al., 2019b).

The mass accretion rates derived in this study are likely lower limits, as the method used to determine A_V utilised outflow-tracing lines, which originate further from the source where the extinction is lower. As can be seen in Table 3.4, the values of $\dot{M}_{\rm acc}$ derived from the two different lines are slightly different. Incorporating a higher A_V value into the calculation of $\dot{M}_{\rm acc}$ would provide a higher mass accretion rate. The accuracy of the A_V estimates is thus investigated further by plotting $\dot{M}_{\rm acc}$ derived from the Paβ and Brγ lines and the difference in accretion luminosities measured using the Paβ and Brγ lines ($\Delta L_{\rm acc}$) as a function of A_V for the 2005 (Fig. 3.13 top panel) and 2013 (Fig. 3.13 bottom panel) epochs. The $\dot{M}_{\rm acc}$ measured from each line should theoretically agree if the A_V was measured accurately. As can be seen in Fig. 3.13, the agreement between Paβ and Brγ in 2005 is strongest in the low extinction limit, and it diverges for A_V values larger than ~ 20 mag. In the 2013 case, the difference between $\dot{M}_{\rm acc}$ calculated using either line is largest at A_V values $\sim$25 mag, which is where the measurement of $A_V \sim 24$ mag resides. However, this strengthens the assumption that this is a lower limit for extinction, as values approaching 30 mag provide better agreement. The red star in Fig. 3.13 represents the value for A_V that minimises the disparity between the $\dot{M}_{\rm acc}$ values derived from Brγ and Paβ measurements, which is at $A_V \sim$18.5 mag in 2005 and $\sim$29.5 mag in 2013. This is most likely close to the actual extinction toward the source in 2013. These A_V values correspond to $\dot{M}_{\rm acc} \sim 3.1 \times 10^{-8}\,{\rm M}_\odot\,{\rm yr}^{-1}$ in 2005 and $\dot{M}_{\rm acc} \sim 7.3 \times 10^{-7}\,{\rm M}_\odot\,{\rm yr}^{-1}$ in 2013, respectively.

3.4.2 Jet variability and asymmetry

Examining the H_2 line emission maps in Fig. 3.10, the 2014 epoch exhibits lower luminosity in line emission than that of the 2010 epoch. Whether the luminosity in the region of the jet was also changing was sought for investigation. In principle, the jet would not be expected to change instantaneously with a change in accretion. Although accretion and ejection are linked, the observed jet emission originates from further out in the system and consequently takes longer to reflect an increase in accretion. There-

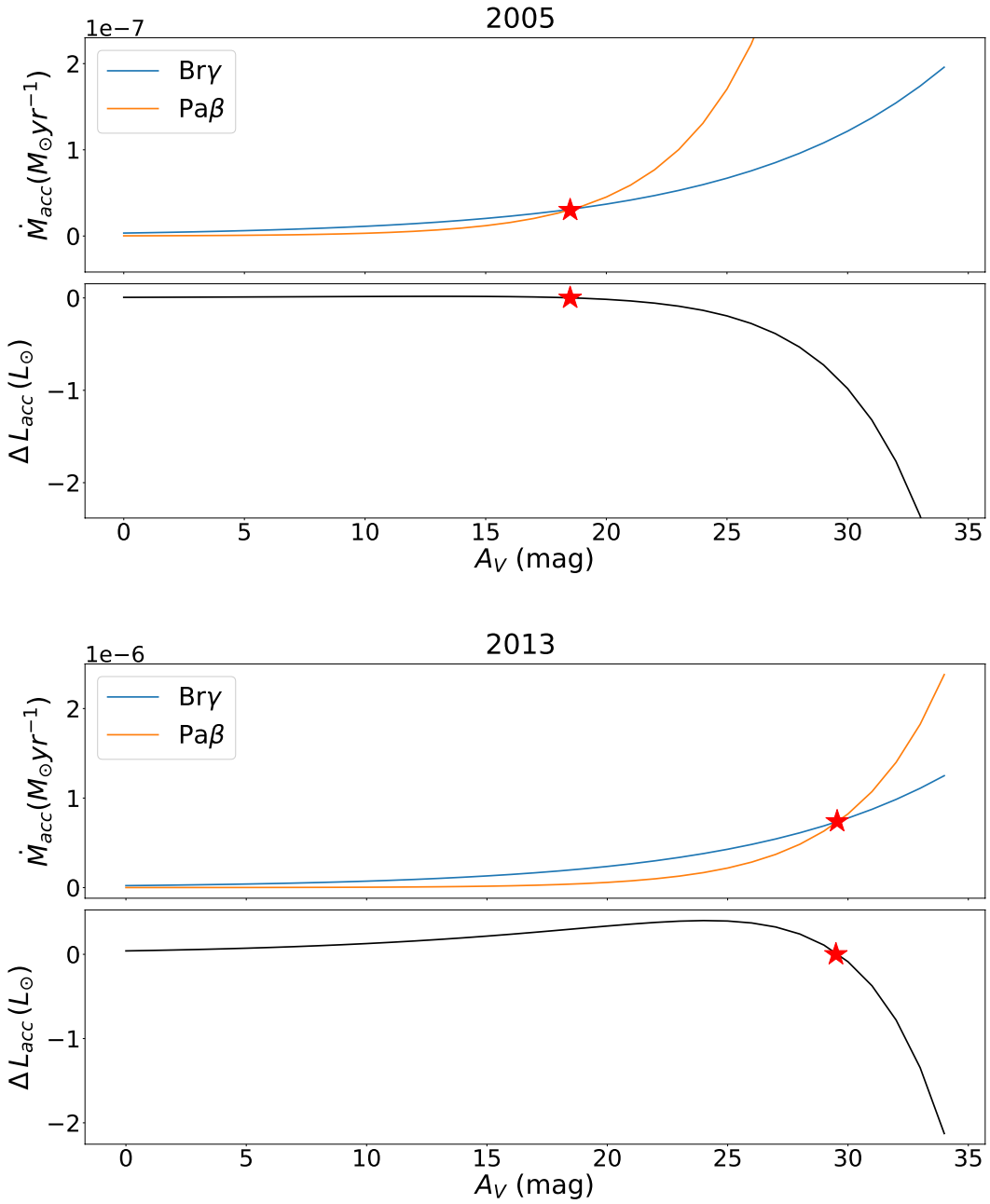

Figure 3.13: Plots $\dot{M}_{\rm acc}$ and $\Delta L_{\rm acc}$ vs. A_V for the 2005 (top panel) and 2013 (bottom panel) epochs. The blue line represents the measurement of $\dot{M}_{\rm acc}$ using the Brγ line luminosity and the orange line represents the measurement of $\dot{M}_{\rm acc}$ using the Paβ line luminosity. The red stars represent the value of A_V where the Brγ and Paβ de-reddened fluxes best agree in calculating the $\dot{M}_{\rm acc}$.

fore, between 2010 and 2014, where accretion was observed to change, the jet would not necessarily change accordingly. To determine this, spectra from multiple regions of the same size across the SINFONI image were extracted in 2010 and 2014 and compared. Unexpectedly, the flux of the regions extracted along the jet was found to vary between the two epochs. A possible explanation is that these regions are contaminated by scattered light, which does reflect the changes in accretion luminosity. The cavity walls surrounding the central source are also illuminated by this scattered light and their flux also increases during the burst.

It is clear that the jet of IRS 54 has both an atomic and a molecular component, as seen in Figs. 3.3 and 3.4 where the H_2 line emission is predominantly red-shifted and the [Fe II] line emission is predominantly blue-shifted. This implies different excitation conditions and possibly different velocities of the jet material ejected in the two lobes. This asymmetry could be due in part to the inhomogeneity of the interstellar medium (ISM) in the region, or is potentially an effect of a misalignment in the magnetic fields of the protostar, but investigating this issue is beyond the scope of this study.

It is also interesting to note that during the 2014 epoch dimming, the flux from the jet-tracing lines (H_2 and [Fe II]) dropped to a flux lower than that of 2005. In contrast, the flux from accretion-tracing lines (Paβ, Br12 and Brγ) during 2014 dropped only to a flux between that of 2005 and 2010, which reflects how the continuum changed during this period across all bands (J, H and K). This difference in how the flux changed in 2014 is most obviously seen in Fig. 3.8b where Br12 line is adjacent to the [Fe II] 1.644 μm emission line. This implies that the processes of accretion and ejection are not behaving synchronously following the burst, as would be expected considering they originate from different regions.

3.4.3 A new EXor object?

The increase of mass accretion rate seen in IRS 54 is consistent with that observed in EXor objects. In addition, EXor burst timescales and frequencies are also in line with the observations of IRS 54. As these observations are at NIR wavelengths, the observed increase in luminosity of IRS 54 is lower than what would be observed in typical, much less embedded EXors, which are usually observed at optical wavelengths and are therefore expected to be larger. If one considers this and the fact that IRS 54 is a very low-mass star, its luminosity increase is likely on par with typical Exor-type bursts. The brightness of IRS 54 increases by more than one magnitude in the K band (and varies by more than two magnitudes over 20 years in the J, H and K bands) and $\dot{M}_{\rm acc}$ increases by at least an order of magnitude.

I also note a similar behaviour of EX Lup and IRS 54 light curves in the MIR in terms of strength, duration and shape (see Figure 1 of Ábrahám et al., 2019, and this study's Fig. 3.9). As for IRS 54, EX Lup $W1$ and $W2$ light curves (during the 2011 burst) have a similar shape, showing a steep rise at the beginning and a smoother flickering decline lasting a few years, as indeed seen in IRS 54 (see top panels of Fig. 3.9). In both objects the MIR brightness increases by a couple of magnitudes.

Both the duration (a few years) and intensity of the burst hint at an EXor-type event, although some of the typical disk spectral features are missing, such as the CO band head lines in emission and Na lines. This might be due to the system geometry of IRS 54, which prevents the inner disk from being seen, as these signatures originate from that region. On the other hand, the hydrogen lines detected in IRS 54 that trace accretion are likely seen in scattered light. If present, the low-J lines from the v = 2 − 0 CO band head ~~are~~ seen in absorption would suggest cold gas (with a temperature of a few hundred Kelvin), likely originating from the outer disk atmosphere, absorbing emission coming from a hotter (inner) region emitting CO. This might hint at CO band heads in emission, typical of EXor bursts being present in the inner gaseous disk. However, it would be necessary to obtain higher signal-to-noise spectra in the K-band to be certain of the existence of these CO lines in IRS 54 and subsequently use them as further evidence of it having undergone an EXor-type burst. While it is not possible at this time to definitively decipher whether or not IRS 54 is an EXor-type object, the issue is worthy of further investigation, as this source would be the first very low-mass protostar where an EXor-type burst is observed.

3.5 Conclusions

In the course of this study, data obtained with ISAAC and SINFONI over four epochs (2005, 2010, 2013 and 2014) were reduced and analysed to assess variability in IRS 54. This was done over the wavelength range 1.24 μm to 2.45 μm (J, H and K bands). Significant changes in flux were found between the epochs, reflecting an increase between 2005 and 2013 and a drop in 2014. The lightcurves in the $W1$ and $W2$ bands show a similar behaviour, showing a steep rise in 2010 and possibly a secondary maximum after 2014. This increase in luminosity is accompanied by a burst in the mass accretion rate, $\dot{M}_{\rm acc}$, which increases from $\sim 1.7 \times 10^{-8}\,M_\odot\,{\rm yr}^{-1}$ in 2005 to $\sim 2.6 \times 10^{-7}\,M_\odot\,{\rm yr}^{-1}$ in 2013. The peak of the burst occurred between 2010 and 2013. This burst is consistent with the photometric data that have been gathered during these same epochs. Going back to archival data from 1999, the photometry illustrates that this protostar went

through a previous change in luminosity between 1999 and 2005 of approximately two magnitudes in the J, H and K bands (Fig. 3.9). These two large changes in flux suggest these bursts may be episodic.

Specific emission lines were analysed for this variability and to calculate $\dot{M}_{\rm acc}$ and A_V, which demonstrated an increase in tandem with one another. Maps of the jet-tracing emission (H_2 and [Fe II]) were also generated to examine how the emission varied spatially about the central star of the YSO. The [Fe II] was found to be emitting predominantly from the blue-shifted component of the jet, and the H_2 was found to be illuminating the cavity walls with scattered light, while primarily originating from the red-shifted component of the jet. This asymmetry is notable and may help understand the inner mechanism at work in the YSO. Two of the possible causes for this asymmetry in emission from the jet are that the interstellar medium in the region may be inhomogeneous or that there may be misaligned magnetic fields in the protostar.

Examining the SED of each epoch and its variability, it is deduced that the changes it exhibits reflect a combination of both an increase in accretion and extinction. A possible explanation for this tandem increase in these two parameters is that the increased accretion and ejection activity during the burst lifts up material into the line of sight and obscures the YSO.

The timescales of the burst seen in IRS 54 are reminiscent an EXor-type object, and its increase in luminosity is exceptionally large over a short period of time, especially considering it is a VLMS. Further investigation of IRS 54 as a potential EXor-type object is warranted as, if found to be true, IRS 54 would be the lowest mass Class I source observed to have this type of violent bursts in accretion and ejection.

4

Accretion variability in RU Lup

Camille Stock, Pauline McGinnis, Alessio Caratti o Garatti, Antonella Natta, & Tom P. Ray, (2022), Astronomy & Astrophysics, 668, A94,
https://doi.org/10.1051/0004-6361/202244315

4.1 Introduction

Many processes at work in low-mass ($M_* \leq 2\,\mathrm{M}_\odot$) young stars influence their formation and evolution. Two of the most important are accretion and ejection of material onto and emanating from young stars, such as TTSs (see Section 1.1.4). The CTTSs demonstrate a rich emission spectrum mostly due to accretion of material theorised to be structured as funnels, flowing along the stellar magnetic field lines from the inner disk to the stellar surface (see Section 1.2.1). Other spectral lines come from the ejection phenomena. They are varied in their structures (e. g. jets and winds) and velocities, depending on the conditions from which they originate, however it has been shown that a strong link between ejection and accretion exists (e .g. Ray et al., 2007, and references therein).

Accretion in young stars is not a steady process but rather variable (for a review see Fischer et al., 2022, and references therein). Understanding how young stars' accretion activity varies is vital for determining how they gain their mass and what implications that process has on their evolution (Herbst et al., 1994). Indeed, luminosity amplitude and time-scales vary depending on the origin of such variability (see Figure 3 of Fischer et al., 2022). Temporal changes over timescales of days and amplitudes less than one order of magnitude in the accretion rate (the so-called "Routine Variability", see Fischer et al., 2022) are often attributed to rotation of the star and are very useful in measuring its rotation period (e.g. Scholz & Jayawardhana, 2006; Costigan et al., 2012; Costigan et al., 2014; Rebull et al., 2014). However, this is not always the case and removing the rotation contribution to the perceived variability is necessary to probe any intrinsic changes that might come from the stellar-disk magnetospheric interaction. On the other hand, the so-called accretion bursts with larger amplitude (more than one order of magnitude) and time-scale variability (from months to years) are more related to the disk's mass transport and refurbishment, and might originate from disk instabilities and other related mechanisms relevant to EXor and FUor phases (Hartmann et al., 2016).

Therefore, studying the variation of L_{acc} and $\dot{M}_{\mathrm{acc}}$ is important in understanding how TTSs form. Magnetospheric accretion can be divided into two regimes: stable and unstable. These two regimes were predicted by several 3D magnetohydrodynamic (MHD) simulations of disk accretion onto a rotating young star (Romanova et al., 2008;

Distance	158.9 ± 0.7	pc	Gaia Collaboration et al. (2018)
Age	$2-3$	Myr	Herczeg et al. (2005)
$M_\star$	~ 0.65	$M_\odot$	Herczeg et al. (2005)
$R_\star$	~ 1.64	$R_\odot$	Herczeg et al. (2005)
SpT	K7	-	Bailer-Jones et al. (2018)
$T_{\rm eff}$	4037 ± 96	K	Frasca et al. (2017)
$L_\star$	1.313 ± 0.605	$L_\odot$	Alcalá et al. (2017)
$P^*_{\rm rot}$	3.71 ± 0.01	days	Stempels et al. (2007)
$v \sin i$	8.5 ± 4.8	km s^{-1}	Frasca et al. (2017)
A_V	~ 0.07	mag	Herczeg et al. (2005)
i^{**}	$16 \pm {}^{6}_{8}$	$^\circ$	Gravity Collaboration et al. (2021)

$*$ Calculated from radial velocity measurements;
$**$ Disk inclination with respect to the plane of the sky

Table 4.1: Stellar properties of RU Lup.

Kulkarni & Romanova, 2008, 2009). According to these models, the main factors that determine in which regime a star accretes are the mass accretion rate, the strength of the magnetic field, the stellar rotation rate, and the misalignment between the star's rotation axis and its magnetic poles.

CTTS accretion activity and variability can also be studied by using veiling. This is the filling-in of stellar photospheric absorption features such that they appear more shallow in observed spectra of an actively accreting young star, due to an accretion-fueled flux excess (both in the continuum and in lines). This phenomenon has been investigated since Joy (1949) first introduced the concept of veiling. With high resolution spectroscopy, it is possible to observe the photospheric absorption lines of the star and this excess due to accretion that effectively veils the spectrum.

This study focuses on the CTTS RU Lup, which is known to have a plethora of strong accretion features (Herczeg et al., 2005; Gahm et al., 2008; Siwak et al., 2016, and references therein). RU Lup is an accreting CTTS of $2-3$ Myrs that lies in the Lupus star-forming region at a distance of $d \approx 159$ pc (Gaia Collaboration et al., 2018). It has a rotational period of 3.71 ± 0.01 (Stempels et al., 2007) and is notable for its strong emission lines and veiling. These accretion-tracing lines are exceptionally broad, for example, the EW of the Hα emission line is usually found to be greater than 100 Å (Siwak et al., 2016). In their models, this high accretion activity was found by Lamzin et al. (1996) to be responsible for the majority of the observed luminosity, whereby only about 10% is generated by gravitational contraction of the star itself. The $\dot{M}_{\rm acc}$ was calculated by Herczeg & Hillenbrand (2008) and found to be $\sim 1.8 \times 10^{-8}\, M_\odot\, {\rm yr}^{-1}$. The study by Alcalá et al. (2017) resulted in values of $\sim 6.7 \times 10^{-8}\, M_\odot\, {\rm yr}^{-1}$.

In Herczeg & Hillenbrand (2008), the combined uncertainty on the mass accretion rate introduced by the determination of stellar parameters, bolometric corrections, geometry of the system, and the exclusion of emission lines is found to be ~ 0.6 dex. The authors acknowledge that the works of Johns-Krull & Basri (1997); Batalha et al. (2002); Scholz & Jayawardhana (2006); Bouvier et al. (2007) found intrinsic variability in the veiling measurements of young stars, and therefore accretion rates, of ~ 0.2 dex. In Alcalá et al. (2017), the authors compare estimates of $L_{\rm acc}$ found through two methods: utilizing the $L_{\rm acc} - L_{\rm line}$ empirical relationship from Alcalá et al. (2014) and fitting the spectra with a slab model of the Hydrogen emission. Their results determined the values of $L_{\rm acc}$ were similar within ~ 0.25 dex. Therefore, they found an uncertainty in $\dot{M}_{\rm acc}$ of ~ 0.42 dex. Therefore, the spread in these values reported by Herczeg & Hillenbrand (2008) and Alcalá et al. (2017) are such that they are not different enough (within the uncertainties) to prove intrinsic variability over the timescale of years. However, much of these uncertainties are systematic and can be mitigated by comparing the relative values of $\dot{M}_{\rm acc}$ of a single star over a shorter timescale. In this study the $\dot{M}_{\rm acc}$ of RU Lup is studied during 2011 and how it changes over the shorter timescale of two weeks. By investigating its short-time stellar-disk magnetospheric interaction, this dataset allows the exploration of how RU Lup's accretion fits into the category of "Routine Variability", as delineated in Table 1. of Fischer et al. (2022).

Additionally, multiple studies have inferred that RU Lup has a near face-on geometry from varying methods including the analysis of line profiles and measured rotational velocities (see Section 2 of Herczeg et al., 2005, and references therein) or the direct measurement of the inner dusty disk geometry and size with NIR interferometry (Gravity Collaboration et al., 2021). Because it is seen mostly face-on, RU Lup is an excellent candidate for a study of accretion variability as there are less geometrical effects to confound the observations (such as stellar rotation and extinction from the disk). It is also a well-studied and interesting object undergoing strong accretion activity. Stellar properties of RU Lup such as its radius ($R_\star$), spectral type (SpT), stellar luminosity ($L_\star$), rotational period ($P_{\rm rot}$), $v \sin i$ and visual extinction (A_V) can be found in Table 4.1.

4.2 Observations and data reduction

4.2.1 Spectroscopy

High-resolution ($R \sim 68,000$, corresponding to $\sim 4.4\,{\rm km\,s^{-1}}$) optical spectroscopic data were obtained with CFHT/ESPaDOnS across 12 epochs from 08 June 2011 to 23 June

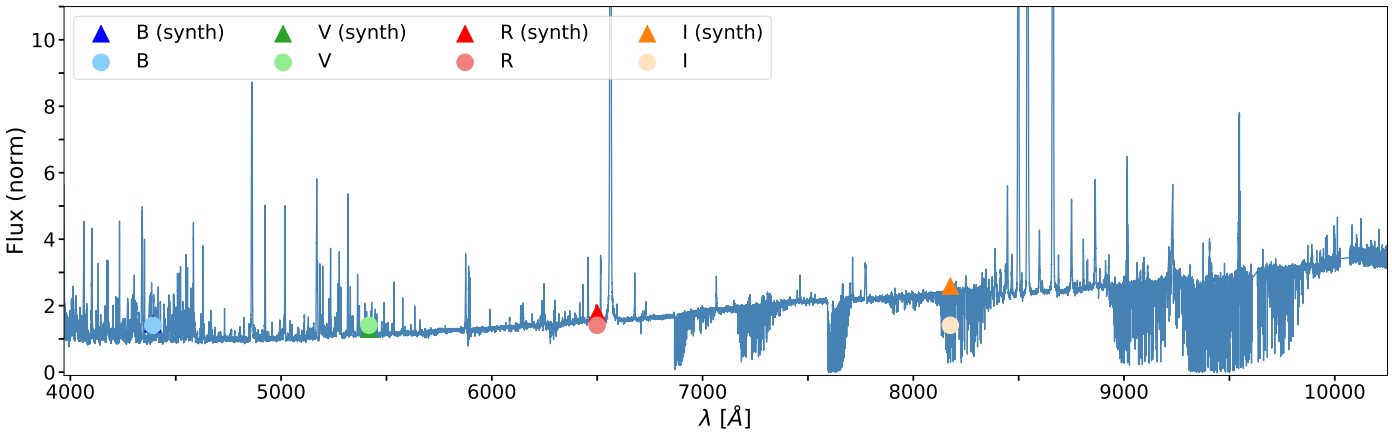

Figure 4.1: ESPaDOnS optical spectrum of RU Lup on the night of 17 June 2011. This spectrum is overlaid with the photometry measured from the ANDICAM observations of the same night. The circles represent the aperture photometry taken in the B, V, R and I bands and the triangles represent the synthetic photometry calculated by convolving the spectrum with the transmission response of ANDICAM in each band. For the B and V bands the triangles and circles are overlapping.

2011 (proposal ID: 11AP12, PI: Jean-Francois Donati). Details about the ESPaDOnS instrument can be found in Section 2.2. The ESPaDOnS data were reduced with "Upena," the standard pipeline provided by the CFHT, based on the Libre-ESpRIT package (Donati et al., 1997), outputting multiple, simultaneous sections of spectra (orders) that needed to be joined together to produce the full optical spectrum.

Additionally, because no standard star observation was available, the telluric lines in the regions of interest to this study were fitted and removed manually. This included the region in and around the [O I] 6300 Å line, i.e. the stronger component of the doublet that also includes [O I] 6364 Å, containing strong telluric contamination. This was done by first identifying known telluric lines in the wavelength region by comparing the target spectra with a telluric spectral atlas (Catanzaro, 1997). Next, the continuum in this region was fit and subtracted, and then, utilising libraries such as Astropy in Python, each identified telluric absorption that was blended with the [O I] 6300 Å line emission was fitted with a Gaussian. These Gaussian fits were then subtracted from each night's spectrum. These telluric absorption lines were identified by their extremely narrow characteristic profiles and by consulting high resolution spectra of the Earth's atmospheric telluric features[1].

In addition to telluric contamination, the data contain many photospheric absorption lines, typical of a K7 star. Some of these were blended with the [O I] 6300 Å line and required removal to study its profile. Unlike the telluric absorption lines, it was

[1]These atmospheric spectra can be found at the ESO science site: https://www.eso.org/sci

possible to remove all the photospheric lines in this region (6284 − 6342 Å) at once. This was done by obtaining a WTTS spectrum of the same spectral type as a template, which contains the same photospheric lines but no emission lines (Martín, 1998), and subtracting this from the CTTS spectrum of RU Lup. As WTTSs undergo little-to-no accretion activity (which produces many emission lines), their spectra can be used as templates for the photosphere of CTTSs of the same spectral type. Indeed, the RU Lup spectra was compared with the WTTS spectrum of TAP 45 (same spectral type and similar $v \sin i = 7.7 \pm 0.7\,\mathrm{km\,s^{-1}}$; Nguyen et al., 2012). TAP 45 has a stellar mass of $\sim 0.79\,M_{\odot}$, a radius of $\sim 1.14\,R_{\odot}$ and $T_{\rm eff} \sim$ 4040 K (Grankin, 2013). This template was then re-scaled such that it met the level of the RU Lup continuum; these parameters were adjusted by minimising a χ^2 fit. The resultant broadened and veiled template represents a spectrum containing the fitted photospheric features which can then be used to subtract the contaminating photospheric lines from the regions of interest. This process was completed on a night-by-night basis.

Finally, the radial velocities of the observed lines were calculated using single or multiple Gaussian fits (the detected lines typically show multiple components). These velocities are measured with respect to the systematic velocity of the star ($v = +8 \pm 2\,\mathrm{km\,s^{-1}}$, Takami et al., 2001) in the local standard of rest (LSR) frame. It is important in this analysis to note that deconvolving spectral lines into multiple components can potentially result in degeneracy of the fits, especially when there is noise. To combat this, a goodness of fit was assessed via the reduced χ^2 statistic for each individual line fitted. Additionally, the multiple components found to form the spectral line were only included in the study when there existed a potential physical explanation for that component in the literature.

4.2.2 Photometry and spectroscopic flux calibration

As the ESPaDOnS observations were not flux calibrated, archival data of simultaneous photometry was found of RU Lup from the 1.3 m SMARTS/CTIO[1] telescope for the night of 17 June 2011.

These ANDICAM photometric data were taken on 17 June 2011, allowing the ESPaDOnS spectra from the same night to be flux calibrated. The data from the B, V, R and I filters were reduced in Python using the "Astropy" and "ccdproc" packages to apply biases, darks and flat-fielding (dome flats for V, R and I filters and sky flats for

[1]SMARTS, the Small and Medium Aperture Research Telescope Facility, is a consortium of universities and research institutions that operate the small telescopes at Cerro Tololo under contract with AURA.

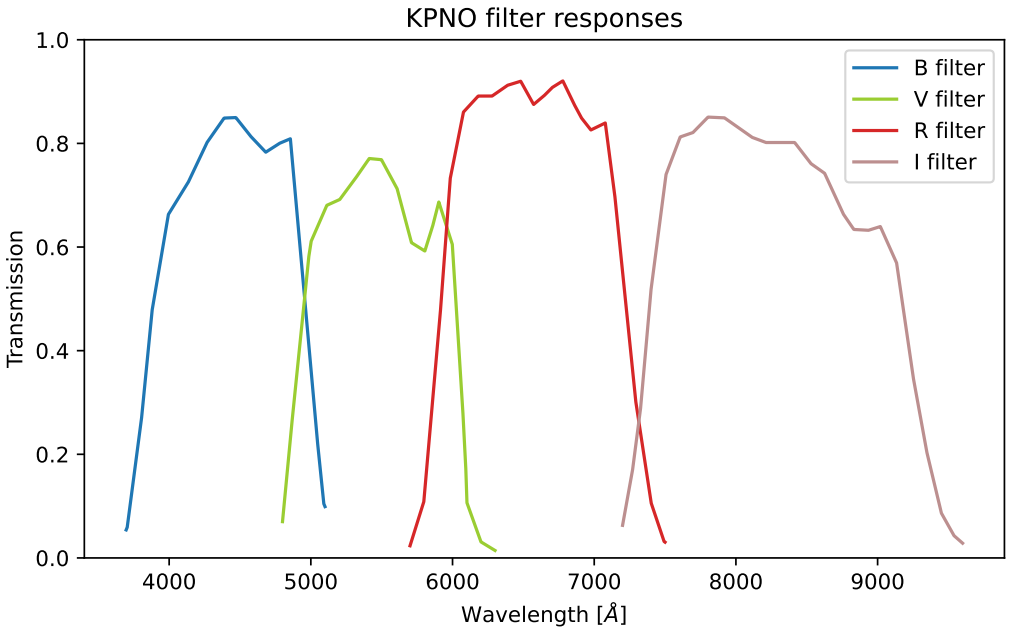

Figure 4.2: The transmission curves of the KPNO filters used on the ANDICAM instrument. These are convolved with the observations in order to produce the synthetic photometry.

the B filter) to the raw images of RU Lup and the standard stars observed from the same night. The resulting standard stars were flux calibrated using the zero-point fluxes given for the Kitt Peak National Observatory (KPNO) filters used on ANDICAM, and were then used to flux calibrate the science images. The calibrated spectrum of the June 17, 2011 night is shown in Fig. 4.1, together with the photometric data.

No photometric data are available for the other nights. Therefore, the [S II] 6730 Å emission line was examined and found to have extremely similar profiles from night-to-night, and very small night-to-night flux variations. The profiles of this line show the typical features of forbidden lines in CTTSs, namely a high- and a low-velocity component (HVC and LVC, respectively) wherein the HVC is not expected to show any variability on these short timescales (see Section 4.3.4) (Hartigan et al., 1995; Rigliaco et al., 2013; Simon et al., 2016; McGinnis et al., 2018). Taking the flux calibrated [S II] 6730 Å HVC (the 17 June epoch) as a reference (the [O I] 6300 Å line can also be used, but is less straightforward to analyse because it is in a region of telluric contamination), each epoch was re-scaled by the amount that was necessary to match the flux of its HVC with the flux calibrated one.

The lack of temporal variability seen in the resultant [O I] 6300 Å line spectra (Fig. 4.3, left panel) confirms that this re-scaling is a valid calibration, as the [O I] 6300 Å line's HVC is not expected to vary over these timescales either. I estimate that the uncertainty

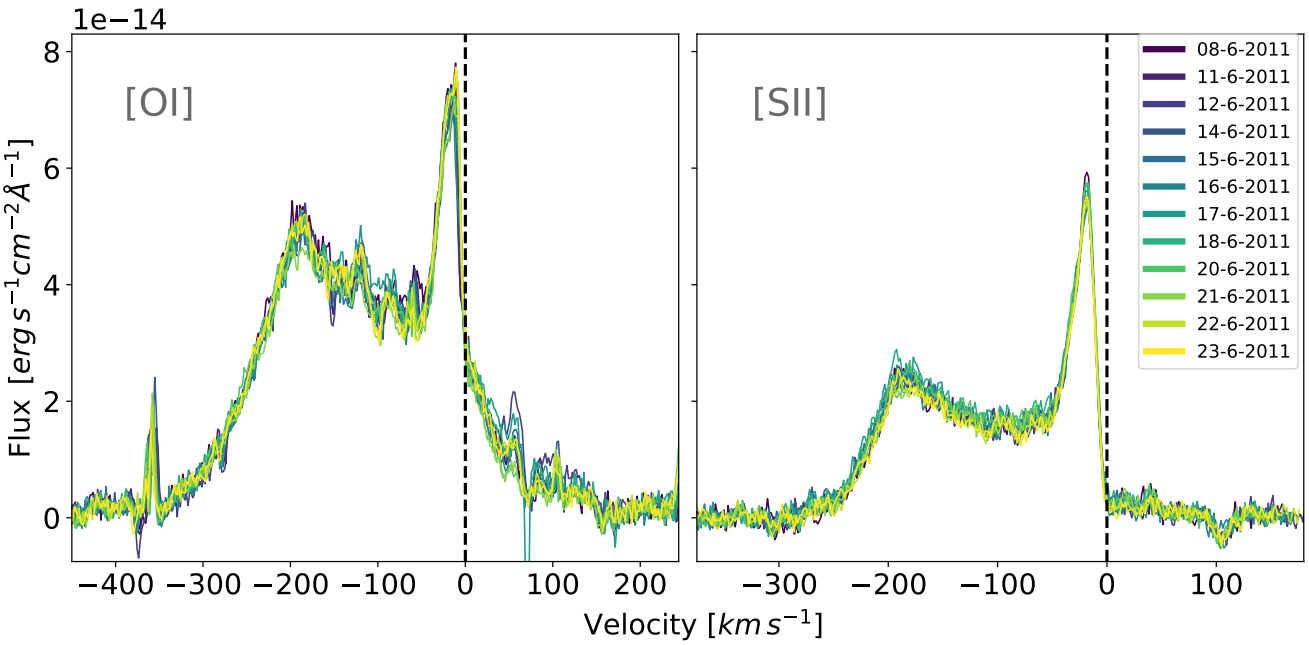

Figure 4.3: The outflow-tracing lines of [O I] 6300 Å and [S II] 6730 Å over the 12 epochs of ESPaDOnS observations spanning from 08 June 2011 to 23 June 2011. These spectra are continuum-subtracted and flux calibrated. The features at $\sim -370\,\mathrm{km\,s^{-1}}$ and $\sim +80\,\mathrm{km\,s^{-1}}$ are residuals from the telluric removal.

of the calibrated flux is of the order of 5%.

In the specific case of RU Lup, this choice is also supported by the results of Gahm et al. (2013), which found that the forbidden line profiles remained remarkably constant over their study's longer timescale of five years. The authors also note that in their flux calibrated spectra, the flux of the [S II] 6730 Å line remains stable for relatively moderate veiling ($r \leq 2$; see Figure 2 in Gahm et al., 2008). Indeed, this is the case in this data set (see Section 4.3.3).

My assumptions separately work on both [O I] 6300 Å and [S II] 6730 Å line flux calibration. These calibrated spectra are presented in Fig. 4.4, where the main lines used in this paper are labelled. The [S II] 6730 Å emission line is the stronger component of the S II doublet that also includes [S II] 6716 Å.

4.3 Results

These multi-epoch calibrated spectra are presented in Fig. 4.4. The spectra, from the B to the R band, show variations in the continuum flux. Many photospheric lines in absorption are present, indicative of a K7 star (White & Basri, 2003). Among them, the

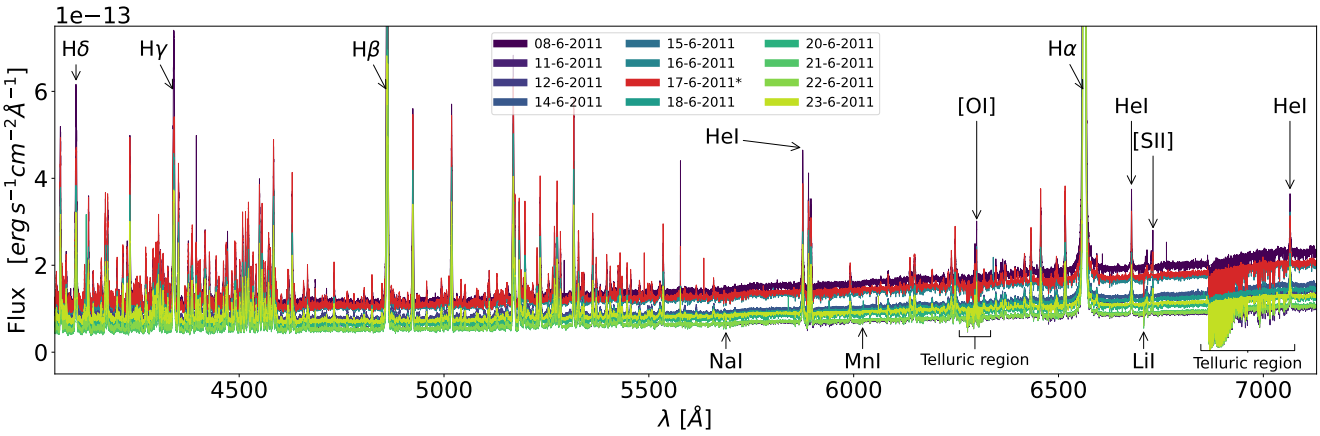

* simultaneous with ANDICAM photometry

Figure 4.4: The flux calibrated spectra from the 12 epochs taken with ESPaDOnS across the optical regime (4000 − 7100 Å). Notable emission and absorption lines discussed in this study are identified with their species name. Regions highly contaminated by telluric emission are also indicated. The spectrum in black (17-06-2011) represents the night of observations that was calibrated with simultaneous photometry. The other 11 nights were flux calibrated as described in Section 4.2.2.

Li I 6707 Å transition is the most prominent. Additionally, an overwhelming number of emission lines are detected, typically originating from the circumstellar environment of RU Lup such as accretion shocks, winds, jet and chromosphere. For the purposes of this paper, lines that are widely used to trace accretion and ejection activity in CTTSs are selected.

4.3.1 Accretion-tracing lines

As previously mentioned, the accretion activity in young stars such as RU Lup produces line emission that allows the study of these processes. There are many known accretion-tracing emission lines at optical wavelengths, and their intensities, profiles, and relative red- and blue-shifts provide information about their origins.

The brightest accretion-tracing lines present in the data are H I (Hα, Hβ, Hγ and Hδ) and He I (5875 Å, 6678 Å, and 7065 Å). Equivalent widths and integrated fluxes are shown in Tables 4.2 and 4.3, respectively. Both line profiles and intensities vary with species and (most noticeably in the case of H I) from night to night (see Figure 4.5). In the following the variation of the line luminosity will be concentrated on.

As seen in the left-hand column of Fig. 4.5, the Balmer lines vary significantly over the short timescale of two weeks covered by the ESPaDOnS data. Between the dimmest and brightest nights, there is an increase in integrated flux by a factor of ∼1.7 for Hα,

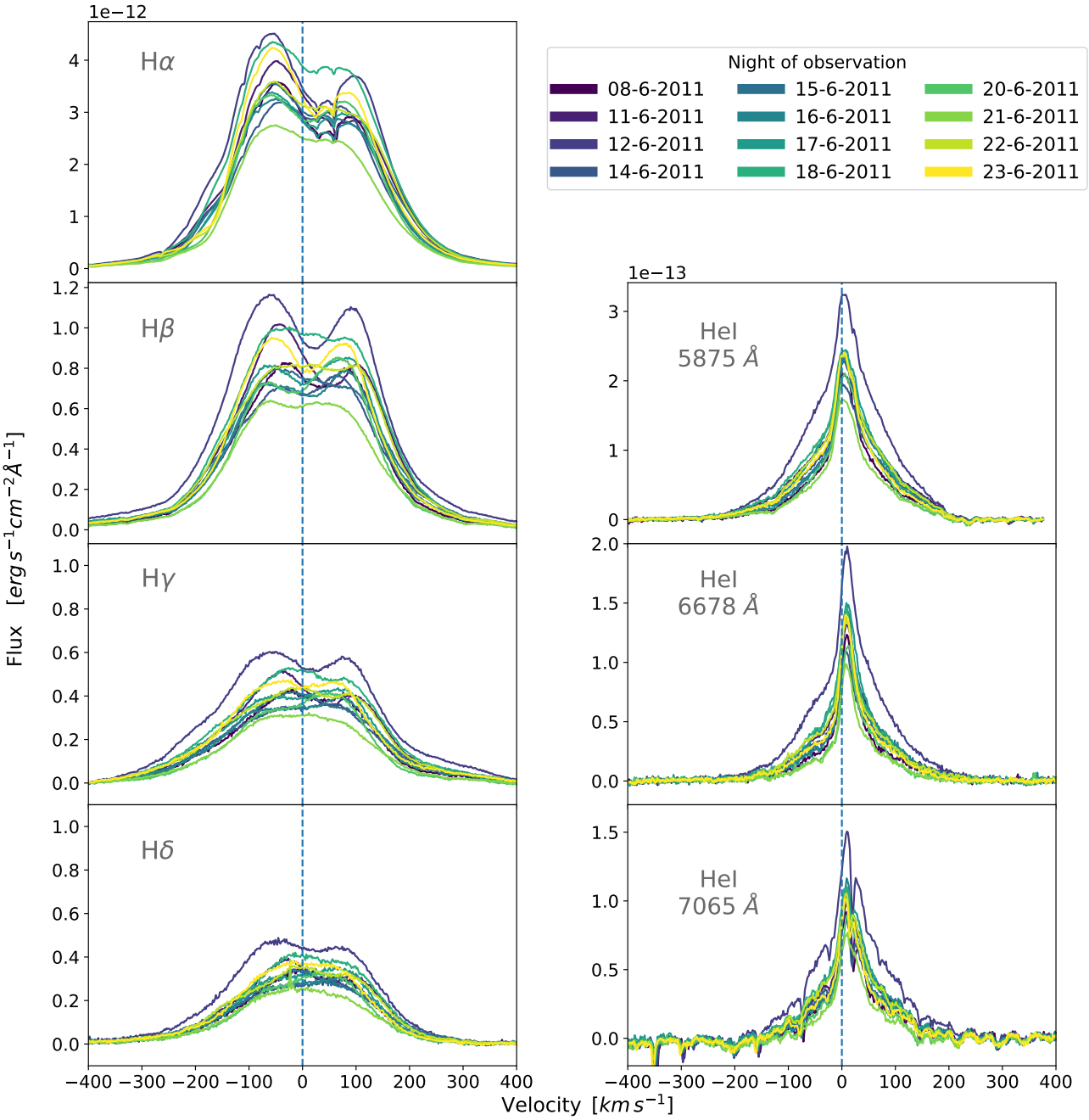

Figure 4.5: The accretion-tracing lines of H I and He I over the 12 epochs of ESPaDOnS observations spanning from 08 June 2011 to 23 June 2011. These spectra are continuum-subtracted and flux calibrated. They illustrate a night-to-night variability in the line emission from RU Lup.

$\sim$1.9 for Hβ, $\sim$2.2 for Hγ and $\sim$2.0 for Hδ.

The right-hand column of Fig. 4.5 shows the He I emission lines at 5875 Å, 6678 Å and 7065 Å. The trend in flux variability seen here is similar to that for the Balmer series. There is an increase in the integrated intensity between the dimmest and brightest nights by a factor of $\sim$ 1.9 for He I 5875 Å and $\sim$ 2 for He I 6678 Å and He I 7065 Å.

As has been shown by Beristain et al. (2001), the He I 5875 Å line can be decomposed into a narrow component (NC) and a broad component (BC). The NC is generally slightly red-shifted and is believed to originate in the post-shock region near the stellar surface. The BC has been theorised to have multiple origins, with contributions from the accretion columns as well as from a hot wind. The He I 5875 Å and He I 6678 Å lines have been decomposed into two components in Figs. 4.6 and 4.7. Though the components vary from night to night, both profiles indeed show a clear NC and BC every night. The flux of each component varies with a similar trend, indicating that the processes that give rise to both components correlate well with each other, and therefore with accretion.

4.3.2 Time-dependent accretion luminosity & mass accretion rate

The $L_{\rm acc}$ from the luminosity of the accretion-tracing lines was derived using the well established relations between each line luminosity ($L_{\rm line}$) and $L_{\rm acc}$ derived in Alcalá et al. (2017) for CTTSs. $L_{\rm acc}$ is then computed for each night from the average of the $L_{\rm acc}$ values derived from the individual lines (see Fig. 4.8). Note that, because of the way the $L_{\rm line}$ *vs.* $L_{\rm acc}$ relation was derived in Alcalá et al. (2017), $L_{\rm acc}$ refers to the continuum excess emission only.

The inferred $L_{\rm acc}$ values found in the He I differ slightly from those of the H I lines. This is likely due to the complexity of processes that the He I lines are tracing, which include accretion, but not exclusively. In particular there can be a strong wind emission (Beristain et al., 2001; Johns-Krull & Basri, 2001; McGinnis et al., 2020). Therefore only the H I emission lines have been used to estimate $L_{\rm acc}$.

The calculated values for $L_{\rm acc}$ range from 0.35 to 0.72 $L_\odot$ over the course of 15 days, with an average of 0.5 $L_\odot$ (see Table 4.4). It is worth noting that the observed variability in the accretion luminosity is real, as the line flux variation of the different H I lines is much larger than their flux uncertainties (see Tables 4.2 and 4.3).

Variations in $L_{\rm acc}$ can in principle be due to variations in extinction. However, there is no evidence in the literature of significant variations in visual extinction which is always very small (e.g. Herczeg et al., 2005; Alcalá et al., 2017) and consistent with this

Date	$F_{H\alpha}$	$EW_{H\alpha}$	$F_{H\beta}$	$EW_{H\beta}$
yyyy-mm-dd	$\times 10^{-12}$ [erg s^{-1} cm^{-2}]	[Å]	$\times 10^{-12}$ [erg s^{-1} cm^{-2}]	[Å]
2011-06-08	22.96 ± 0.02	-142.22 ± 0.03	4.25 ± 0.04	-56.69 ± 0.04
2011-06-11	25.45 ± 0.01	-131.85 ± 0.03	5.07 ± 0.07	-55.55 ± 0.04
2011-06-12	30.35 ± 0.02	-119.31 ± 0.03	6.53 ± 0.02	-51.85 ± 0.05
2011-06-14	22.50 ± 0.01	-133.94 ± 0.03	4.19 ± 0.05	-58.15 ± 0.04
2011-06-15	24.10 ± 0.01	-125.81 ± 0.03	4.44 ± 0.05	-48.78 ± 0.04
2011-06-16	21.96 ± 0.01	-117.41 ± 0.03	4.19 ± 0.05	-44.08 ± 0.04
2011-06-17	23.03 ± 0.01	-111.94 ± 0.03	4.66 ± 0.10	-47.94 ± 0.05
2011-06-18	30.12 ± 0.01	-149.78 ± 0.03	5.58 ± 0.08	-66.94 ± 0.04
2011-06-20	22.44 ± 0.01	-134.46 ± 0.03	4.00 ± 0.02	-47.61 ± 0.04
2011-06-21	18.34 ± 0.01	-114.83 ± 0.03	3.44 ± 0.03	-46.26 ± 0.04
2011-06-22	24.61 ± 0.01	-125.28 ± 0.03	4.86 ± 0.07	-53.06 ± 0.04
2011-06-23	25.92 ± 0.01	-127.09 ± 0.03	4.91 ± 0.06	-47.69 ± 0.04
Date	$F_{H\gamma}$	$EW_{H\gamma}$	$F_{H\delta}$	$EW_{H\delta}$
yyyy-mm-dd	$\times 10^{-12}$ [erg s^{-1} cm^{-2}]	[Å]	$\times 10^{-12}$ [erg s^{-1} cm^{-2}]	[Å]
2011-06-08	1.89 ± 0.05	-23.21 ± 0.04	1.31 ± 0.02	-16.70 ± 0.02
2011-06-11	2.29 ± 0.04	-23.31 ± 0.04	1.52 ± 0.01	-14.91 ± 0.02
2011-06-12	3.18 ± 0.05	-23.26 ± 0.04	2.11 ± 0.02	-12.99 ± 0.02
2011-06-14	1.82 ± 0.05	-22.77 ± 0.04	1.29 ± 0.02	-17.25 ± 0.02
2011-06-15	2.00 ± 0.03	-21.38 ± 0.04	1.36 ± 0.01	-13.64 ± 0.03
2011-06-16	1.85 ± 0.05	-18.08 ± 0.04	1.28 ± 0.02	-12.27 ± 0.02
2011-06-17	2.13 ± 0.05	-20.23 ± 0.04	1.41 ± 0.02	-12.25 ± 0.02
2011-06-18	2.57 ± 0.04	-30.81 ± 0.04	1.67 ± 0.02	-17.89 ± 0.02
2011-06-20	1.65 ± 0.06	-17.77 ± 0.04	1.18 ± 0.02	-13.47 ± 0.02
2011-06-21	1.47 ± 0.05	-18.60 ± 0.04	1.04 ± 0.01	-14.13 ± 0.02
2011-06-22	2.21 ± 0.04	-22.73 ± 0.04	1.50 ± 0.01	-14.58 ± 0.02
2011-06-23	2.28 ± 0.04	-21.88 ± 0.04	1.49 ± 0.01	-12.89 ± 0.02

Table 4.2: Integrated fluxes and equivalent widths of the H I lines and their associated errors.

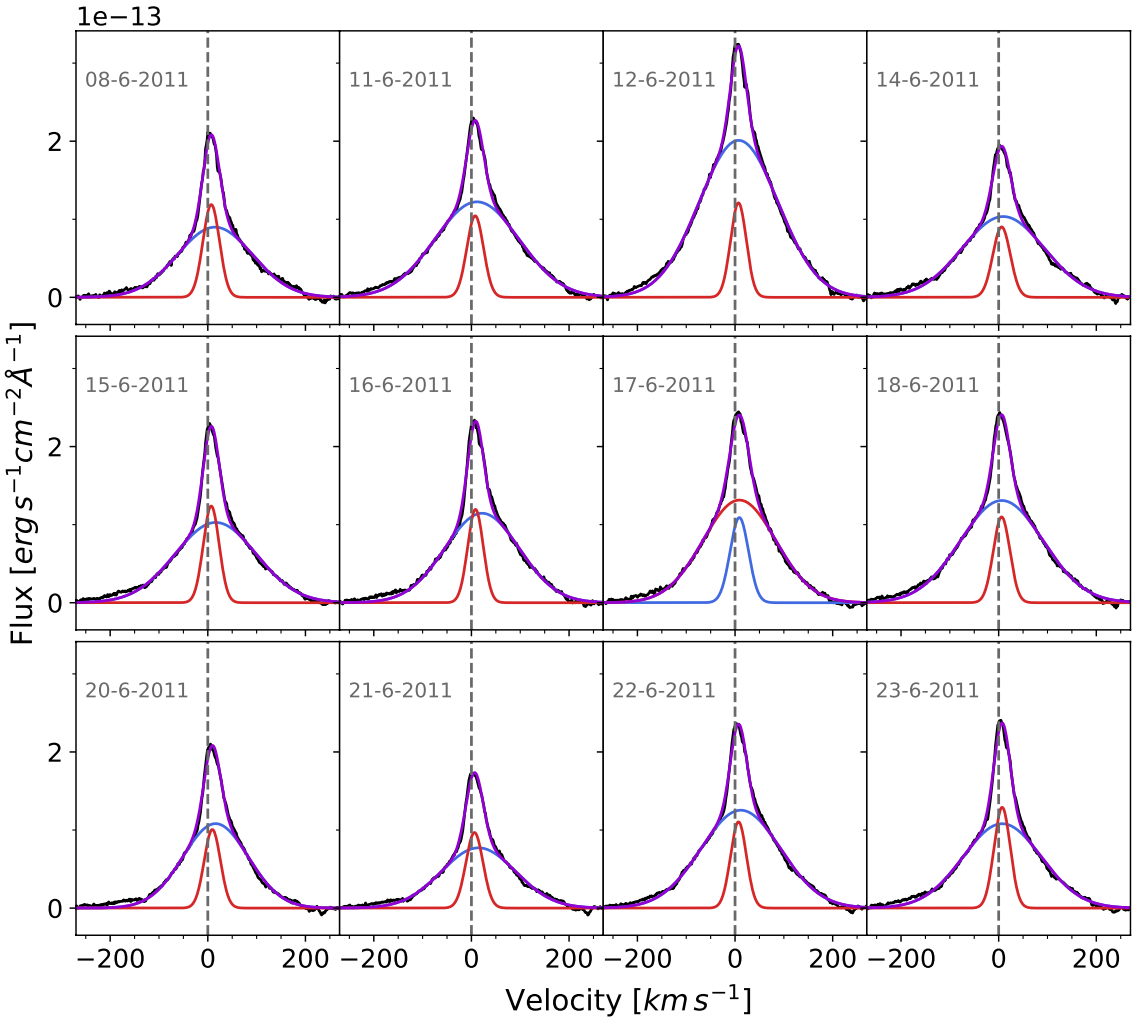

Figure 4.6: The Gaussian decompositions of the He I 5875 Å emission lines for each night of observations. The spectra are continuum-subtracted and flux calibrated. The black line is the RU Lup spectra, the red represents the narrow component (NC), the blue represents the broad component (BC) and the purple represents the convolution of the two components.

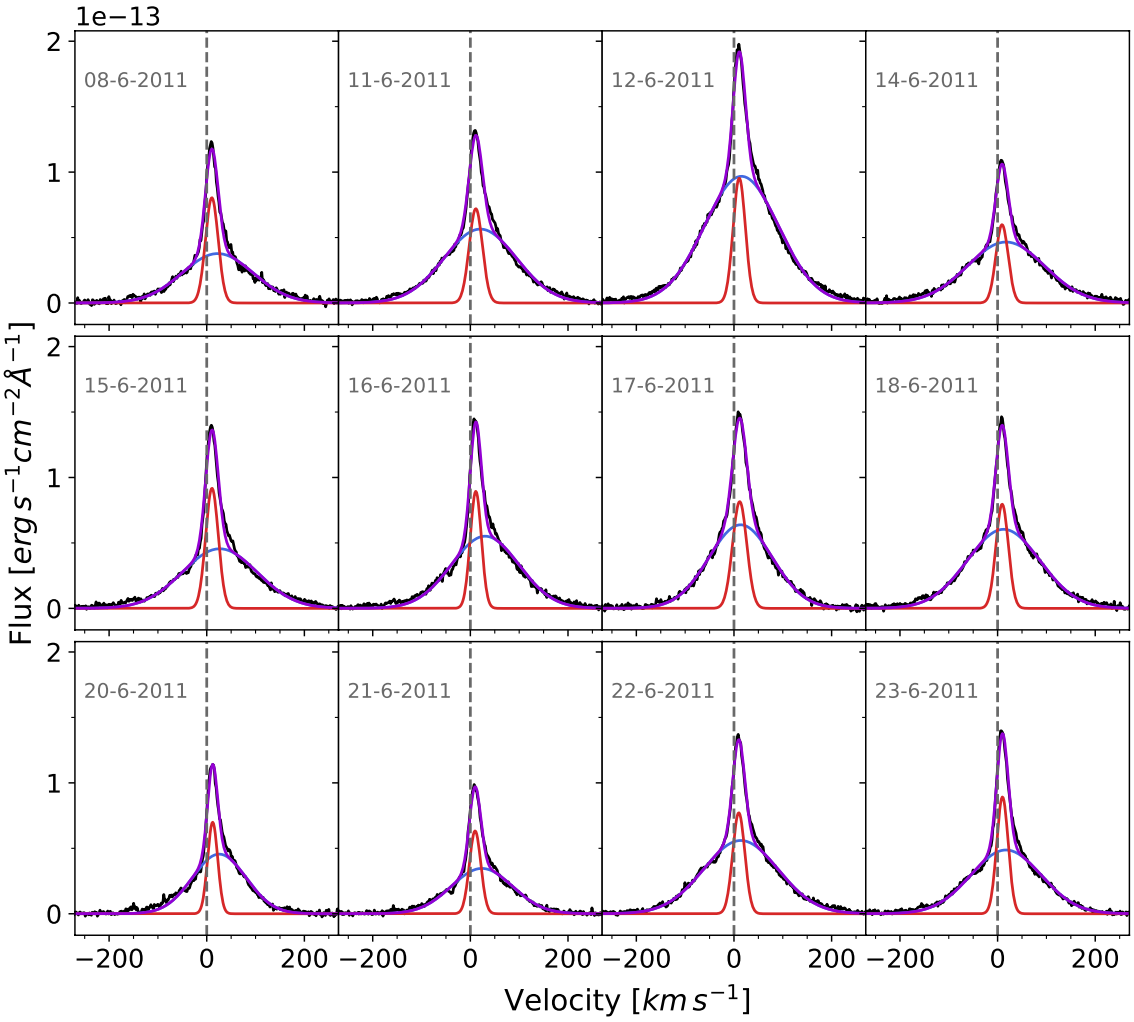

Figure 4.7: The Gaussian decompositions of the He I 6678 Å emission lines for each night of observations. The spectra are continuum-subtracted and flux calibrated. The black lines is the RU Lup spectra, the red represents the narrow component (NC), the blue represents the broad component (BC) and the purple represents the convolution of the two components.

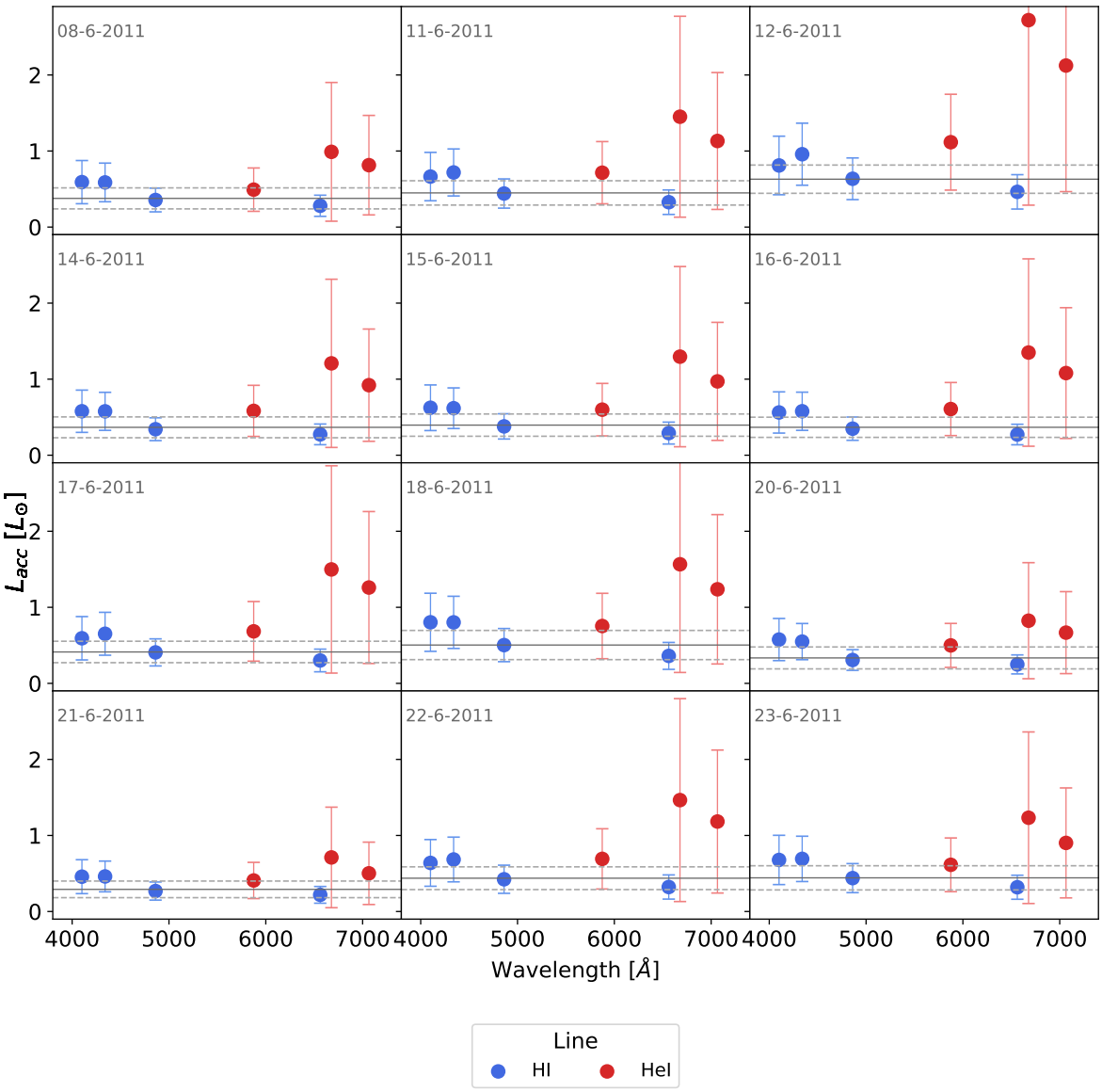

Figure 4.8: Plots searching for any possible wavelength dependence of the estimate of $L_{\rm acc}$ for each of the 12 epochs. None is found. The horizontal line represents the $L_{\rm acc}$ used as a result, which has been derived from an average of only the H I 's values for $L_{\rm acc}$ (blue dots). The He I (red dots) lines are also shown.

Date	$F_{\mathrm{He\,I\ 5875}}$	$EW_{\mathrm{He\,I\ 5875}}$	$F_{\mathrm{He\,I\ 6678}}$	$EW_{\mathrm{He\,I\ 6678}}$
yyyy-mm-dd	$\times 10^{-13}$ [erg s^{-1} cm^{-2}]	[Å]	$\times 10^{-13}$ [erg s^{-1} cm^{-2}]	[Å]
2011-06-08	4.41 ± 0.01	-4.05 ± 0.01	2.18 ± 0.06	-1.65 ± 0.02
2011-06-11	6.10 ± 0.04	-4.76 ± 0.02	2.97 ± 0.05	-1.91 ± 0.02
2011-06-12	8.98 ± 0.06	-5.05 ± 0.02	4.91 ± 0.06	-2.38 ± 0.02
2011-06-14	5.10 ± 0.03	-4.45 ± 0.02	2.56 ± 0.06	-1.84 ± 0.03
2011-06-15	5.23 ± 0.03	-4.06 ± 0.02	2.71 ± 0.05	-1.76 ± 0.02
2011-06-16	5.29 ± 0.04	-4.01 ± 0.02	2.80 ± 0.06	-1.79 ± 0.02
2011-06-17	5.86 ± 0.04	-4.14 ± 0.02	3.04 ± 0.05	-1.79 ± 0.02
2011-06-18	6.38 ± 0.04	-5.06 ± 0.02	3.15 ± 0.06	-1.99 ± 0.02
2011-06-20	4.46 ± 0.01	-3.86 ± 0.01	1.89 ± 0.05	-1.36 ± 0.02
2011-06-21	3.75 ± 0.01	-3.43 ± 0.02	1.68 ± 0.04	-1.25 ± 0.02
2011-06-22	5.93 ± 0.03	-4.46 ± 0.02	2.99 ± 0.05	-1.88 ± 0.02
2011-06-23	5.34 ± 0.04	-3.78 ± 0.02	2.60 ± 0.04	-1.56 ± 0.02

Table 4.3: Integrated fluxes and equivalent widths of He I 5875 Å and He I 6678 Å and their associated errors.

system being oriented face-on. Moreover, Fig. 4.8 shows there is no trend of increasing L_{acc} from lines of increasing wavelength. Therefore, it is assumed in the following that changes in L_{acc} trace physical changes in the accretion rate.

Because this variability cannot be caused by changes in extinction, it must come from accretion variability. The derived range of L_{acc} values is in line with those found in the literature, derived with different methods (e. g. slab modelling of the Balmer jump, luminosity of H I lines, UV excess), namely $\sim 0.5\,L_{\odot}$ (Herczeg et al., 2005; Antoniucci et al., 2014; Alcalá et al., 2017).

The corresponding value of the mass accretion rate is computed as in Eq. 1.13. The $\dot{M}_{\mathrm{acc}}$ ranges from a minimum of $\sim 3 \times 10^{-8} M_{\odot}\,\mathrm{yr}^{-1}$ to a maximum of $\sim 7 \times 10^{-8} M_{\odot}\,\mathrm{yr}^{-1}$. When averaged across the 15 nights, the result is $\dot{M}_{\mathrm{acc}} = 4.8 \times 10^{-8} M_{\odot}\,\mathrm{yr}^{-1}$, in line with the values found in the literature. Small differences are due to slightly different distances ($140 - 160$ pc) and masses ($0.5 - 1.1\,M_{\odot}$) adopted for RU Lup by different authors. This kind of variability aligns with what Fischer et al. (2022, Table 1) characterise as "Routine Variability" wherein there are day-to-day changes of $< 1 - 2$ mag in the optical and IR. This variability in CTTSs is described in Fischer et al. (2022) as a result of rotational, magnetospheric or inner-disc interactions with the star. In this study, the impact stellar rotation has (or does not have) on RU Lup's variability is discussed in Section 4.4.1.

It is important to stress here that absolute values of $\dot{M}_{\mathrm{acc}}$ depend on the stellar parameters adopted, chosen accretion tracers measured, and the adopted size of the star's magnetosphere (which will alter what truncation radius is used in the calculation).

Date yyyy-mm-dd	$\log L_{\rm acc}$ $[L_\odot]$	$\pm\sigma$ (spread)	$\log \dot{M}_{\rm acc}$ $[M_\odot\,{\rm yr}^{-1}]$	$r_{\rm Na\,I}$	$r_{\rm Mn\,I}$	$r_{\rm Li\,I,\,obs}$	$r_{\rm Li\,I}$ *	χ^2
2011-06-08	−0.35	0.13	−7.36	2.66 ± 0.44	2.23 ± 0.46	1.11	2.91 ± 0.24	8.7
2011-06-11	−0.27	0.13	−7.28	2.98 ± 0.55	3.56 ± 0.35	1.56	3.36 ± 0.20	4.8
2011-06-12	−0.14	0.11	−7.16	4.61 ± 1.06	**	2.51	4.31 ± 0.19	2.5
2011-06-14	−0.36	0.13	−7.37	2.21 ± 0.32	2.08 ± 0.42	1.04	2.84 ± 0.23	7.6
2011-06-15	−0.32	0.13	−7.34	3.53 ± 0.72	4.55 ± 1.39	1.48	3.28 ± 0.16	5.2
2011-06-16	−0.36	0.13	−7.38	3.94 ± 0.86	3.07 ± 0.73	1.50	3.30 ± 0.17	4.3
2011-06-17	−0.31	0.13	−7.33	3.90 ± 0.79	4.96 ± 1.63	1.79	3.59 ± 0.22	5.9
2011-06-18	−0.21	0.14	−7.23	3.20 ± 0.58	2.81 ± 0.61	1.37	3.17 ± 0.20	5.8
2011-06-20	−0.38	0.15	−7.40	2.86 ± 0.48	2.43 ± 0.51	1.06	2.86 ± 0.18	6.4
2011-06-21	−0.46	0.14	−7.47	2.45 ± 0.39	2.07 ± 0.18	0.93	2.73 ± 0.20	8.5
2011-06-22	−0.28	0.13	−7.30	3.11 ± 0.54	3.10 ± 0.75	1.33	3.13 ± 0.15	5.0
2011-06-23	−0.28	0.13	−7.29	3.84 ± 0.81	5.35 ± 0.30	1.71	3.51 ± 0.24	4.3

* $r_{\rm Li\,I}$ = $r_{\rm Li\,I}$ (obs) + $\Delta r_{\rm abund.\,corr.}$, where $\Delta\, r_{\rm abund.\,corr.} = 1.8$, see Section 4.4.3

** signal-to-noise ratio (SNR) insufficient to measure veiling

Table 4.4: The $L_{\rm acc}$, $\dot{M}_{\rm acc}$ and veiling for each epoch. The $L_{\rm acc}$ and $\dot{M}_{\rm acc}$ for each night are determined by averaging the values found from the H I lines, and their uncertainties are estimated from their spread. Columns 5 and 6 contain the veiling measurements for the photospheric lines, Na I 5688 Å and Mn I 6021 Å. The observed veiling measured in the Li I 6707 Å photospheric line is given in column 7 ($r_{\rm Li\,I}$ (obs)) and the abundance corrected veiling is given in column 8 ($r_{\rm Li\,I}$ = $r_{\rm Li\,I}$ (obs) + $\Delta r_{\rm abund.\,corr.}$). The final column contains the χ^2 values of the fits done to calculate the veiling in the Li I 6707 Å absorption line.

However, the relative time variations of $\dot{M}_{\rm acc}$, and those of $L_{\rm acc}$, do not depend on these parameters.

4.3.3 Time-dependent veiling from metal lines

Additional information on the accretion variability of RU Lup can be obtained by measuring the excess emission in photospheric lines (veiling), as described in Eq. 4.1. The excess emission in a given line is the sum of the continuum emission from the accretion shock at the line wavelength and of the emission of the same line in accreting matter (Hartigan et al., 1989). By measuring the amount of veiling in a CTTS, it is possible to quantify the amount of accretion activity occurring in the star during a given observation.

In Hartigan et al. (1989), a quantitative method was developed to measure the amount of veiling present in a given CTTS. By comparing the spectrum of the accreting CTTS, with a template spectrum that represents only the photosphere (no accretion present), the dimensionless quantity, veiling, is produced:

$$r_j = \frac{F_{excess}}{F_{photo}}, \tag{4.1}$$

where r_j is the veiling in a specific wavelength interval j, F_{excess} is the excess flux (due to accretion activity) and F_{photo} is the photospheric flux, given from the template star. WTTSs are often used for this purpose (e.g. Hartigan et al., 1991; Valenti et al., 1993; Johns-Krull et al., 1999; Dodin & Lamzin, 2012; McGinnis et al., 2018).

The veiling present in a specific photospheric line can be similarly derived using the equivalent widths (EWs) of that line in the CTTS spectrum and the WTTS spectrum:

$$r_j = \frac{EW_{photo}}{EW_{observed}} - 1, \tag{4.2}$$

where $\mathrm{EW}_{observed}$ is the equivalent width of the observed line in the CTTS spectrum and EW_{photo} is the equivalent width of the same line in the template (WTTS) spectrum. Notably, the numerator in Eq. 4.2 represents the total flux observed (the sum of the photospheric and excess fluxes), whereas the numerator in Eq. 4.1 represents only the excess flux.

Veiling, being the ratio of the excess flux over the photospheric flux, does not depend on extinction. Although it is not the case for RU Lup, this is very important, as the extinction is sometimes uncertain and it is known to vary with time in a large number of pre-main sequence stars (e. g. the dippers studied by Contreras Peña et al., 2017).

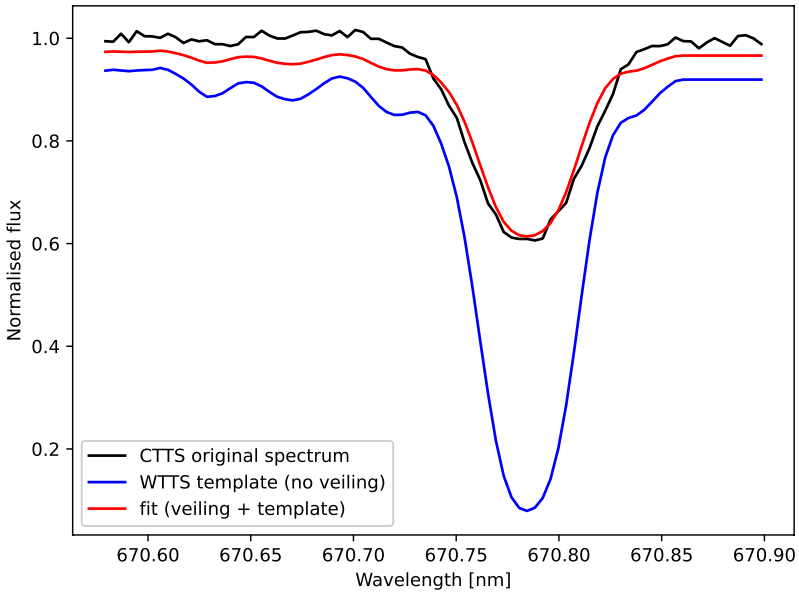

Figure 4.9: An example of fitting a photospheric (Li I 6707Å) line in one of the RU Lup spectra (21-06-2011) with the WTTS template from TAP 45 to estimate the veiling present in this region of the spectrum.

Photospheric lines of different species and properties may exhibit different veiling if accretion-related line-emission is important, as proposed, for example, by Dodin & Lamzin (2012).

This study aims to add to the conversation concerning the distinction between continuum veiling, that is, the contribution to the measurement of veiling due to a continuum excess, and the contribution of specific line emission. Therefore, veiling in the individual lines was investigated in a clean region of the spectra to attain the most accurate measurements possible. This allows me to delve deeper into how veiling from metal lines relates to the accretion luminosity.

Therefore, this analysis is focused on three intrinsically deep metal lines in the region $5600 - 6700$ Å, namely the Li I 6707Å, Mn I 6021Å and Na I 5688Å lines. The latter were chosen as they are within the wavelength range of interest and have a sufficiently high signal-to-noise ratio (SNR) for veiling measurements.

The Li I 6707 Å line seen in absorption in young K7 stars has the deepest absorption in the optical wavelength range. It has an average $\mathrm{EW}_{\mathrm{Li\,I}} = 0.17 \pm 0.03$ Å. This line was analysed by comparing it to a K7 WTTS and estimated the amount of veiling present as described in Section 4.2. An example of the fits is provided in Fig. 4.9, and in Section 1.2.3 the method for calculating veiling is explained in detail. Preliminary analysis of the observed veiling produced an average over the 15 nights of $r_{\mathrm{Li\,I\ avg}}(\mathrm{obs}) = 1.92 \pm 0.03$. This observed value is affected by there being different abundances of Li in

the template star and RU Lup, as discussed in Section 4.4.3. The abundance-corrected average is $r_{\mathrm{Li\,I\ avg}} = 3.25 \pm 0.20$, which is used throughout this study. The nightly results are shown in column 8 of Table 4.4.

Veiling measurements of the Na I 5688 Å and Mn I 6021 Å photospheric lines can be found in columns 5 and 6 of Table 4.4 and their averages over the 15 nights are $r_{\mathrm{Na\,I\ avg}} = 3.27 \pm 0.63$ and $r_{\mathrm{Mn\,I\ avg}} = 3.29 \pm 0.67$. As these photospheric lines do not have as high an SNR as that of the Li I 6707 Å, and are intrinsically weaker, there is higher uncertainty in the measured veiling.

The additional photospheric metal lines Ti I 6261.10 Å, Ca I 6431.10 Å and Ni I 6643.63 Å were initially considered as well, however these lines were too veiled to get accurate measurements. This illustrates the difficulty in measuring the veiling in high accretors as there is a balance wherein the veiling is high enough to be noticeable in the spectrum, but is not so high that the photospheric lines are completely "washed-out".

4.3.4 Wind & jet lines

In the studied spectral range, there are multiple forbidden emission lines associated with outflowing material from young stars (Edwards et al., 1987; Hamann, 1994; Hartigan et al., 1995). Present in these data with a strong SNR are the [O I] 6300 Å and [S II] 6730 Å emission lines. The flux calibrated spectra of these lines from the 12 epochs can be seen in Fig. 4.3. The vast majority of the emission from the [O I] 6300 Å line is blue-shifted and it is completely blue-shifted in the [S II] 6730 Å. Both lines have a very similar profile with wings reaching very high systematic velocities, namely ~ -300 and $\sim -380\,\mathrm{km\,s^{-1}}$ for the [S II] 6730 Å and the [O I] 6300 Å lines, respectively. These wing velocity values are slightly higher than those found for RU Lup in the observations of Fang et al. (2018) and Banzatti et al. (2019) in 2008 ($\sim -270\,\mathrm{km\,s^{-1}}$ for [O I] 6300 Å) and Whelan et al. (2021) in 2012 (~ -250 and $\sim -280\,\mathrm{km\,s^{-1}}$, for the [S II] 6730 Å and the [O I] 6300 Å lines, respectively). All these values for the wings of the HVC in RU Lup are typically higher than those of other TTS with this forbidden emission, often by at least $100\,\mathrm{km\,s^{-1}}$, as can be seen in Figure 17 of Fang et al. (2018) for the case of the [O I] 6300 Å line.

These two line profiles show two distinct components: an HVC peaking at ~ -200 km s^{-1} and a LVC peaking at ~ -17 km s^{-1}. The LVC of both lines is dominated by a narrow low-velocity component (NLVC), while the HVC contains two components, with one less defined very broad component at ~ -75 and $\sim -105\,\mathrm{km\ s^{-1}}$ for the [S II] 6730 Å and the [O I] 6300 Å line, respectively (see 4.10). The broad component of the [O I] 6300 Å line has a broader width (roughly $400\,\mathrm{km\,s^{-1}}$) than that of the [S II]

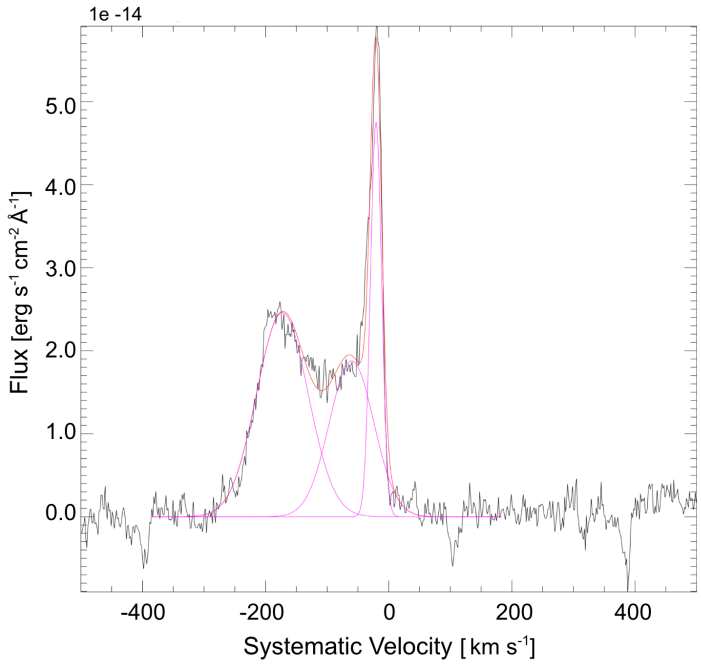

Figure 4.10: An example of one of the Gaussian decompositions of the [S II] 6730 Å lines from 14-06-2011. The spectra are continuum-subtracted and flux calibrated.

6730 Å line (roughly 200 km s^{-1}). These are quite common features in the jets and winds of CTTSs (Rigliaco et al., 2013; Simon et al., 2016; McGinnis et al., 2018).

While the main component of the HVC is tracing the collimated jet, the broad component is often associated with the base of the jet or a disk-wind and the NLVC with a slow-moving compact disk-wind or a photoevaporative wind from the disk (see e. g. Ray et al., 2007; Simon et al., 2016). In the case of RU Lup, the different nature of such components has been recently confirmed by the spectro-astrometric analysis of Whelan et al. (2021). Here the authors showed that the HVC and the broad component come from the extended jet and base of the jet, respectively, whereas the NLVC originates from a very compact ($\lesssim$ 8 au) MHD disk-wind.

Interestingly, these measurements of the HVC and LVC radial velocities match very well the total jet and wind velocities measured or inferred in other CTTSs of similar mass (see e. g. Ray et al., 2007, and references therein). This is a further indication that the disk geometry is almost face-on ($16° \pm {}^{6°}_{8°}$; Gravity Collaboration et al., 2021), namely the outflow is approaching the observer with a small inclination angle.

Indeed, because of the disk geometry, very little of the red-shifted emission from the outflow is observed, as it is located on the side of the star facing away from us, hidden by the disk. This explains why the red-shifted HVC is not detected in the spectra (see Figure 4.3).

4.4 Discussion

The results presented in Sec. 4.3 show that accretion in RU Lup varies from night-to-night over a period of 15 nights by about a factor of two. All the analysed accretion tracers (emission line luminosities, profiles, veiling) give consistent results. Notably, the average value of $\dot{M}_{\rm acc}$ in this period agrees well with values found at different epochs in the studies of Herczeg & Hillenbrand (2008) ($\sim 1.8 \times 10^{-8}\,M_{\odot}\,{\rm yr}^{-1}$) and Alcalá et al. (2017) ($\sim 6.7 \times 10^{-8}\,M_{\odot}\,{\rm yr}^{-1}$) mentioned earlier. It is therefore likely that the variability pattern found is typical of RU Lup's accretion at this stage of its evolution. In addition, as mentioned in Section 4.3.2, the extinction of RU Lup is negligible and has not been taken into consideration in this study. As the EW of each absorption line analysed changes slightly over these short timescales, this indicates that such variability is due to veiling and not to extinction.

As Fig. 4.3 clearly shows, there is no variability of the line profile or flux of the [O I] 6300 Å or [S II] 6730 Å forbidden lines in the timescale covered by these data. As was discussed in Section 2.2, this is expected for the HVC, however if either of the other components were to originate from an MHD disk wind located in the innermost region of the disk, where accretion occurs, then it could be expected to see some variability of that component on similar timescales as accretion. Simon et al. (2016) and McGinnis et al. (2018) show that the NLVC of the [O I] 6300 Å line originates from the inner disk, but far enough from the central object that it should not be directly impacted by accretion (>0.5 au, which was confirmed for RU Lup by Whelan et al. (2021)), whereas the BC seems to trace a wind from closer in (between ~ 0.05 au and ~ 0.5 au from the central object). This latter component has velocities of $\lesssim 50\,{\rm km\,s}^{-1}$ and is therefore a LVC, unlike the BC of the [O I] 6300 Å line of RU Lup, which is more blue-shifted. It is therefore evident that the broad component seen in the [O I] 6300 Å line profile of RU Lup is not the same component as the broad low-velocity component (BLVC) described by Simon et al. (2016) and McGinnis et al. (2018) in their samples, but is likely an intermediate velocity component linked to the base of the jet (Whelan et al., 2021). This star therefore lacks the BLVC which is linked to an MHD disk wind in the innermost part of the disk.

4.4.1 Accretion luminosity's relationship with the stellar rotation

Variation in the observed $L_{\rm acc}$ is sometimes associated with the stellar rotation if the line of sight intercepts a single or multiple accretion spots (Costigan et al., 2014), the

properties of which are relatively stable over several rotation periods. For instance, Alencar et al. (2018) show that the veiling measured in LkCa15 varies by a factor of $\sim$5 over the course of a few rotation cycles, and that this variability folds well in phase with the star's rotation period (see their Fig. 5). Similarly McGinnis et al. (2020) show that the veiling variability and, even more pronounced, the flux of the He I emission line at 5876 Å, of the star IP Tau has a clear modulation at the star's rotation period.

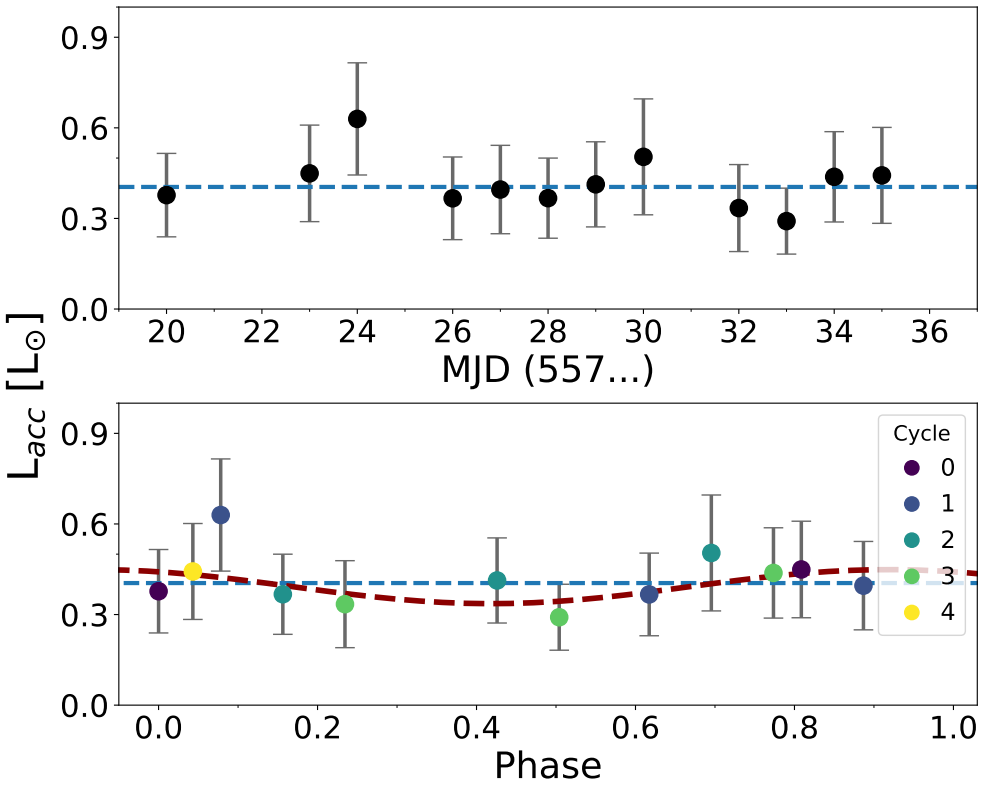

Figure 4.11: $L_{\rm acc}$ variability across the 12 epochs (upper panel) and folded in phase with the rotation of the star (lower panel). The period is 3.71 days (Stempels et al., 2007). The colour of the data points in the lower panel indicates the cycle of rotation of the star. The parameters of the sinusoidal fit are: amplitude $= 0.06 \pm 0.01$, offset $= 0.39 \pm 0.01$ and phase $= 2.1 \pm 0.1$. The correlation measure Kendall's τ_b was measured as $\tau = -0.061$ and p-value $= 0.84$ between the veiling measurements and the phase of the star's rotation, thus indicating it is very likely no correlation is present. The blue dashed line indicates the median value of accretion luminosity of 0.48 $L_\odot$.

However, given the nearly face-on geometry of RU Lup's disk (Gahm et al., 2013; Gravity Collaboration et al., 2021), it is not expected that the observed variability is related to stellar rotation. This is because the post-shock region, which is the region responsible for most of the emission, would always be visible in a face-on geometry (e.g. EX Lupi in Sicilia-Aguilar et al., 2015). The accretion columns falling onto the star are understood to land near the pole (Hartmann et al., 1994), and the flux levels would not

vary much with the rotation of the star. However, when studying the effects of rotation on radial velocities of certain lines in the RU Lup spectrum, Gahm et al. (2013) found they folded in phase nicely with the period of the star. The authors also note that they found no dependence of rotation on veiling (as done here in Fig. 4.12). Therefore, while velocity modulations may be seen, a change in the observed flux is less likely to be observed.

Checking this in this study of RU Lup, I investigate how $L_{\rm acc}$ varies as a function of the stellar rotation period. In Fig. 4.11, the variability of $L_{\rm acc}$ is presented across the roughly two weeks of the observations (upper panel) and folded in phase with the rotation of the star (lower panel) which has a period of 3.71 days (Stempels et al., 2007). To quantify the amount of $L_{\rm acc}$ variability potentially due to rotation, a sinusoidal curve is fit to the folded data. The resulting fit (red-dashed curve) is shown in the lower panel of Fig. 4.11 and the fit parameters are listed in the figure's caption. Similar plots are shown in Fig. 4.12 for the veiling derived from the Li I 6707 Å line ($r_{\rm Li\,I}$) variability *vs.* time and folded in phase with stellar rotation (upper and lower panel, respectively).

If the variability seen in these two quantities was solely due to RU Lup's rotation, the lower panels of Fig. 4.11 and Fig. 4.12 would show a distinct sinusoidal trend. However, the data vary in a more complex way, indicating that an intrinsic variability in the star's accretion exists. These plots indicate that any effect of rotational modulation on the observed variability is insignificant.

4.4.2 Intrinsic accretion variability

As the bulk of RU Lup's accretion variability cannot be due to stellar rotation nor to extinction, it must then be related to variations of the mass accretion rate (a factor of 2 or 0.31 dex, see Table 4.4) onto the star during the 15-day spectroscopic monitoring. On this observational timescale, such variability is similar to what was found in other photometric and spectroscopic studies of CTTSs (Costigan et al., 2012; Venuti et al., 2014; Zsidi et al., 2022).

By spectroscopically monitoring a sample of 15 CTTSs and Herbig Ae/Be stars, Costigan et al. (2014) derived that their mean accretion rates change from 0.04 to 0.4 dex on a daily basis. The photometric monitoring of ∼750 young stars by Venuti et al. (2014) found a 0.5 dex variability over a period of two weeks.

For what concerns RU Lup's accretion variability, long-term photometric monitoring by Siwak et al. (2016) already showed stochastic variability and lack of a single stable periodic pattern in its light-curves. The authors inferred that an unstable accretion regime, typical of CTTSs with high-mass accretion rates, operates in RU Lup. In

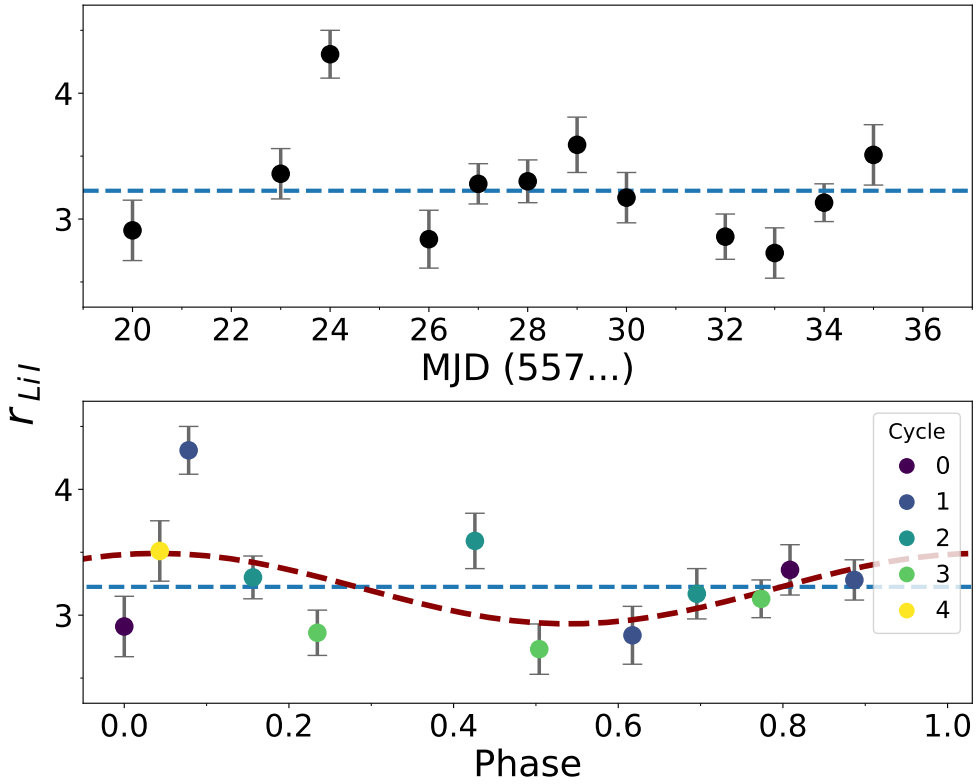

Figure 4.12: Veiling in the Li I 6707 Å line. $r_{\mathrm{Li\,I}}$ variability across the 12 epochs (upper panel) and folded in phase with the rotation of the star (lower panel). The period is 3.71 days (Stempels et al., 2007). The colour of the data points in the lower panel indicate the cycle of rotation of the star. The parameters of the sinusoidal fit are: amplitude = 0.3 ± 0.1, offset = 3.2 ± 0.1 and phase = 1.3 ± 0.1. The correlation measure Kendall's τ_b was measured as $\tau = -0.12$ and p-value = 0.64 between the veiling measurements and the phase of the star's rotation, thus indicating it is likely no correlation is present. The blue dashed line indicates the median value of Li I veiling of 3.23.

particular, they argue that RU Lup's photometric variability is due to increased mass accretion rates that can prompt Rayleigh–Taylor (RT) instabilities, moving accretion from a stable to an unstable regime, as predicted by several 3D MHD simulations of disk accretion onto a rotating magnetised star (see Romanova et al., 2008; Kulkarni & Romanova, 2008, 2009).

Although several ingredients can influence such a transition (strength of the magnetic field - B, stellar rotation rate, misalignment between the star's rotation axis and its magnetic poles), Romanova et al. (2008) showed that the main player in the development of RT instabilities is the mass accretion rate.

During the stable regime, the accretion disk is blocked by the star's magnetic field, and, at the magnetospheric radius ($\sim 5\,R_*$), the accreting matter flows around the mag-

netosphere, forming two funnels that deposit matter near the star's magnetic poles, making accretion relatively stable. An increase in accretion rates and thus in density squeezes the magnetosphere in the equatorial region. As a consequence, it is energetically impossible for the inner disk matter to follow the resulting magnetospheric field lines. RT instabilities develop, causing matter to move towards the star across the field lines, until it reaches field lines that are energetically possible to follow. The matter is wound along these lines, forming miniature funnel flows and accreting at lower latitudes (Romanova et al., 2008; Kulkarni & Romanova, 2008, 2009).

These $\dot{M}_{\rm acc}$ results can be compared with the predictions from Romanova et al. (2008); Kulkarni & Romanova (2008, 2009) and verify whether RT instabilities might be the source of the observed variability in RU Lup. The $\dot{M}_{\rm acc}$ boundary value between the stable and unstable regime in a CTTS is provided by Eq. 1 of Kulkarni & Romanova (2008) and depends on the B, $M_\star$ and $R_\star$. For these calculations, the stellar parameters reported in Table 4.1 are used. The strength of RU Lup's magnetic field is not well constrained in the literature, however Johnstone & Penston (1986) provide an upper limit of $\sim$500 G, that will be adopted as B of RU Lup. Eq. 1 of Kulkarni & Romanova (2008) with RU Lup's parameters gives $\dot{M}_{\rm acc} \sim 1.6 \times 10^{-8}\, M_\odot\, {\rm yr}^{-1}$ as the critical mass accretion rate whereby the stable regime shifts to an unstable one. This $\dot{M}_{\rm acc}$ is lower than the observed range of $\dot{M}_{\rm acc}$ values in the target. Notably, lower B values would provide a lower boundary value for $\dot{M}_{\rm acc}$. Thus, the possibility of an unstable accretion regime in RU Lup is confirmed.

Kurosawa & Romanova (2013) employ the results of Romanova et al. (2008)'s 3D simulations to compute time-dependent accretion rates and calculate Hydrogen line profiles for a CTTS slightly more massive (0.8 $M_\odot$) and more magnetised (1000 G) than RU Lup, and with a slightly larger stellar radius (2 $R_\odot$). As expected from Eq. 1 of Kulkarni & Romanova (2008), the accretion rates derived by Kurosawa & Romanova (2013) for such a CTTS in the unstable regime are slightly higher than ours (see lower panel of Fig. 2 of Kurosawa & Romanova, 2013). However, the relative $\dot{M}_{\rm acc}$ variations are comparable to the observed variations in RU Lup.

4.4.3 Veiling in the Li I 6707 Å line

The Li I 6707 Å photospheric line is the deepest absorption line in the spectra and benefits from a high SNR, making it a more enticing photospheric line with which to study the veiling. However, this use of the Li I 6707 Å line potentially suffers from the uncertain Li abundance ($A({\rm Li}) = \log N({\rm Li})$) of pre-main sequence stars, due to the onset of Li nuclear burning. The Li abundance decreases as a star gets older, in a way that

depends on its stellar properties, i.e., mass and temperature (Palla et al., 2007).

It has been hypothesized that WTTSs are simply more evolved CTTSs with dissipated disks (Walter et al., 1988; Bertout, 1989). However, there are CTTSs and WTTSs that coexist (e.g., Fig. 15 of Kenyon & Hartmann, 1995), and their disk evolution is informed by their star-forming region and circumstellar environment (Bonnell et al., 2006; Rosotti et al., 2014). In addition, not all stars begin with the same disk mass and therefore do not have the same rates of evolution (Hartmann et al., 1998; Sicilia-Aguilar et al., 2006, 2010). The details of this complex evolution are beyond the scope of this study, however, the implication is that the amount of Li depletion (a known indicator of stellar age) is often higher in WTTSs than CTTSs, but cannot be assumed (Galli et al., 2015).

Therefore, the template used to measure the veiling needs to take the Li abundance of the target CTTS and the template WTTS into account. For example, if the Li in the template star is depleted, there will be less Li in the photosphere to absorb light and the EW of the Li I line will be less than an un-depleted star. Because the flux of the Li I 6707 Å line in the WTTS is compared with that of the CTTS to evaluate veiling, the abundances of Li must be similar, if not equal, ($A(\mathrm{Li})_{\mathrm{WTTS}} \simeq A(\mathrm{Li})_{\mathrm{CTTS}}$) to accurately identify the difference in line depth as a veiling effect.

RU Lup has had its abundance measured as $A(\mathrm{Li}) < 3.81$ dex, which indicates no depletion of Li (Biazzo et al., 2017). On the other hand, TAP 45 has A(Li) values ranging from 2.92 to 3.27, depending on the method used for determining it (see Column 8 of Table 1 in Sestito et al., 2008, their source #51). This means that this template has an A(Li) from 0.5 to 0.9 dex *lower* than RU Lup, leading to an underestimate of $r_{\mathrm{Li\,I}}$.

In order to correct for the difference in Li abundance between the WTTS template and RU Lup, the theoretical unveiled $\mathrm{EW_{Li}}$ of RU Lup given by Biazzo et al. (2017) is compared with the $\mathrm{EW_{Li}}$ that is measured in the spectrum of the template star, TAP 45, and derive a correction factor. Biazzo et al. (2017) analyse a sample of YSOs, which includes RU Lup, that were observed with X-Shooter (this sample is described in Alcalá et al., 2017; Frasca et al., 2017). They measure the $\mathrm{EW_{Li}}$ for each star from the observed data and then unveil these equivalent widths using the values of r_{6700} estimated in Frasca et al. (2017) from the code ROTFIT (e.g. Frasca et al., 2006, 2015). This value of veiling is extrapolated between the values Frasca et al. (2017) found for r_{6200} and r_{7100}. The notation $\mathrm{EW^{corr.}_{Li,\,CTTS}}$ represents the equivalent width of the Li I 6707 Å line in a CTTS with the veiling effect removed (or "unveiled") (see Section 3.1.1 of Biazzo et al., 2017). The value found for RU Lup in Biazzo et al. (2017) is $\mathrm{EW^{corr.}_{Li,\,RU\,Lup}} = 988 \pm 10$ mÅ.

This is illustrated in Fig. 4.13, where the teal line represents the observed Li I 6707 Å line of RU Lup, the orange line represents the template star, TAP 45, and the

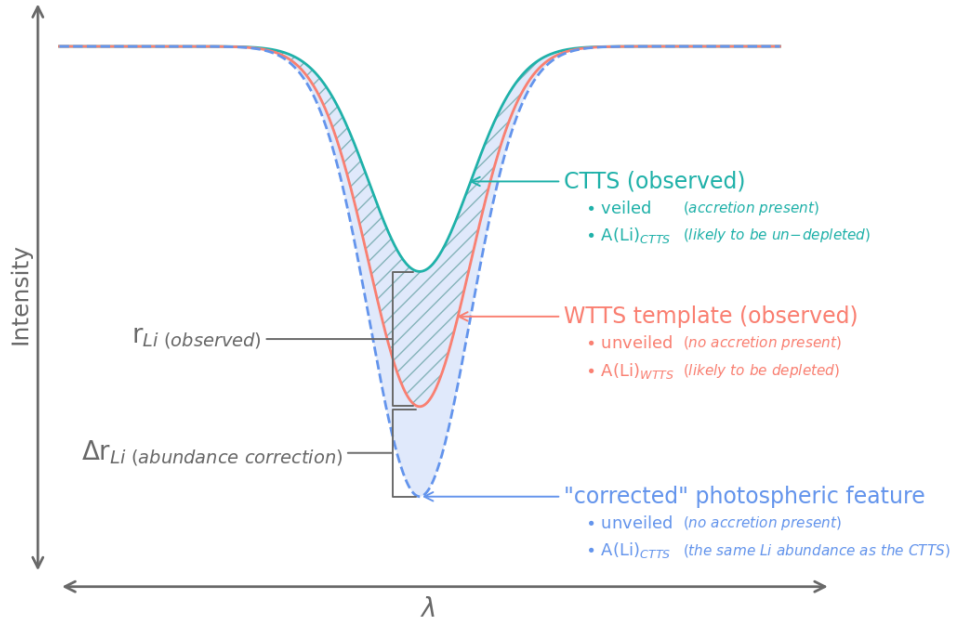

Figure 4.13: A diagram showing the difference in an observed CTTS (teal) Li I 6707 Å line and that of a WTTS (orange). The deepest absorption feature (dashed light blue) represents a spectrum with no veiling and the same abundance of Li I 6707 Å as the CTTS. The hatched region represents the difference in absorption depth between the CTTS and WTTS. The shaded region represents the difference in absorption depth between the CTTS and the unveiled CTTS spectrum.

dashed light blue line represents the absorption line of RU Lup when unveiled. The difference between the orange line's EW and the light blue line's EW is the difference of veiling measurement between the two templates. In this project, this is called the abundance correction factor ($\Delta\, r_{\rm Li}$) as it represents the discrepancy between the WTTS template and the template $\rm EW_{Li}$ of RU Lup unveiled: a difference only in Li abundance.

Rewriting Eq. 4.2 using this notation, the correction factor is defined as:

$$\Delta\, r_{\rm Li} = \frac{EW_{\rm Li}^{\rm corr.}}{EW_{\rm Li}} - 1, \tag{4.3}$$

where $\rm EW_{Li}^{corr} = 988 \pm 10\,m\AA$ and $\rm EW_{Li} = 352 \pm 10\,m\,\AA$ (the template star's (TAP 45) equivalent width of the Li I 6707 Å line.) This gives $\Delta\, r_{\rm Li} = 1.8$. A resultant total veiling can be found by summing $\Delta\, r_{\rm Li}$ and $r_{\rm Li\,I}$ (obs), which is taking the differing abundance between RU Lup and the template star TAP 45 into account.

It should be noted that there are large uncertainties in this correction factor, because of the way that the unveiled $\rm EW_{Li}$ of RU Lup was determined. RU Lup is a strongly veiled CTTS in which continuum veiling is likely not the dominant form of veiling (Gahm et al., 2008), meaning that individual photospheric absorption lines suffer from different amounts of veiling due to the filling in of lines by line emission (this will be explained

further in the next section Section 4.4.4). Therefore using an extrapolation of the veiling from other photospheric lines is not very accurate to determine the amount of veiling in the Li I line. However, this should be a good approximation, and in any case it does not affect the relative variation observed in the veiling of the Li I line and the results shown in Fig. 4.14.

Another method to determine veiling in the Li I line would be to simply compare the EWs of the Li I line in the observed spectra with the EW_{Li} given by Biazzo et al. (2017) using Eq. 4.2. However, it was decided instead to use the same method as was used to determine veiling for the Na I and Mn I lines and calculate a correction factor for the Li I abundance to maintain self-consistency. Regarding the measurement of veiling in these 2 other metal lines, it is preferable to compare the observed lines with a WTTS spectrum to determine veiling, rather than use a theoretical unveiled EW of each line as was done for Li I by Biazzo et al. (2017) and use Eq. 4.2, because there should not be a measurable difference in the abundance of these elements between the template and RU Lup, and therefore extrapolating values of veiling found from several photospheric lines by Frasca et al. (2017) to get an unveiled EW would only insert additional uncertainties to the measurements.

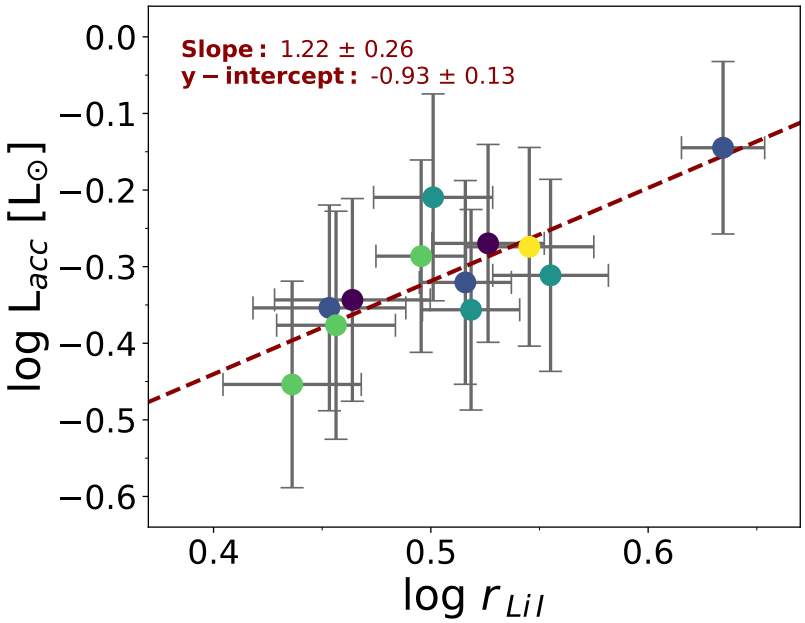

Figure 4.14: A fit representing how the veiling, estimated from the Li I 6707 Å absorption line (including a Li abundance correction - see Section 4.4.3), correlates with the L_{acc} logarithmically. The colours of the dots correspond to the same colour scheme used throughout this paper, as shown in Fig 4.3.

Even given these caveats, the most interesting finding of this study stands, the

relative variation of the veiling with time does not depend on the uncertainties of the Li I 6707 Å abundances in RU Lup itself nor in the template.

Fig. 4.14 shows the result that there is a close proportionality between $r_{\mathrm{Li\,I}}$ and L_{acc} for RU Lup. The absolute value of the accretion luminosity for a given value of $r_{\mathrm{Li\,I}}$ may depend on a number of stellar and accretion properties, and the possibility to derive L_{acc} from the Li I 6707 Å veiling alone needs to be explored further. However, the results suggest that in any individual star the variation of $r_{\mathrm{Li\,I}}$ may be correlated with variabilities in L_{acc}.

4.4.4 Continuum and line veiling

As noted in the previous section, the veiling values of the three metal lines studied, roughly agree within the uncertainties. However, a closer inspection shows that, while there is a rather tight correlation, the values of the veiling of different lines are not proportional to each other, as shown in Fig.8. In a system with only continuum excess emission, the veiling in these lines, which spreads over a relatively small interval of wavelengths, should present a 1:1 relationship with one another, as it is expected that the continuum will change by a very similar amount over this interval. This, however, is not going to be the case if accretion-related emission in the metal lines is also contributing to the overall veiling values. While the Na I 5688 Å line roughly traces that of the Li I 6707 Å, the Mn I 6021 Å veiling increases sharply as the Li I 6707 Å veiling increases. This implies that the Mn I 6021 Å line emission is increasing more strongly with increase in L_{acc} than the Li I 6707 Å and Na I 5688 Å line emission. However, Li I 6707 Å, Na I 5688 Å and Mn I 6021 Å all show strong reactions to an increase in accretion in RU Lup.

This accretion-related emission in metal lines, "line veiling", has been observed in a number of accreting TTS (e.g. Bertout, 1984; Hartigan et al., 1989; Gahm et al., 2008). In some, the line veiling has been found to be dominant, among them RU Lup (Gahm et al., 2008, 2013). The authors compare the V-band photometric variability of the star with the variability of the veiling and find that the veiling is not correlated, or only weakly related, to the stellar brightness during states of high veiling. They argue that there are two sources of veiling: a continuous excess emission, and narrow emission lines filling-in the photospheric absorption lines, both related to the accretion shocks and foot-prints of the accretion funnels. Line emission becomes the dominant component for high-veiling states ($r > 2$). In this case, a change in veiling does not lead to a corresponding change in stellar brightness, as it would happen if the veiling was caused by continuous emission alone.

Indeed this lack of correlation in highly veiled, and thus highly-accreting CTTSs, is

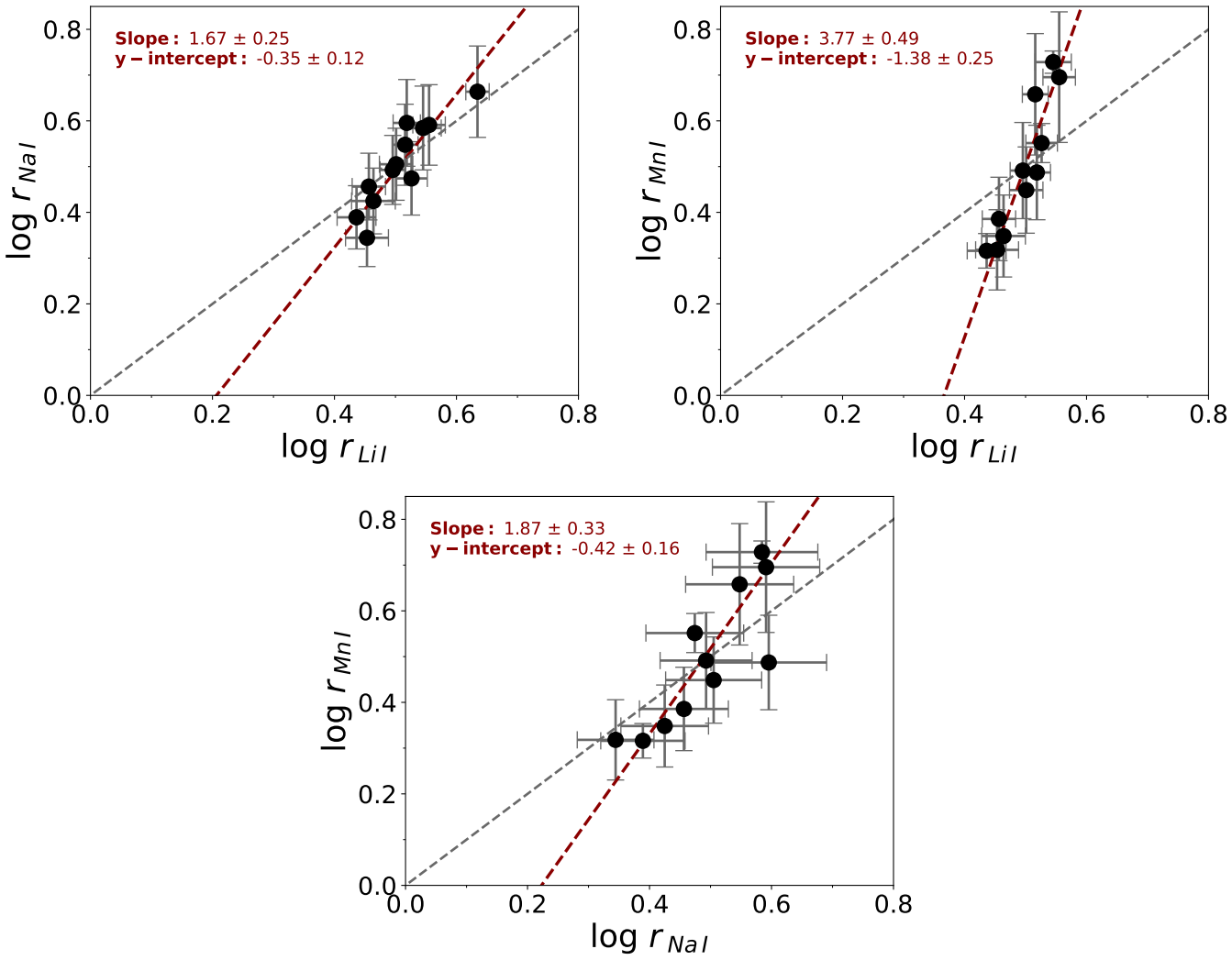

Figure 4.15: Log plots of the veiling measured in the metal lines of Li I 6707 Å, Na I 5688 Å and Mn I 6021 Å in comparison with each other. These plots allow visualisation of how the veiling can vary from one line species to another and that this is indicative of line emission veiling contributing to the total veiling measured in each.

confirmed by Rei et al. (2018). For a small sample of young active stars, Rei et al. (2018) find that the veiling is strongly line-dependent and is larger in strong photospheric lines and weaker or absent in the weakest ones. This concurs with what was found in the three metal lines, namely, the stronger lines exhibit stronger reactions to increases in accretion.

The cause of these variations in line veiling depend on the specific atomic transition, however, this requires further study. Gahm et al. (2008) examined the dependence of excitation potential on line depth, but found none. This was checked for the photospheric lines Li I 6707 Å, Na I 5688 Å and Mn I 6021 Å in this study, finding the excitation potentials do not vary greatly between the lines, indicating no dependence on the variations in line depth.

4.5 Summary and conclusions

The accretion variability of RU Lup has been investigated over time through the H I line luminosities and the veiling present in the photospheric metal lines Li I 6707 Å, Na I 5688 Å and Mn I 6021 Å. The main results are the following:

- $L_{\rm acc}$ and $\dot{M}_{\rm acc}$ were observed to vary by up to a factor of $\sim$2 over the 15 nights. This variability is an intrinsic variation of the accretion rates. In particular it does not reflect variations related to the stellar rotation.

- The average value of mass accretion rate found is $\dot{M}_{\rm acc,\,avg} = 4.8 \times 10^{-8}\,M_{\odot}\,{\rm yr}^{-1}$. This is within the spread of values found in Herczeg & Hillenbrand (2008) ($1.8 \times 10^{-8}\,M_{\odot}\,{\rm yr}^{-1}$) and Alcalá et al. (2017) ($6.7 \times 10^{-8}\,M_{\odot}\,{\rm yr}^{-1}$).

- The wind-tracing emission lines ([O I] 6300 Å and [S II] 6730 Å) are very stable over the time interval of these observations. They do not reflect the short-term changes in the mass accretion rate.

- In comparing the models of Romanova et al. (2008); Kulkarni & Romanova (2008, 2009), it is established that RU Lup is likely to be in an unstable accretion regime.

- The Li I 6707 Å absorption line is measured to have an average ${\rm EW}_{\rm Li\,I} = 0.17 \pm 0.03$ Å and an average $r_{\rm Li\,I} = 3.25 \pm 0.20$ when the Li depletion in the template star TAP 45 is taken into account.

- The temporal variability pattern over the 15 nights for $r_{\rm Li\,I}$ is strongly correlated to that of $L_{\rm acc}$ (see Fig. 4.14).

- The veiling measured in the photospheric absorption lines Na I 5688 Å ($r_{\mathrm{Na\,I\ avg}} = 3.27 \pm 0.63$) and Mn I 6021 Å ($r_{\mathrm{Mn\,I\ avg}} = 3.29 \pm 0.67$) demonstrate positive, although different, correlations with the veiling measured in Li I 6707 Å and $r_{\mathrm{Li\,I\ avg}} = 3.25 \pm 0.20$. This reveals the relative importance of emission line veiling in each individual line's total veiling. The veiling found in Mn I 6021 Å, for example, increases more rapidly than the other metal lines, given an increase in accretion.

- The correlation detected between changes in the accretion luminosity and changes in the veiling is strong and provides further evidence that the variability observed is not caused by extinction (the veiling measurements are unaffected by extinction because they are obtained by comparing two normalised spectra).

Because of the strength of the Li I 6707 Å line in CTTSs, its veiling can be an excellent tool in monitoring accretion variability that is independent of extinction and flux calibration. This relationship between variabilities in $r_{\mathrm{Li\,I}}$ and L_{acc} over short timescales can be further explored in other CTTSs to characterise accretion activity regardless of their visual extinction.

A future multi-object study aimed at calibrating this relationship could benefit from the careful selection of template stars that have similar Li abundances as the targets. The correlation between these two quantities found in this paper need not only be applied to the Li I photospheric line, however, its prevalence in TTSs and high SNR make it a better tool than other metal lines that are not always visible. The techniques explained in this paper also provide useful methods to calculate veiling in the absence of a perfect template star, opening the door for more research into the accretion processes in young stars.

5

Conclusions and Future Work

5.1 Conclusions

The first project (Chap. 3) detailed in this thesis explored the accretion variability found in the Class I protostar, IRS 54. Utilising NIR (J, H and K) spectroscopic observations over four epochs roughly a decade apart, a burst in accretion activity was detected. This burst was not only in the brightness of the protostar, but also in the mass accretion rate, and is consistent with the photometric data obtained during the same epochs. The change in shape of the SEDs of each epoch was interpreted as a tandem increase in both accretion and extinction over the course of the burst, an unexpected result. A possible explanation is that the increase of accretion and ejection activity during the burst lifts up material, obscuring the line of sight, leading to an increase in extinction. The dramatic increase and subsequent fall in flux is reminiscent of EXor-type bursts that exhibit these phenomena over similar timescales. IRS 54 is a VLMS and as such is one of the lowest mass Class I sources to demonstrate such a violent burst in accretion and ejection.

In the second project (Chap. 4), the Class II PMS star RU Lup was characterised through optical spectroscopy and photometry. Upon measuring the accretion luminosity and mass accretion rate across two weeks, RU Lup was found to exhibit an intrinsic variability of up to a factor of ~ 2. Due in part to RU Lup's especially face-on geometry, this variability is not dominated by the rotation of the star. Specific emission lines were studied to probe not only accretion phenomena, but ejection as well. The wind-tracing emission lines of [O I] 6300 Å and [S II] 6730 Å ([S II] is a doublet at 6716Å and 6730Å, but only latter was observable) were remarkably stable across the short timescales of this study, and therefore do not reflect any short-term changes in $\dot{M}_{\rm acc}$. Additionally, the veiling in RU Lup was measured across the epochs and compared with the varying $L_{\rm acc}$, producing a positive correlation between the two. This finding helps narrow down what exactly is being traced when the veiling is measured from a given photospheric line. The differences between veiling in different photospheric lines is explored in this chapter and it is hypothesized that these differences are due to the presence of continuum *and* emission line veiling. It is also found that the veiling in Li I correlates more strongly with $L_{\rm acc}$ than veiling in other metal lines. The power of the relationship between changes in $L_{\rm acc}$ and changes in the veiling in the Li I line, $r_{\rm Li}$, lies in how these two quantities are differently calculated: The $L_{\rm acc}$ is measured from an empirical relationship between the $L_{\rm line}$ and $L_{\rm acc}$ which is based on obtaining flux calibrated data, whereas the veiling is a ratio between two normalised spectra and does not depend on the actual fluxes

involved and is unaffected by extinction. This further strengthens the conclusion that the variability detected in accretion in RU Lup is intrinsic and not contaminated by extinction effects like the ones detected in IRS 54.

These two projects demonstrate the value of both optical and infrared observations in studying different classes of YSO. Observations at different wavelength ranges complement each other, highlighting different aspects of the star formation process, which demonstrates the need for simultaneous multi-wavelength observations to contextualise the individual processes in an object. This thesis does just that by looking first in the IR at a Class I protostar (invisible at optical wavelengths) and witnessing the dramatic accretion and ejection phenomena occurring during these early years of a star. Next, a Class II PMS star was examined at optical wavelengths, taking advantage of the plethora of strong emission lines visible in this range. By taking advantage of different wavelength ranges and techniques to study accretion on different timescales, this thesis provides useful insight into how young stars evolve through their protostar and pre-main sequence stages.

5.2 Future Work

The first proposed project draws inspiration from an accepted proposal of which I was the principal investigator (PI) along with co-investigators (CIs): Pauline McGinnis, Alessio Caratti o Garatti, Luisa Rebull and P. S. Teixeira. This proposal was submitted under ESO's Cycle P108 for the use of the instrument VLT/KMOS (described below). Although this proposal was accepted and the Phase 2 material was prepared (see Fig. 5.5 at the bottom of this section), the priority was not high enough to get observed during the requested cycle. Therefore, I intend to resubmit this proposal in the future to continue the work described throughout this thesis.

5.2.1 Using NIR observations to characterise Class I and II YSOs in NGC 2264

As an example of potential future projects that exploit what has been learnt from my research, I consider here the advantage of a multi-object spectroscopic survey using, for example, VLT/KMOS.

Young stellar objects (YSOs) represent a very early and important stage in a star's life that influences its evolution. Among YSOs, Class I protostars (see Top panel of Fig. 5.1) are very deeply embedded and are therefore invisible at optical wavelengths, as described in Section 1.1.3. Characterising these objects by measuring properties such

as their accretion luminosity, mass accretion rate, mass ejection rate, extinction toward the source and system geometry can only be done through spectroscopic observations in the IR, as has been demonstrated throughout this thesis. Because of this, Class I YSOs have not been studied in as much depth as their later-evolutionary counterparts such as Class II YSOs (see bottom panel of Fig. 5.1). Therefore, much of the current information and models on accretion processes in the early stages of star formation are inferred from Class II sources. However, it is in the Class I phase and earlier that YSOs undergo their strongest accretion activity (Contreras Peña et al., 2017). Moreover, strong accretion variability phenomena such as FUor and EXor bursts are important in defining a star's final mass and influencing its evolution. It has been found that in Class I YSOs, eruptive variability is at least one order of magnitude more common than in Class II YSOs (Contreras Peña et al., 2017). As accretion bursts have predominantly been studied in Class II sources, further investigation of variable accretion activity in Class I YSOs would be vital in providing a more clear picture of how common these phenomena are and how they influence the formation of young stars. As the chances of observing a source undergoing an episodic accretion burst are relatively small, the best strategy for a potential project is to perform a survey of YSOs.

This thesis has explored what is possible with medium and high resolution spectroscopy of these objects, however, single object studies are limited in scope. The logical follow-up to the determination of EXor-type outburst characteristics observed in IRS 54 (Chapter 3) is a broader examination of YSOs to establish what is common behaviour in Class I sources. Thus, a survey of the Class I population of a young stellar cluster in the NIR using the VLT instrument, the K-band Multi Object Spectrograph (KMOS, Fig. 5.2) would be ideal (Sharples et al., 2013). Such a young stellar cluster is NGC 2264 of age $\sim 1 - 5$ Myrs.

Targeting a particular star forming region with a multi-object spectrograph allows the observation of dozens of sources simultaneously in a small amount of time, increasing the chances to observe such bursts. By obtaining NIR spectroscopic data in NGC 2264, in addition to characterising Class I sources in the cluster, it would be possible to investigate the spectra for Exor- and FUor-specific spectroscopic features that can help identify systems that have recently undergone an accretion burst. Such features include CO bandheads ($2.3 - 2.4\,\mu$m) in emission (EXors) or in absorption (FUors), the Na I $2.206\,\mu$m doublet and sometimes Ca I $2.267\,\mu$m. It is suggested that these lines (CO, Na I , Ca I and H I) originate from the same region in a bursting YSO (Lorenzetti et al., 2009). Figure 5.3 shows two examples of the NIR spectrum of an EXor during a burst.

The star forming region NGC 2264 has been the object of many studies and has a well-characterised Class II population (see e.g. Lamm et al., 2004; Dahm & Simon,

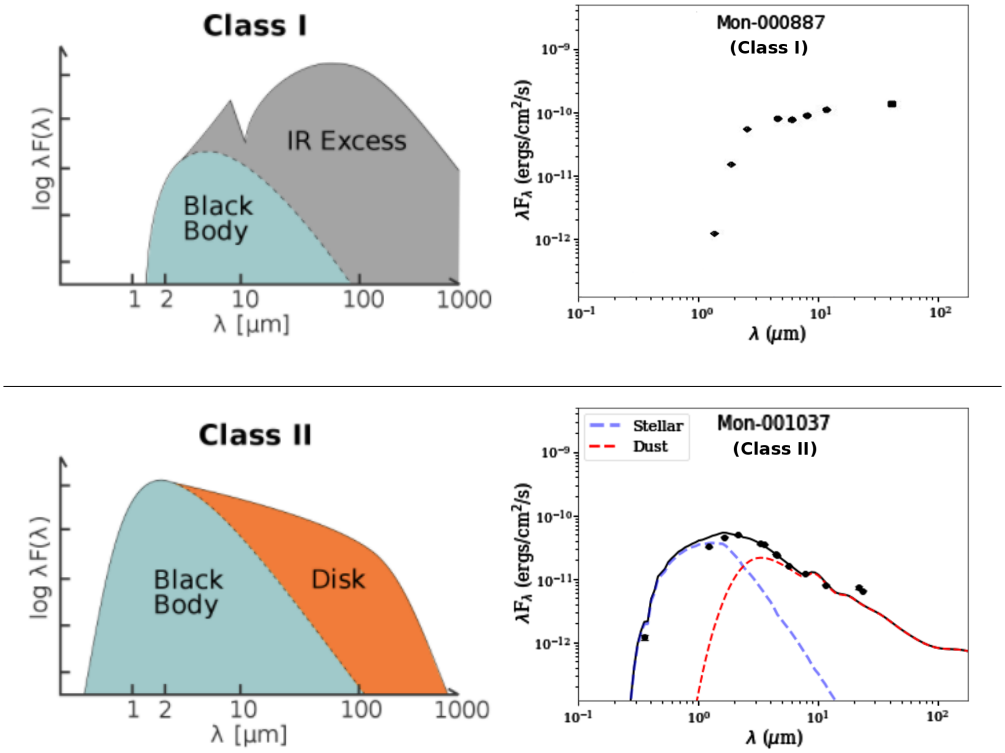

Figure 5.1: Left (Persson, 2014b) and Right (Luisa Rebull, obtained via private communication) examples of the spectral energy distribution of Class I and Class II YSOs. As the envelope surrounding a protostar begins to disperse, the central object becomes observable in the IR, with a large contribution (IR excess) from the surrounding dusty envelope and accretion disk (Class I, top panel). When the envelope surrounding a young star has fully dispersed, the central object becomes visible and the remaining IR excess is due to the accretion disk (Class II, bottom panel). The observed examples are of YSOs in NGC 2264 (Mon-000887 and Mon-001037).

2005; Alencar et al., 2010; Cody et al., 2014; Venuti et al., 2014; Sousa et al., 2016), however, its Class I population has been much less explored. It is conveniently situated in a region with very little interstellar extinction towards it, $A_V \sim 0.4$ mag (Flaccomio et al., 2006; Venuti et al., 2014) and at a distance of 760 pc (Sung et al., 1997). This region has shown evidence of sequential star formation (Venuti et al., 2018), therefore, most Class I sources are concentrated in a particular region, known as the Spokes cluster (Teixeira et al., 2006), which also optimises the number of targets that can be fit in each field.

Additionally, it would be possible to take advantage of the multi-object ability of KMOS to characterise and investigate Class II sources in the field that are potential eruptive variable candidates. It was shown by McGinnis et al. (2018) that most of the NGC 2264 Class II sources with a protostellar jet show very irregular short-term variability, similar to the short-term variability observed in EXors between bursts (Audard

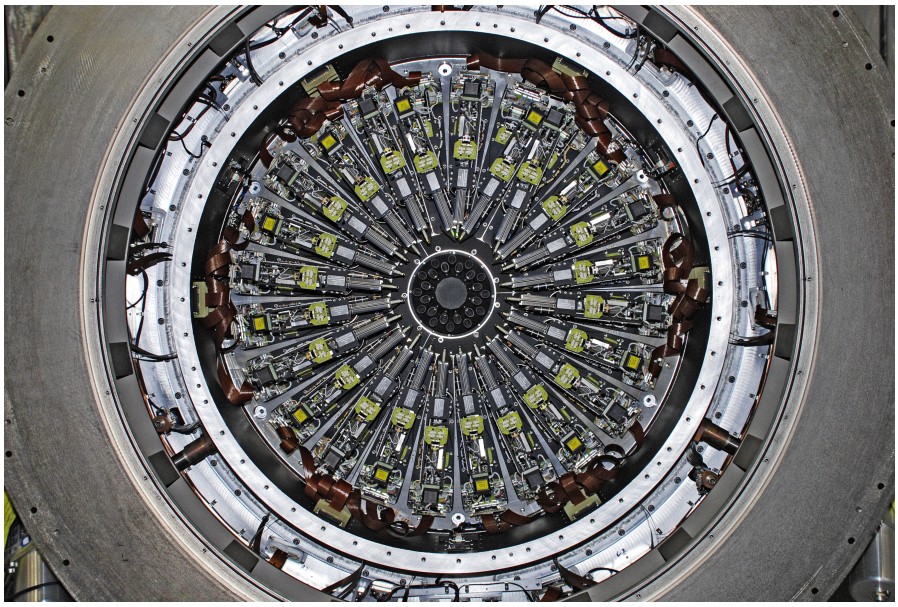

Figure 5.2: A view of the KMOS instrument showing all 24 robotic arms that each produce an IFU spectroscopic image *Credit:* STFC/UKATC/ESO.

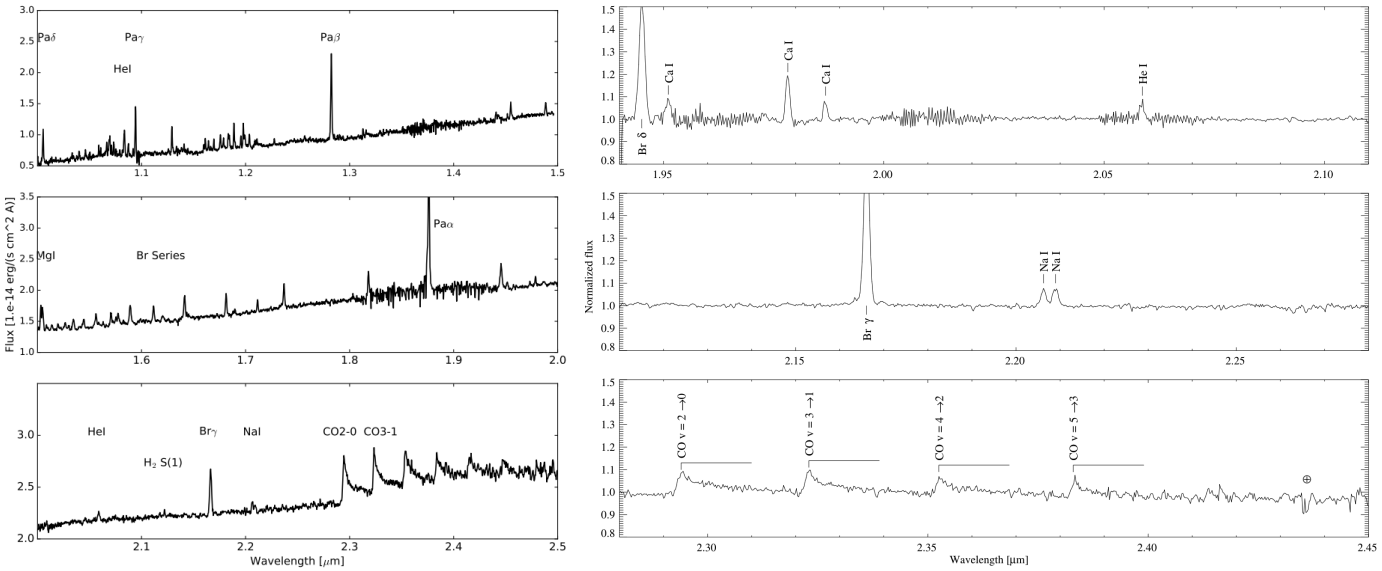

Figure 5.3: Two examples of YSOs during an EXor-type outburst. **Left panel:** J, H and K NIR spectra of ESO-Hα99, a young star bordering its Class I and Class II phase (Hodapp et al., 2019). **Right panel:** The normalised K band spectrum of the Class II, and protoype for the EXor-type outburst, EX Lup during its largest recorded burst (2008). The Earth symbol indicates telluric absorption (Kóspál et al., 2011). Note the difference in wavelength scale between the two observations.

et al., 2014). The jet launching mechanism is not yet well understood, but the spacing between individual knots seen in spatially resolved jets has led to the hypothesis that they may be linked to strong accretion bursts (Reipurth, 1989). These variable stars associated with jets are therefore excellent targets to search for EXor- and FUor-type characteristics in their NIR spectra.

Potential targets within the fields shown in Fig. 5.4 include 40 Class I sources, 16 Class II sources that are FUor candidates and another 5 Class II sources with a jet (spanning masses of $0.14 - 1.82\,M_{\odot}$). These targets are selected from a complete sample of all known Class I sources in NGC 2264 that have $J \leq 17$ mag and are grouped appropriately to fit within a few KMOS fields, optimizing the use of its multi-object capabilities. The NIR is the ideal wavelength range in which to study these objects as the visual extinction toward these deeply embedded objects is very high, rendering them invisible in the optical. As these objects have spectral energy distributions (SEDs) from previous years available in the literature, they can be compared with the obtained spectra, allowing the verification of how the luminosity has changed over time.

KMOS is ideally suited for observations of this nature. With 24 individual IFUs, it would be possible to use four different fields to survey the most sources possible in NGC 2264 (see Fig. 5.4). The 24 configurable IFUs allow individual spectra to be obtained for many objects in a short amount of time. KMOS's spectral resolution of $R \sim 4000$ is satisfactory to measure the spectral features of interest, which lie within the range of the instrument (YJ, H and K). If obtained, this data would make it possible to, i) characterise the Class I population of NGC 2264 in terms of its accretion and outflows and constrain mass and spectral type of the driving source (see e.g. Caratti o Garatti et al., 2012; Antoniucci et al., 2014), ii) search for candidate EXor and FUor variables among both Class I and Class II sources, iii) confirm the FUor status of a number of Class II sources which are FUor candidates by searching for the typical NIR spectral features, e.g. CO bandheads in absorption, lack of Brγ line, He I 1.08 μm in absorption (Audard et al., 2014; Connelley & Reipurth, 2018), iv) compare the frequency of EXor/FUor variables among the Class I and Class II population in NGC 2264, to verify if it follows the trends found in the literature.

Looking even further ahead, it would be beneficial to follow up EXor and FUor candidates identified in this study in subsequent years to obtain time-sampled NIR spectroscopic data and study the variability of the observed characteristics during a burst.

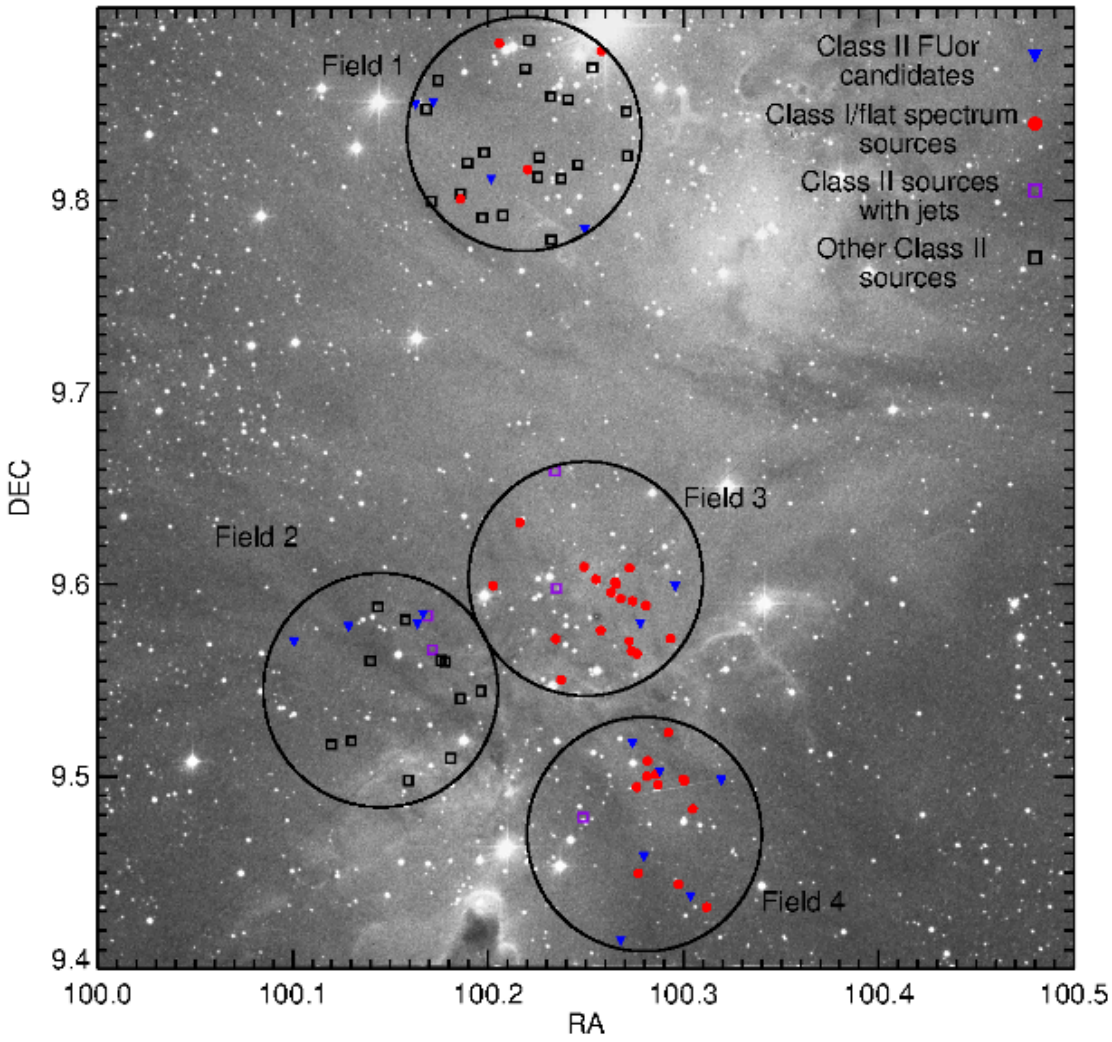

Figure 5.4: Fields of potential KMOS observations of Class I and Class II young stellar objects in NGC 2264.

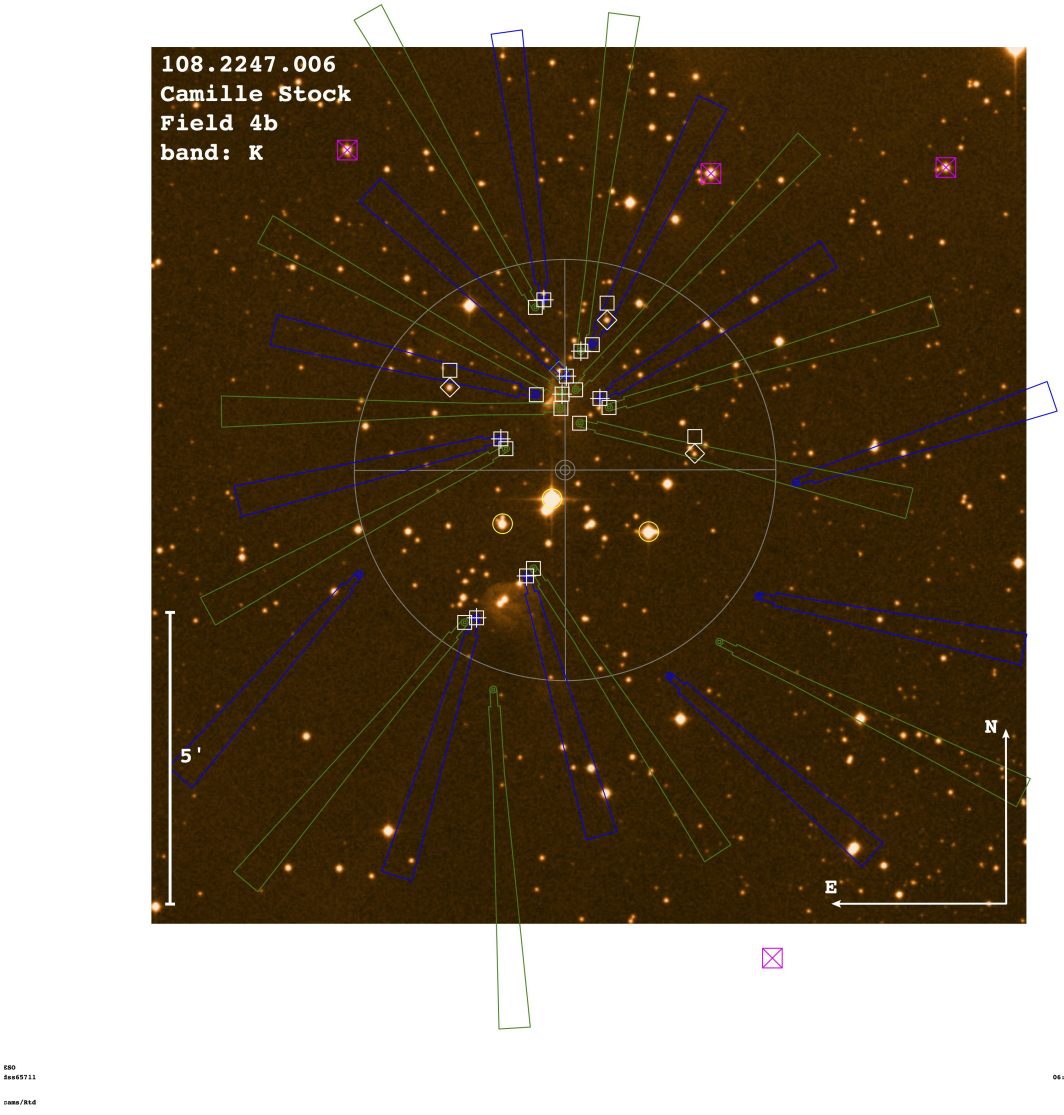

Figure 5.5: A view of the process undertaken to assign each of the 24 arms to a different target (both science and calibration targets) within one of the chosen KMOS fields. This was completed as part of the Phase 2 material for the original proposal.

5.2.2 Delving deeper into the relationship between veiling and accretion luminosity

In Chap. 4, it was established that in the Class II YSO RU Lup, there exists a positive correlation between the variability of veiling measured from the Li I 6707 Å line and the variability of the accretion luminosity calculated from the H I accretion-tracing lines. This relationship stands regardless of the exact values involved, as it arises from relative changes in these quantities. However, it would be very interesting and potentially fruitful to extend this analysis to a flux-calibrated survey of CTTSs, to establish a catalog of how accretion luminosity and veiling vary with respect to each other across Class II stars from multiple star formation regions.

This project would require the reduction of much archival data, however, there are many spectra that are already flux calibrated and merely need to have the veiling measured (when there is enough accretion present to make it possible). If this catalog contained absolute measures of the slope of the positive relationship found between accretion luminosity and veiling in Li I, it would open the door to potentially using the slope together with veiling measurements from a CTTS to estimate the accretion luminosity. This would be a great help to the field of CTTS studies because the veiling measurement does not require flux calibration and is independent of extinction. This could help ease the strain on telescope time for observing separate standard stars used for flux calibration, when an estimate of accretion luminosity is the goal. Additionally, this would allow an accretion luminosity to be estimated for decades of archival data that did not contain observations of a standard star for calibration purposes (e.g. the ESPaDOnS archival data, as in Chap. 4).

This is all contingent on accurately calculating the parameters of this correlation between accretion luminosity and veiling for enough CTTSs that generalisations between stars of similar masses and age can be drawn.

5.2.3 Concluding remarks

Throughout this thesis, I have explored the intricate and complex processes occurring in the inner regions of YSOs, and found that they are anything but predictable. These systems' accretion is variable on multiple timescales and heavily influences along which track a star will evolve. This field, as with most fields in astronomy, is predominantly restricted by the current detector and telescope technologies. A recent breakthrough includes the James Webb Space Telescscope (JWST) which boasts multiple cutting-edge infrared instruments: Near-Infrared Camera (NIRcam), Near-Infrared

Spectrograph (NIRspec), Fine Guidance Sensor/Near-Infrared Imager and Slitless Spectrograph (FGS/NIRISS) and Mid-Infrared Instrument (MIRI) which span a wavelength range of $0.6 - 5.0\,\mu$m (NIR instruments) and $5.0 - 28.0\,\mu$m, respectively (Gardner et al., 2006). The spectral resolution possible from a space telescope is superior to that of a ground-based telescope, which will allow science such as that described in this thesis to be done without burdensome atmospheric corrections. JWST joins other impressive space telescopes, such as the Hubble Space Telescope and the Spitzer Space Telescope, to provide more infrared insight. Comparisons between the instruments are shown in Figs. 5.6 and 5.7. It is an exciting time to be doing infrared astronomy, and I look forward to witnessing the interesting science and discoveries that come about from JWST.

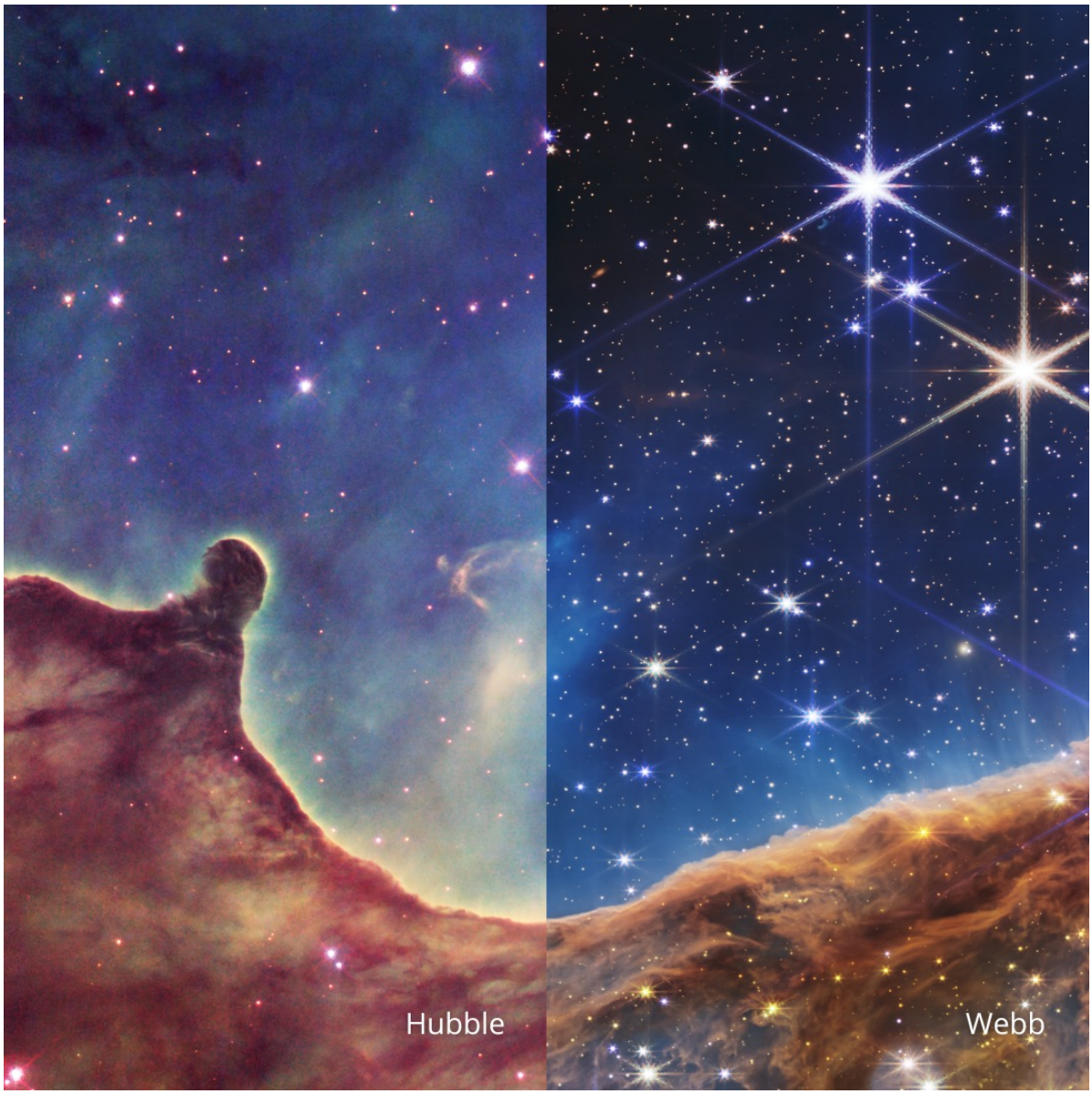

Figure 5.6: A portion of the Carina Nebulae as seen with the Wide Field Planetary Camera 2 (WFPC2) on board the Hubble Space Telescope in 2008 (*Credit:* NASA/ESA/STScI/AURA/N. Smith (University of California, Berkeley), in comparison with the NIRcam instrument on board the James Webb Space Telescope in 2022 (*Credit:* NASA/ESA/CSA/STScI).

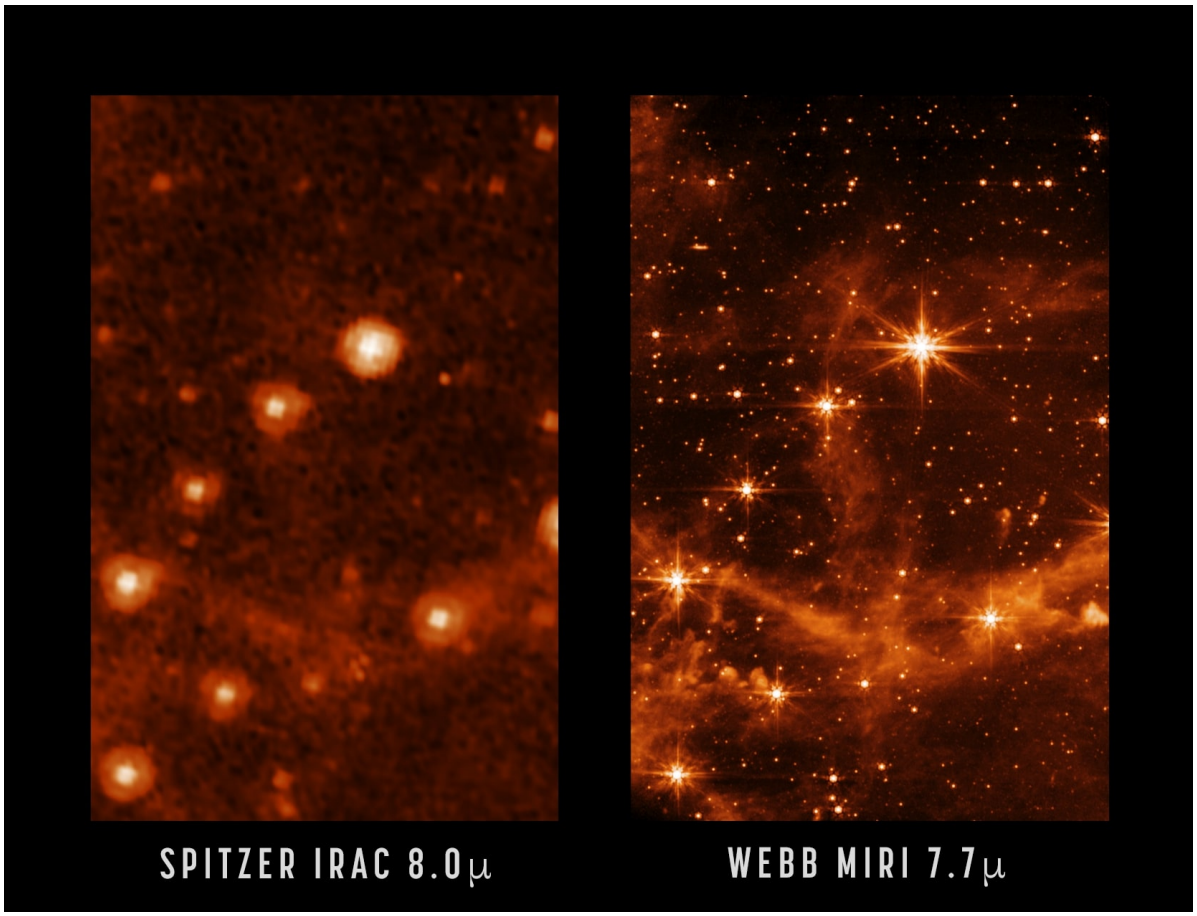

Figure 5.7: A portion of the Large Magellanic Cloud taken with the Spitzer Space Telescope Infrared Array (*Credit:* NASA/JPL-Caltech) in 2003, in comaprison with the MIRI instrument on board the James Webb Space Telescope in 2022 (*Credit:* NASA/ESA/CSA/STScI).

Bibliography

ALMA Partnership et al., 2015, ApJL, 808 L3 8, 10

Ábrahám P., et al., 2019, ApJ, 887, 156 79

Alcalá J. M., et al., 2014, A&A, 561 1, 17, 83

Alcalá J. M., et al., 2017, A&A, 600, 20 14, 17, 18, 19, 20, 64, 65, 70, 72, 82, 83, 90, 95, 101, 106, 111

Alcalá J. M., et al., 2021, A&A, 652 17

Alencar S. H. P., et al., 2010, A&A, 519, A88 27, 116

Alencar S. H., et al., 2018, A&A, 620, A195 102

Allart R., et al., 2022, accepted to A&A 42

Ambartsumian V. A., 1958, Theoretical Astrophysics. Pergamon Press 6

André P., Belloche A., Motte F., Peretto N., 2007, A&A, 472, 519 56

Andrews S. M., et al., 2016, ApJL, 820 L40 8

Ansdell M., Gaidos E., Williams J. P., Kennedy G., Wyatt M. C., Lacourse D. M., Jacobs T. L., Mann A. W., 2016, MNRAS, 462, 101 28

Antoniucci S., García López R., Nisini B., Caratti o Garatti A., Giannini T., Lorenzetti D., 2014, A&A, 572, A62 95, 118

Appenzeller I., Mundt R., 1989, A&AR, 1, 291 7, 50

Argiroffi C., Maggio A., Peres G., 2007, A&A, 465, L5 16

Audard M., et al., 2010, A&A, 511, 63 27

Audard M., et al., 2014, Protostars and Planets VI 27, 53, 63, 116, 118

Bailer-Jones C. A. L., Rybizki J., Fouesneau M., Mantelet G., Andrae R., 2018, AJ, 156, 58 82

Banzatti A., Pascucci I., Edwards S., Fang M., Gorti U., Flock M., 2019, ApJ, 870, 76 99

Barsony M., Kenyon S. J., Lada E. A., Teuben P. J., 1997, ApJS, 112, 109 68

Barsony M., Haisch K. E., Marsh K. A., McCarthy C., 2012, ApJ, 751, 22 68

Batalha C., Batalha N. M., Alencar S. H. P., Lopes D. F., Duarte E. S., 2002, ApJ, 580 83

Beristain G., Edwards S., Kwan J., 2001, ApJ, 551, 1037 90

Bertout C., 1984, Reports on Progress in Physics, 47, 111 6, 109

Bertout C., 1989, ARA&A., 27, 351 106

Beuther H., Churchwell E. B., Mckee C. F., Tan J. C., 2007, Protostars and Planets V, pp 165–180 8

Biazzo K., Alcalá J. M., Covino E., Frasca A., Getman F., Spezzi L., 2012, A&A, 547 17

Biazzo K., et al., 2017, A&A, 605, 66 106, 108

Blitz L., 1993, Protostars and Planets III 1

Bodenheimer P. H., 2011, Principles of Star Formation. Springer Berlin Heidelberg, doi:10.1007/978-3-642-15063-0 22

Boltzmann L., 1884, Annalen der Physik, 258, 291 29

Bonnell I. A., Larson R. B., Zinnecker H., 2006, Protostars and Planets V, pp 149–164 106

Bouvier J., Alencar S. H. P., Harries T. J., Johns-Krull C. M., Romanova M. M., 2007, Protostars and Planets V, pp 479–494 10, 14, 83

Bouvier J., Grankin K., Ellerbroek L. E., Bouy H., Barrado D., 2013, A&A, 557, 77 27

Burrows C. J., et al., 1996, ApJ, 473, 437 23, 24

Calvet N., Gullbring E., 1998, ApJ 16, 17, 19

Calvet N., Hartmann L., 1992, ApJ, 386, 239 10, 24, 51

Calvet N., Muzerolle J., Briceño C., Hernández J., Hartmann L., Saucedo J. L., Gordon K. D., 2004, AJ, 128, 1294 17, 64, 72

Calvet N., et al., 2005, ApJ, 630, L185 11

Camenzind M., 1990, Reviews in Modern Astronomy, 3, 234 10

Campbell-White J., Sicilia-Aguilar A., Manara C. F., Matsumura S., Fang M., Frasca A., Roccatagliata V., 2021, MNRAS, 507, 3331 29

Caratti o Garatti A., Eislöffel J., 2009, ASSP, 0, 329 23

Caratti o Garatti A., Giannini T., Nisini B., Lorenzetti D., 2006, A&A, 449, 1077 66

Caratti o Garatti A., et al., 2012, A&A, 538 118

Catanzaro G., 1997, Ap&SS, 257, 161 84

Cody A. M., et al., 2014, AJ, 147, 2014 116

Connelley M. S., Greene T. P., 2014, AJ, 147, 125 66

Connelley M. S., Reipurth B., 2018, ApJ, 861, 145 118

Contreras Peña C., et al., 2017, MNRAS, 465, 3011 27, 28, 53, 97, 115

Costigan G., Scholz A., Stelzer B., Ray T., Vink J. S., Mohanty S., 2012, MNRAS, 427, 1344 81, 103

Costigan G., Vink J. S., Scholz A., Ray T., Testi L., 2014, MNRAS, 440, 3444 28, 81, 101, 103

Curcio J. A., Drummeter L. F., Knestrick G. L., Curcio J. A., Drummeter L. F., Knestrick G. L., 1964, ApOpt, 3, 1401 42

Cutri R., et al., 2003, VizieR Online Data Catalog, 2246, 0 68

DENIS Consortium 2005, VizieR Online Data Catalog, p. II/263 68

Dahm S. E., Simon T., 2005, AJ, 129, 829 115

Davis C. J., Ray T. P., Desroches L., Aspin C., 2001, MNRAS, 326, 524 66

Davis C. J., et al., 2011, A&A, 528 64

DePoy D. L., et al., 2003, SPIE, 4841, 827 47

Decampli W. M., 1981, ApJ, 244, 124 23

Dodd S., Lancaster G., Craig J., Smyth R., Williamson P., 2006, Blackbody Spectrum Figure 30

Dodin A. V., Lamzin S. A., 2012, Astron. Lett., 38, 649 16, 19, 97, 98

Dodin A., et al., 2019a, MNRAS, 482, 5524 28

Dodin A., et al., 2019b, MNRAS, 482, 5524 76

Donati J. F., Semel M., Carter B. D., Rees D. E., Cameron A. C., 1997, MNRAS, 291, 658 37, 84

Donati J. F., Catala C., Landstreet J. D., Petit P., 2006, ASPC, 358, 362 46

Donati J.-F., et al., 2010a, MNRAS, 402, 1426 28

Donati J.-F., et al., 2010b, MNRAS, 409, 1347 28

Dougados C., 2008, Jets from Young Stars II, Lecture Notes in Physics, 742, 105 41

Dullemond C. P., Monnier J. D., 2010, ARA&A, 48, 205 5, 13, 14

Dullemond C. P., van den Ancker M. E., Acke B., van Boekel R., 2003, ApJL, 594, L47 28

Dunham M. M., Vorobyov E. I., 2012, ApJ, 747, 52 25

Dunham M. M., et al., 2014, Protostars and Planets VI 8, 9

Duvert G., Guilloteau S., Ménard F., Simon M., Dutrey A., 2000, A&A, 355, 165 7, 19

D'Alessio P., Calvet N., Hartmann L., Lizano S., Canto J., 1999, ApJ, 527, 893 11

Edwards S., 2008, Lecture Notes in Physics, 742, 3 23

Edwards S., Cabrit S., Strom S. E., Heyer I., Strom K. M., Anderson E., 1987, ApJ, 321, 473 99

Edwards S., Hartigan P., Ghandour L., Andrulis C., 1994, AJ, 108, 1056 10

Eisenhauer F., et al., 2003, Instrument Design and Performance for Optical/Infrared Ground-based Telescopes, 4841, 1548 45, 56

Eislöffel1998 J., Mundt R., 1998, The Astronomical Journal, 115, 1554 23

Espaillat C., Calvet N., D'alessio P., Ndez J. H., Qi C., Hartmann L., Furlan E., Watson D. M., 2007, ApJ, 670, L135 11

Espaillat C., et al., 2014, Protostars and Planets VI 9, 11

Espaillat C. C., Robinson C. E., Romanova M. M., Thanathibodee T., Wendeborn J., Calvet N., Reynolds M., Muzerolle J., 2021, Nature, 597, 41 16

Esposito S., Pinna E., 2008, Jets from Young Stars II, Lecture Notes in Physics, 742, 45 41

Fang M., Boekel R. V., Wang W., Carmona A., Sicilia-Aguilar A., Henning T., 2009, A&A, 504, 461 17

Fang M., Sicilia-Aguilar A., Roccatagliata V., Fedele D., Henning T., Eiroa C., Müller A., 2014, A&A, 570 74

Fang M., et al., 2018, ApJ, 868, 28 99

Fedriani R., et al., 2018, A&A, 616, 126 23

Fedriani R., et al., 2019, Nature Communications, 10, 1 1

Fischer W. J., Safron E., Megeath S. T., 2019, ApJ, 872, 183 26

Fischer W. J., Hillenbrand L. A., Herczeg G. J., Johnstone D., Kóspál Á., Dunham M. M., 2022, Protostars and Planets VII, 26, 81, 83, 95

Flaccomio E., Micela G., Sciortino S., 2006, A&A, 455, 903 116

Frasca A., Guillout P., Marilli E., Ferrero R. F., Biazzo K., Klutsch A., 2006, A&A, 454, 301 106

Frasca A., et al., 2015, A&A, 575 106

Frasca A., Biazzo K., Alcalá J. M., Manara C. F., Stelzer B., Covino E., Antoniucci S., 2017, A&A, 602, 33 82, 106, 108

Gahm G. F., Walter F. M., Stempels H. C., Petrov P. P., Herczeg G. J., 2008, A&A, 482, L35 82, 87, 107, 109, 111

Gahm G. F., Stempels H. C., Walter F. M., Petrov P. P., Herczeg G. J., 2013, A&A, 560, A57 29, 87, 102, 103, 109

Gaia Collaboration et al., 2018, A&A, 616 82

Galli P. A. B., Bertout C., Teixeira R., Ducourant C., 2015, A&A, 580, 26 106

Gangi M., et al., 2022, A&A 17

García-López R., Nisini B., Giannini T., Eislöffel J., Bacciotti F., Podio L., 2009, Ap&SS Proceedings, pp 485–490 66

García-López R., Caratti o Garatti A., Weigelt G., Nisini B., Antoniucci S., 2013, A&A, 552, 2 54, 68

Gardner J. P., et al., 2006, Space Science Reviews, 123, 485 122

Gatti T., Testi L., Natta A., Randich S., Muzerolle J., 2006, A&A, 460, 547 17

Goodman J. W., 1995, Introduction to Fourier Optics, 2 edn. McGraw-Hill 40

Grankin K. N., 2013, Astron. Lett., 39, 251 85

Gras-Velázquez A., Ray T. P., 2005, A&A, 443, 541 7

Gravity Collaboration et al., 2021, A&A, 655, A73 82, 83, 100, 102

Gray D. F., 2005, The observation and analysis of stellar photospheres. Cambridge University Press 34

Gredel Roland 1994, A&A, 292, 580 49

Greene T. P., Wilking B. A., Andre P., Young E. T., Lada C. J., 1994, ApJ, 434, 614 9

Güdel M., Nazé Y., 2009, A&AR, 17, 309 16

Gullbring E., Hartmann L., Briceño C., Calvet N., 1998, ApJ, 492, 323 14, 16, 17

Gullikson K., Dodson-Robinson S., Kraus A., 2014, AJ, 148, 53 42

Günther H. M., Schmitt J. H. M. M., Robrade J., Liefke C., 2007, A&A, 466, 1111 16

Haisch, Jr. K. E., Greene T. P., Barsony M., Stahler S. W., 2004, AJ, 127, 1747 68

Hamann F., 1994, ApJS, 93, 485 99

Hartigan P., 2008, Lecture Notes in Physics, 742, 15 50

Hartigan P., Hartmann L., Kenyon S., Hewett R., Stauffer J., 1989, ApJS, 70, 899 21, 97, 109

Hartigan P., Kenyon S. J., Hartmann L., Strom S. E., Edwards S., Welty A. D., Stauffer J., 1991, ApJ, 382, 617 16, 97

Hartigan P., Edwards S., Ghandour L., 1995, ApJ, 452, 736 6, 86, 99

Hartmann L., 2009, Accretion Processes in Star Formation, second edn. Vol. 44, Cambridge University Press, doi:10.1088/1751-8113/44/8/085201 2, 4, 6, 8, 25, 26

Hartmann L., Calvet N., Avrett E. H., Loeser R., 1990, ApJ, 349, 168 23

Hartmann L., Hewett R., Calvet N., 1994, ApJ, 426, 669 10, 51, 102

Hartmann L., Calvet N., Gullbring E., D'Alessio P., 1998, ApJ, 495, 385 14, 17, 106

Hartmann L., Herczeg G. J., Calvet N., 2016, ARA&A, 54, 135 12, 14, 15, 16, 81

Herbig G. H., 1966, Vistas in Astronomy, 8, 109 25

Herbig G. H., 1977, ApJ, 217, 693 25

Herbig G. H., 1989, in ESO Workshop on Low Mass Star Formation and Pre-Main Sequence Objects. pp 233 – 246 25

Herbig G. H., 2008, AJ, 135, 637 27, 53

Herbig G. H., Bell R. K., 1988, Lick Observatory Bulletin, 1111, 90 50

Herbst W., Herbst D. K., Grossman E. J., Weinstein D., 1994, AJ, 108, 1906 81

Herbst W., Maley J. A., Williams E. C., 2000, AJ, 120, 349 27, 28

Herczeg G. J., Hillenbrand L. A., 2008, ApJ, 681, 594 14, 82, 83, 101, 111

Herczeg G. J., et al., 2005, AJ, 129, 2777 82, 83, 90, 95

Hillenbrand L. A., Findeisen K. P., 2015, ApJ, 808 27

Hodapp K. W., et al., 2019, AJ 117

Ingleby L., et al., 2013, ApJ, 767, 112 15, 16

Jeans J. H., 1902, RSPTA, 199, 1 2

Johns C. M., Basri G., 1995a, AJ, 109, 2800 24

Johns C. M., Basri G., 1995b, ApJ, 449, 341 28

Johns-Krull C. M., 2009, ASSP, 13, 33 24

Johns-Krull C. M., Basri G., 1997, ApJ, 474, 433 83

Johns-Krull C. M., Basri G., 2001, AJ, 122, 3335 90

Johns-Krull C. M., Valenti J. A., Hatzes A. P., Kanaan A., 1999, ApJ, 510, L41 37, 97

Johnstone R. M., Penston M. V., 1986, MNRAS, 219, 927 105

Joy A. H., 1949, ApJ, 110, 424 6, 19, 82

Kastner J. H., Huenemoerder D. P., Schulz N. S., Canizares C. R., Weintraub D. A., 2001, ApJ, 567, 434 16

Kenyon S. J., Hartmann L., 1995, ApJS, 101, 117 25, 106

Kenyon S. J., Hartmann L. W., Strom K. M., Strom S. E., 1990, AJ, 8, 9 25

Kenyon S. J., Gomez M., Marzke R. O., Hartmann L., Kenyon S. J., Gomez M., Marzke R. O., Hartmann L., 1994, AJ, 108, 251 25

Khanzadyan T., Gredel R., Smith M. D., Stanke T., 2004, A&A, 426, 171 54

Königl A., 1991, ApJL, 370, L39 10, 14

Kornilov V., Tokovinin A., Shatsky N., Voziakova O., Potanin S., Safonov B., 2007, MNRAS, 382, 1268 41

Kóspál A., et al., 2011, ApJ, 736, 72 117

Koutoulaki M., et al., 2019a, A&A, 625, A49 28

Koutoulaki M., et al., 2019b, A&A, 625, A49 76

Kuhi L. V., 1964, ApJ, 140 23

Kulkarni A. K., Romanova M. M., 2008, MNRAS, 386, 673 82, 104, 105, 111

Kulkarni A. K., Romanova M. M., 2009, MNRAS, 398, 701 82, 104, 105, 111

Kurosawa R., Romanova M. M., 2013, MNRAS, 431, 2673 105

Kurosawa R., Harries T. J., Symington N. H., 2005, MNRAS, 358, 671 28

Lada C. J., 1987, IAU Symposium, 115 53

Lada C. J., Lada E. A., 2003, ARA&A 1

Lamm M. H., Bailer-Jones C. A. L., Mundt R., Herbst W., Scholz A., 2004, A&A, 417, 557 115

Lamzin S. A., Bisnovatyi-Kogan G. S., Errico L., Giovannelli F., Katysheva N. A., Rossi C., Vittone A. A., 1996, A&A 82

Langeveld A. B., Madhusudhan N., Cabot S. H., Hodgkin S. T., 2021, MNRAS, 502, 4392 42

Lee C.-F., 2020, A&AR, 28 23, 54

Livio M., 2009, ASSP, 13, 3 23

Lorenzetti D., Larionov V. M., Giannini T., Arkharov A. A., Antoniucci S., Nisini B., Di Paola A., 2009, ApJ, 693, 1056 27, 115

Luhman K. L., 2012, ARA&A, 50, 65 1

Lyman R., Cherubini T., Businger S., 2020, Monthly Notices of the Royal Astronomical Society, 496, 4734 41

Lynden-Bell D., 1969, Nature, 223, 690 4

Lynden-Bell D., Pringle J. E., 1974, MNRAS, 168, 603 10

Mainzer A., et al., 2011, ApJ, 731, 53 69

Mainzer A., et al., 2014, ApJ, 792, 30 69

Manara C. F., Robberto M., Rio N. D., Lodato G., Hillenbrand L. A., Stassun K. G., Soderblom D. R., 2012, ApJ, 755, 154 17

Manara C. F., Testi L., Natta A., Alcalá J. M., 2015, A&A, 579, 66 1

Manara C. F., Fedele D., Herczeg G. J., Teixeira P., 2016, A&A, 585, A136 14, 17

Marti J., Rodriguez L. F., Reipurth B., 1995, ApJ, 449, 184 23

Martín E. L., 1998, AJ, 115, 351 85

Martín E. L., 1997, A&A, 321, 492 50

McGinnis P., Dougados C., Alencar S. H., Bouvier J., Cabrit S., 2018, A&A, 620, 1 86, 97, 100, 101, 116

McGinnis P., Bouvier J., Gallet F., 2020, MNRAS, 497, 2142 90, 102

Mendigutia I., Oudmaijer R. D., Rigliaco E., Fairlamb J. R., Calvet N., Muzerolle J., Cunningham N., Lumsden S. L., 2015, MNRAS, 452, 2837 64

Mestel L., 1965, QJRAS, 6, 161 22, 23

Mihalas D., 1978, Stellar atmospheres. W. H. Freeman 33

Milli J., et al., 2019, Proceedings of the AO4ELT6 conference 41

Moehler S., et al., 2014, A&A, 568, 9 42, 43

Monnier J. D., Millan-Gabet R., 2002, ApJ, 579, 694 13

Moorwood A., et al., 1998, The Messenger, 94, 7 45, 55

Motte F., Bontemps S., Louvet F., 2018, ARA&A, 56, 41 8

Mundt R., 1984, ApJ, 280, 749 23

Muzerolle J., Hartmann L., Calvet N., 1998, AJ, 116, 2965 10, 62, 64

Muzerolle J., Calvet N., Hartmann L., 2001, ApJ, 550, 944 10, 51

Muzerolle J., Hillenbrand L., Calvet N., Briceño C., Hartmann L., 2003, ApJ, 592, 266 51

Natta A., Giovanardi C., 1990, ApJ, 356, 646 24

Natta A., Prusti T., Neri R., Wooden D., Grinin V. P., Mannings V., 2001, A&A, 371, 186 28

Natta A., Testi L., Muzerolle J., Randich S., Comerón F., Persi P., 2004, A&A, 424, 603 17

Natta A., Testi L., Randich S., 2006, A&A, 452, 245 17

Natta A., Testi L., Alcalá J. M., Rigliaco E., Covino E., Stelzer B., D'Elia V., 2014, A&A, 569, 5 24

Nealon R., Pinte C., Alexander R., Mentiplay D., Dipierro G., 2019, MNRAS, 484, 4951 28

Nguyen D. C., Brandeker A., Van Kerkwijk M. H., Jayawardhana R., 2012, ApJ, 745, 119 85

Nisini B., 2008, Lecture Notes in Physics, 742, 79 28, 48, 50, 66

Nisini B., Caratti o Garatti A., Giannini T., Lorenzetti D., 2002, A&A, 393, 1035 49, 50, 66

Nisini B., Bacciotti F., Giannini T., Massi F., Eislöffel J., Podio L., Ray T. P., 2005, A&A, 441, 159 49

Nisini B., Giannini T., Antoniucci S., Alcalá J. M., Bacciotti F., Podio L., 2016, A&A, 595, 76 24

Nussbaumer H., Storey P. J., 1988, A&A, 193, 327 32, 49, 50

Ostriker E. C., Shu F. H., 1995, ApJ, 447, 813 4, 10

Palla F., Randich S., Pavlenko Y. V., Flaccomio E., Pallavicini R., 2007, ApJ, 659, L41 106

Perraut K., et al., 2021, A&A, 655, A73 12

Persson M. V., 2014a, Current view of protostellar evolution (ENG) 3

Persson M. V., 2014b, SEDs of the different protostellar evolutionary stages 5, 116

Pinilla P., et al., 2018, ApJ, 868, 14 28

Planck M., 1901, Annalen der Physik, 309, 553 30

Pontoppidan K. M., Dullemond C. P., Blake G. A., Boogert A. C. A., van Dishoeck E. F., Evans N. J., Kessler-Silacci J., Lahuis F., 2007, ApJ, 656, 980 28

Pradhan A. K., Nahar S. N., 2011, Atomic Astrophysics and Spectroscopy. Cambridge University Press 30, 31, 32, 33

Pudritz R. E., Norman C. A., 1983, ApJ, 274, 677 22

Pudritz R. E., Ray T. P., 2019, Frontiers in Astronomy and Space Sciences, 6, 54 23

Quinet P., Le Dourneuf M., Zeippen C., 1996, A&A 50

Raga A. C., Cantó J., Binette L., Calvet N., 1990, ApJ, 364, 601 23

Raga A. C., Rodríguez-Ramírez J. C., Cantó J., Velázquez P. F., 2015, MNRAS, 454, 412 23

Raga A. C., et al., 2017, Revista Mexicana de Astronomía y Astrofísica, 53, 485 23

Ray T., Dougados C., Bacciotti F., Eislöffel J., Chrysostomou A., 2007, Protostars and Planets V, p. 231 6, 23, 81, 100

Rebull L. M., et al., 2014, AJ, 148, 92 81

Rei A. C., Petrov P. P., Gameiro J. F., 2018, A&A, 610, 40 111

Reiners A., 2012, Living Reviews in Solar Physics, 9, 73 35

Reiners A., Shulyak D., Anglada-Escudé G., Jeffers S. V., Morin J., Zechmeister M., Kochukhov O., Piskunov N., 2013, A&A, 552, 103 35, 36

Reipurth B., 1989, Nature, Volume 340, Issue 6228, pp. 42-45 (1989)., 340, 42 118

Reipurth B., Bally J., 2001, ARA&A, 39, 403 23

Rieke G. H., Lebofsky M. J., 1985, ApJ, 288, 618 49, 73

Rigliaco E., Natta A., Randich S., Testi L., Biazzo K., 2011, A&A, 525, 47 17

Rigliaco E., Natta A., Testi L., Randich S., Alcalá J., Covino E., Stelzer B., 2012, A&A, 548 1, 14

Rigliaco E., Pascucci I., Gorti U., Edwards S., Hollenbach D., 2013, ApJ, 772, 60 24, 86, 100

Robberto M., Song J., Carrillo G. M., Beckwith S. V. W., Makidon R. B., Panagia N., 2004, ApJ, 606, 952 17

Romanova M. M., Kulkarni A. K., Lovelace R. V. E., 2008, ApJl, 673, L171 81, 104, 105, 111

Romanova M. M., Ustyugova G. V., Koldoba A. V., Lovelace R. V. E., 2009, Ap&SS Proceedings, pp 153–163 26

Rosotti G. P., Dale J. E., de Juan Ovelar M., Hubber D. A., Kruijssen J. M. D., Ercolano B., Walch S., 2014, MNRAS, 441, 2094 106

Rousselot P., Lidman C., Cuby J.-G., Moreels G., Monnet G., 2000, A&A, 354, 1134 56

Rudolf N., Günther H. M., Schneider P. C., Schmitt J. H., 2016, A&A, 585, A113 42

Saar S. H., Linsky J. L., 1985, ApJ, 473, 47 37

Schneider P. C., Günther H. M., Robrade J., Schmitt J. H. M. M., Güdel M., 2018, A&A, 618, A55 16

Scholz A., Jayawardhana R., 2006, ApJ, 638 81, 83

Schulz N. S., 2005, From Dust to Stars : studies of the formation and early evolution of stars. Springer 2, 3, 8, 37, 48

Sestito P., Palla F., Randich S., 2008, A&A, 487, 965 106

Shakura N. I., Sunyaev R. A., 1973, A&A, 24, 337 4

Sharples R., et al., 2013, The Messenger, 151, 21 115

Shu F. H., Adams F. C., Lizano S., 1987, ARA&A, 25, 23 1, 3, 4, 22

Sicilia-Aguilar A., Hartmann L. W., Hernández J., no C. B., Calvet N., 2005, AJ, 130, 188 17

Sicilia-Aguilar A., Hartmann L. W., Fürész G., Henning T., Dullemond C., Brandner W., 2006, AJ, 132 106

Sicilia-Aguilar A., Henning T., Hartmann L. W., 2010, ApJ, 710, 597 17, 106

Sicilia-Aguilar A., Fang M., Roccatagliata V., Cameron A. C., Kóspál Á., Henning T., Ábrahám P., Sipos N., 2015, A&A, 580, 82 29, 102

Simon M. N., Pascucci I., Edwards S., Feng W., Gorti U., Hollenbach D., Rigliaco E., Keane J. T., 2016, ApJ, 831, 169 24, 86, 100, 101

Siwak M., et al., 2016, MNRAS, 456, 3972 82, 103

Smette A., et al., 2015, A&A, 576, 77 42

Sousa A., et al., 2016, A&A, 586, A47 116

Stahler S. W., Palla F. F., 2004, The Formation of Stars. Wiley-VCH 3, 8, 33, 34, 35, 50, 51

Stapelfeldt K., Burrows C. J., Krist J. E., 1997, Herbig-Haro Flows and the Birth of Low Mass Stars, pp 355–364 23

Stapelfeldt K. R., et al., 1999, ApJ, 516, L95 23, 24

Stefan J., 1879, Akademie der Wissenschaften, 79, S 29

Stelzer B., Schmitt J. H. M. M., 2004, A&A, 418, 687 16

Stempels H. C., Gahm G. F., Petrov P. P., 2007, A&A, 461, 253 82, 102, 103, 104

Sullivan T., Wilking B. A., Greene T. P., Lisalda L., Gibb E. L., Ejeta C., 2019, AJ, 158, 41 54

Sung H., Bessell M. S., Lee S.-W., 1997, AJ, 114, 2644 116

Takami M., Bailey J., Gledhill T. M., Chrysostomou A., Hough J. H., 2001, MNRAS, 323, 177 85

Teixeira P. S., et al., 2006, ApJ, 636, L45 116

Tokovinin A., Kornilov V., 2007, MNRAS, 381, 1179 41

Valenti J. A., Basri G., Johns C. M., 1993, AJ, 106, 2024 17, 97

Venuti L., et al., 2014, A&A, 570, A82 103, 116

Venuti L., et al., 2018, A&A, 609, 10 116

Walter F. M., Brown A., Mathieu R. D., Myers P. C., Vrba F. J., 1988, AJ, 96, 297 106

Whelan E., Garcia P., 2008, Jets from Young Stars II, Lecture Notes in Physics, Volume 742. ISBN 978-3-540-68031-4. Springer-Verlag Berlin Heidelberg, 2008, p. 105, 742, 105 42

Whelan E. T., Pascucci I., Gorti U., Edwards S., Alexander R. D., Sterzik M. F., Melo C., 2021, ApJ, 913, 43 99, 100, 101

White R. J., Basri G., 2003, ApJ, 582, 1109 6, 87

White R. J., Greene T. P., Doppmann G. W., Covey K. R., Hillenbrand L. A., 2007, Protostars and Planets V, pp 117–132 6, 25

Wouterloot J. G. A., Brand J., Henkel C., 2005, A&A, 430, 549 56

Wright E. L., et al., 2010, AJ, 140, 1868 69

Zinnecker H., McCaughrean M. J., Rayner J. T., 1998, Nature, 394, 862 23

Zsidi G., et al., 2022, A&A, 660, A108 103

Zuckerman B., Palmer P., 1974, ARA&A, 12, 279 4

de Zeeuw P. T., Hoogerwerf R., de Bruijne J. H. J., Brown A. G. A., Blaauw A., 1999, AJ, 117, 354 1

van Kempen T. A., van Dishoeck E. F., Salter D. M., Hogerheijde M. R., Jørgensen J. K., Boogert A. C. A., 2009, A&A, 498, 167 54